Novel Materials, Grid Design Rule, and Characterization Methods for Multi-Junction Solar Cells

by

Jingjing Li

A Dissertation Presented in Partial Fulfillment
of the Requirements for the Degree
Doctor of Philosophy

Approved May 2012 by the
Graduate Supervisory Committee:

Yong-Hang Zhang, Chair
Meng Tao
Dieter Schroder
Dragica Vasileska

ARIZONA STATE UNIVERSITY

August 2012

ABSTRACT

This dissertation addresses challenges pertaining to multi-junction (MJ) solar cells from material development to device design and characterization.

Firstly, among the various methods to improve the energy conversion efficiency of MJ solar cells using, a novel approach proposed recently is to use II-VI (MgZnCd)(SeTe) and III-V (AlGaIn)(AsSb) semiconductors lattice-matched on GaSb or InAs substrates for current-matched subcells with minimal defect densities. CdSe/CdTe superlattices are proposed as a potential candidate for a subcell in the MJ solar cell designs using this material system, and therefore the material properties of the superlattices are studied. The high structural qualities of the superlattices are obtained from high resolution X-ray diffraction measurements and cross-sectional transmission electron microscopy images. The effective bandgap energies of the superlattices obtained from the photoluminescence (PL) measurements vary with the layer thicknesses, and are smaller than the bandgap energies of either the constituent material. Furthermore, The PL peak position measured at the steady state exhibits a blue shift that increases with the excess carrier concentration. These results confirm a strong type-II band edge alignment between CdSe and CdTe. The valence band offset between unstrained CdSe and CdTe is determined as 0.63 eV ±0.06 eV by fitting the measured PL peak positions using the Kronig-Penney model. The blue shift in PL peak position is found to be primarily caused by the band bending effect based on self-consistent solutions of the Schrödinger and Poisson equations.

Secondly, the design of the contact grid layout is studied to maximize the power output and energy conversion efficiency for concentrator solar cells. Because the conventional minimum power loss method used for the contact design is not accurate in determining the series resistance loss, a method of using a distributed series resistance model to maximize the power output is proposed for the contact design. It is found that the junction recombination loss in addition to the series resistance loss and shadowing loss can significantly affect the contact layout. The optimal finger spacing and maximum efficiency calculated by the two methods are close, and the differences are dependent on the series resistance and saturation currents of solar cells.

Lastly, the accurate measurements of external quantum efficiency (EQE) are important for the design and development of MJ solar cells. However, the electrical and optical couplings between the subcells have caused EQE measurement artifacts. In order to interpret the measurement artifacts, DC and small signal models are built for the bias condition and the scan of chopped monochromatic light in the EQE measurements. Characterization methods are developed for the device parameters used in the models. The EQE measurement artifacts are found to be caused by the shunt and luminescence coupling effects, and can be minimized using proper voltage and light biases.

Novel measurement methods using a pulse voltage bias or a pulse light bias are invented to eliminate the EQE measurement artifacts. These measurement methods are nondestructive and easy to implement. The pulse voltage bias or

pulse light bias is superimposed on the conventional DC voltage and light biases, in order to control the operating points of the subcells and counterbalance the effects of shunt and luminescence coupling. The methods are demonstrated for the first time to effectively eliminate the measurement artifacts.

ACKNOWLEDGMENTS

I would like to express my sincere gratitude to all who have contributed to this work and who has helped me finishing this doctoral dissertation.

First of all, I would like to thank my adviser, Prof. Yong-Hang Zhang, for being a great supervisor and mentor. Without his absolute support and experienced advice, I would never have accomplished as much as what I have done. I also want to thank Prof. Zhang for mentoring me to grow into an independent and capable researcher. I will benefit from the comprehensive Ph.D. training for the rest of my life. I want to thank Prof. Meng Tao, Prof. Dieter Schroder and Prof. Dragica Vasileska for serving on my committee of Ph.D. defense and Prof. Ronald Roedel and Prof. Dr. Cun-Zhang Ning for serving on my committee of Ph.D. qualifying and comprehensive exams. I also want to thank Dr. Shane R. Johnson for the extensive discussions on research topics and scientific writing techniques. It is my great honor to learn from all these world-class researchers.

Secondly, I would like to thank the wonderful colleagues including Dr. Swee Hoe Lim, Dr. Ding Ding, all the members of the MBE Optoelectronics Group, the collaborators and research staffs. Great appreciation goes to Dr. Swee Hoe Lim, whose excellent work has led to a variety of research opportunities for me. I want to thank Dr. Ding Ding who has helped me getting started when I first joined the group, and the rest of the MBE Optoelectronics Group for the great teamwork. I want to thank Dr. Xinyu Liu and Dr. Jacek Furdyna in Notre Dame

University for growing samples and the helpful discussions and thank Leijun Yin, Prof. Cun-Zheng Ning, and Prof. David Smith for helping with measurements. In addition, I want to thank Newport Corporation, Emcore Corporation and Spectrolab for providing equipments and samples for us. I also want to thank the research staffs at Arizona State University whose efforts in maintaining the laboratory equipments have been crucial for my research work.

Finally, I would like to devote my deepest appreciation to my parents, Xing Li and Lin Du, who have always stood by my side no matter what happened. I would not have gone anywhere without their unlimited love and support.

TABLE OF CONTENTS

Page

CHAPTER Page

CHAPTER Page

LIST OF TABLES

LIST OF FIGURES

Figure Page

Figure Page

Figure Page

Figure Page

I INTRODUCTION

Multi-junction (MJ) solar cells have reached remarkably high energy conversion efficiencies over the past two decades, accompanied with the increased research interests and commercial applications of these devices [1]–[13]. By employing several subcells to partition the solar spectrum, MJ solar cells have much higher efficiencies than their single junction counterparts, as both predicted in theory and achieved in practice. The subcells more efficiently utilize the photon energies in their respective wavelength ranges of the solar spectrum, producing a higher voltage and lower current as the subcell number increases. MJ solar cells have been extensively used in space because of their high efficiencies, small sizes, low weights, and superior radiation resistance. They also started to be applied in terrestrial concentrator systems for large scale utility projects, as their high efficiencies may potentially make the cost of electricity generation lower than conventional energy sources.

1.1 Theoretical Efficiency Limits

The theoretical efficiency limits for solar cells are usually estimated based on the second law of thermodynamics [14]–[19] or more realistic models considering the properties of specific devices [20]–[21]. The Shockley-Queisser limit or detailed-balance limit [14] gives the maximum theoretical efficiency of power conversion as 30% for p-n junction solar cells, considering the fundamental recombination mechanism, i.e. the radiative recombination, and assuming complete absorption of the black-body spectrum above the semiconductor

bandgap. Later, Henry has extended the Shockley-Queisser model using an air mass 1.5 terrestrial solar spectrum, and the maximum efficiency is calculated as 31% under 1 sun [15] for single junction solar cells. The detailed-balance model was also used for MJ solar cells with various numbers of junctions and concentration levels [16]–[18]. In particular, the maximum efficiency for three junction and four junction solar cells were found to be 51.58% and 55.31% under 1 sun AM 1.5 G solar spectrum, respectively [18]. While the detailed-balance limit gives the theoretical efficiency limit of solar cells, realistic models considering the band structure, the actual absorbance, the nonradiative recombination, and the collection efficiency, etc., are more relevant to practical applications [19]–[21]. The achievable maximum efficiency is lower than the theoretical limit when these extrinsic mechanisms are considered, and the configuration of the bandgap energies of the solar cells shift as well. Realistic solar cells may reach up to 75% of the detailed-balance efficiency according to some empirical evidences [24].

1.2 Realistic Efficiency

III-V multijunction solar cells have realized very high efficiencies owing to the large flexibility in the selection of bandgap energies with high quality materials. The state-of-the-art III-V triple junction solar cells have reached efficiencies over 40% via several different device architectures. Among these, the most mature one is the InGaP/Ga(In)As/Ge lattice-matched triple junction solar cells. The lattice-matched nature of the triple junction solar cells provides the

advantages of high material quality and fast growth rate that enables large scale production. The reported record efficiency of lattice-matched triple junction solar cells is 41.6% under 364 suns concentration [8]. However, because the subcell bandgaps are not optimized, the Ge subcell produces almost twice the photocurrents of the top two subcells. This has been a critical limiting factor of the efficiencies of lattice-matched designs. To address this problem, the bandgap energies of the top two subcells need to be decreased or the bandgap energy of the bottom subcell needs to be increased.

The use of metamorphic III-V semiconductor materials offers more flexibility to tune the subcell bandgap energies. By adding a little more Indium into the InGaP and InGaAs subcells, their bandgap energies are decreased while the lattice mismatches to the Ge bottom cell is increased [22]–[24]. A step-graded InGaAs buffer layer was added between the top two subcells and the Ge subcell as a transition between the different lattice constants. Because most misfit dislocations are confined in the grading layer, the material qualities of the top two subcells are not substantially affected. The reported record efficiency of this device architecture is 41.1% under 454 suns concentration [24]. The efficiency can be further improved by increasing the bandgap energy of the bottom subcell to further optimize the bandgap configurations. The InGaP/InGaAs/InGaAs inverted metamorphic (IMM) structure has been developed for this purpose [25]–[26]. The IMM structure consists of an InGaP top cell lattice-matched to the GaAs substrate, a lattice-matched or metamorphic InGaAs middle cell and a

metamorphic InGaAs bottom cell. A grading buffer layer is inserted between the middle cell and the bottom cell to accommodate the misfit dislocations. The disadvantage of this device design is the complex processing steps including wafer bonding and substrate removal. A record efficiency of 40.8% has been reported for this device architecture under 326 suns concentration [26]. Another approach to increase the bandgap energy of the bottom subcell is the bifacial epigrowth process [27], [28], where the InGaP top cell and GaAs middle cell are grown lattice-matched on one side of the GaAs substrates and the metamorphic InGaAs bottom cell is grown on the other side of the substrates. For this device design, the substrate doping concentration has to be optimized considering the tradeoff between series resistance and free carrier absorption. Moreover, the interruption of the growth may add onto the cost of the process. The reported record efficiency of this device architecture is 42.3% under 406 suns concentration [28].

Other more drastic departures from conventional triple junction solar cells are to employ dilute nitrides [29]–[31] and quantum dots [32]–[33] in the solar cells. The incorporation of nitride materials enables better current matching and higher output voltage than using the Ge subcells. In spite of the low minority carrier lifetime and mobility of the nitride materials, an efficiency of 43.5%, which is the current world record of triple junction solar cells, has been achieved under 400 suns by optimizing the device structures and material qualities [34]. MJ solar cells using quantum dots may have increased light absorption below the

bandgap, and have the potential to reach the efficiency of over 40% [35]. However, the strain effects introduced by the self assembly of quantum dots cause defects that may reduce the minority carrier lifetime and open circuit voltage. Strain compensation techniques have to be applied in order to obtain high photocurrent as well as open circuit voltage.

1.3 Challenges

In spite of the high efficiencies achieved with the current technologies, there is still a large gap between the practically achieved efficiencies and the theoretical efficiency limits of MJ solar cells. Many challenges remain to be addressed, presenting the opportunities for a variety of research topics.

Firstly, the employment of more junctions and new material systems has been under active investigation to make current-matched subcells with high material qualities. Recently, the monolithic integration of II-VI (MgZnCd)(SeTe) and III-V (AlGaIn)(AsSb) semiconductors on commercially available GaSb or InAs substrates has been proposed as a platform for ultra-high efficiency MJ solar cells [36], [37]. These two families of semiconductor materials have identical crystalline structures and very similar thermal expansion coefficients, and they can be grown lattice-matched on GaSb or InAs substrates with low defect densities. Furthermore, the direct bandgaps of these materials allow the use of thin absorbing layers that can be current-matched to efficiently capture the entire solar spectrum.

Several multi-junction solar cell structures have been designed with the potential to reach ultra-high conversion efficiencies [37]. In the proposed solar cell designs, a zinc blende CdSeTe alloy lattice matched to the GaSb substrates is used as one of the subcells. The growth and characterization of the type-II CdSe/CdTe superlattices are studied in Chapter II of this dissertation. A series of CdTe/CdSe superlattice structures were grown using molecular beam epitaxy. The structural properties were characterized using high-resolution X-ray diffraction and cross-sectional transmission electron microscopy. The optical properties were characterized using steady-state and time-resolved photoluminescence. The Kronig-Penney model was used to fit the valence band offset with the measured photoluminescence peak positions. Self-consistent solutions of Schrödinger and Poisson equations were performed to model the bend bending effect that caused the blue shift in the photoluminescence peak position in the steady state measurements. Another issue for high efficiency solar cells used in terrestrial concentrating photovoltaic systems is the design of the front contact layout. The front contact layout has to be optimized to minimize the power losses and maximize the output power. Traditionally, the series resistance has been considered as a lumped parameter in the design of front contact layout [38], and the grid finger spacing has been optimized considering the tradeoff between the series resistance loss and the shadowing loss. However, the power losses associated with the series resistance are distributed in nature [39], and the variation of local voltage and current densities in the current flow path may make

it necessary to consider the carrier recombination loss at the junction. Therefore, the design of the front contact layout needs to be reevaluated considering the distributed series resistances.

The front contact layout of solar cells is designed using the distributed series resistance model in Chapter III. Using this model, the variations of local junction voltage and current caused by the lateral current flow in the emitter layer were simulated. The power loss due to the junction recombination current was introduced into the loss mechanisms associated with the front contact, in addition to the series resistance loss and shadowing loss considered in the conventional method. The optimal contact grid spacing was calculated and compared with the conventional method.

The monolithic integration of MJ solar cells has posed unique problems in the characterization of the devices. Because the subcells are in series connection and close proximity, they are coupled both electrically and optically. It is therefore difficult to access the information of the individual subcells. In particular, the external quantum efficiency (EQE) of the individual subcells is determined not only by their own properties, but also by the interactions between them. In order to probe a subcell in a multi-junction stack, DC light biases have to be applied on the subcells not under test to make the subcell under test the current-limiting one. A DC voltage bias is also used to control the subcell operating points in the measurements. However, measurement artifacts are often observed, characterized by the erroneous responses outside the wavelength range

of the subcell under test and the correspondingly lower responses in the wavelength range of the subcell under test [40].

The origins of the EQE measurement artifacts of MJ solar cells are systematically studied in Chapter IV. Models were built for the DC bias conditions in the EQE measurements as well as the AC measurement scans. Characterization methods were developed to obtain the subcell parameters used in the models. The EQE measurement artifacts were characterized for triple junction solar cells with only the shunt effect, only the luminescence coupling effect and the combined effects of shunt and luminescence coupling. It is shown that the EQE measurement artifacts can be minimized by controlling the DC bias conditions.

In order to eliminate the EQE measurement artifacts, novel measurement methods are developed in Chapter V. A pulse voltage bias or a pulse light bias is superimposed on the DC bias conditions to control the subcell operating points and counterbalance the shunt and luminescence coupling effects. The necessary pulse voltage bias and pulse light bias were derived, and the measurement procedures were developed. It is demonstrated that the pulse voltage bias method and pulse light bias method are effective in eliminating the measurement artifacts of triple junction solar cells with only the shunt effect, only the luminescence coupling effect and the combined effects of shunt and luminescence coupling.

References

[1] R. R. King, C. M. Fetzer, P. C. Colter, K. M. Edmondson, J. H. Ermer, H. L. Cotal, H. Yoon, A. P. Stavrides, G. Kinsey, D. D. Krut, and N. H. Karam, "High-efficiency space and terrestrial multijunction solar cells through bandgap control in cell structures," in *Proc. 29th IEEE PVSC*, New Orleans, pp. 776–781, May 2002.

[2] R. R. King, D. C. Law, C. M. Fetzer, R. A. Sherif, K. M. Edmondson, S. Kurtz, G. S. Kinsey, H. L. Cotal, D. D. Krut, J. H. Ermer, and N. H. Karam, "Pathways to 40%-efficient concentrator photovoltaics," in *20th EU PVSEC*, Barcelona, pp. 118–123, Jun. 2005.

[3] R. R. King, C. M. Fetzer, D. C. Law, K. M. Edmondson, H. Yoon, G. S. Kinsey, D. D. Krut, J. H. Ermer, P. Hebert, B. T. Cavicchi, and N. H. Karam, "Advanced III-V multijunction cells for space," in *Proc. 4th WCPEC*, Waikoloa, pp. 1757–1762, May 2006.

[4] R. R. King, D. C. Law, K. M. Edmondson, C. M. Fetzer, G. S. Kinsey, H. Yoon, D. D. Krut, J. H. Ermer, R. A. Sherif, and N. H. Karam, "Advances in high-efficiency III-V multijunction solar cells," *Adv. Optoelectron.*, vol. 2007, pp. 1–9, 2007.

[5] F. Dimroth and S. Kurtz, "High efficiency multijunction solar cells," *MRS Bulletin*, vol. 32, pp. 230–235, 2007.

[6] U. Rau, "Reciprocity relation between photovoltaic quantum efficiency and electroluminescent emission of solar cells," *Phys. Rev. B*, vol. 76, no. 8, p. 085303, 2007.

[7] G. S. Kinsey and K. M. Edmondson, "Spectral response and energy output of concentrator multijunction solar cells," *Prog. Photovolt: Res. Appl.*, vol. 17, no. 5, pp. 279–288, 2009.

[8] R. R. King, A. Boca, W. Hong, X.-Q. Liu, D. Bhusari, D. Larrabee, K.M. Edmondson, D.C. Law, C.M. Fetzer, S. Mesropian and N.H. Karam, "Band gap engineered architectures for high-efficiency multijunction concentrator solar cells," in *Proc. 24th EU PVSC*, Hamburg, pp. 55–61, Sep. 2009.

[9] H. Cotal, C. Fetzer, J. Boisvert, G. Kinsey, R. King, P. Hebert, H. Yoon and N. Karam, "III–V multijunction solar cells for concentrating photovoltaics", *Energy Environ. Sci.*, vol. 2, pp. 174–192, 2009.

[10] D. J. Friedman, "Progress and challenges for next-generation high-efficiency multijunction solar cells," *Curr. Opin. Solid St. M.*, vol. 14, no. 6, pp. 131–138, 2010.

[11] D. C. Law, R. R. King, H. Yoon, M. J. Archer, A. Boca, C. M. Fetzer, S. Mesropian, T. Isshiki, M. Haddad, K. M. Edmondson, D. Bhusari, J. Yen, R. A. Sherif, H. A. Atwater, N.H. Karam, "Future technology pathways of terrestrial III-V multijunction solar cells for concentrator photovoltaic systems," *Sol. Energ. Mat. Sol. C.*, vol. 94, no. 1, pp. 1314–1318, 2010.

[12] N. H. Karam, R. R. King, M. Haddad, J. H. Ermer, H. Yoon, H. L. Cotal, R. Sudharsanan, J. W. Eldredge, K. Edmondson, D. E. Joslin, D. D. Krut, M. Takahashi, W. Nishikawa, M. Gillanders, J. Granata, P. Hebert, B. T. Cavicchi, and D. R. Lillington, "Recent developments in high-efficiency $Ga_{0.5}In_{0.5}P$/GaAs/Ge dual- and triple-junction solar cells: steps to next-generation PV cells," *Sol. Energ. Mat. Sol. C.*, vol. 66, no. 1–4, pp. 453–466, 2001.

[13] T. Takamoto, T. Agui, K. Kamimura, M. Kaneiwa, M. Imaizumi, S. Matsuda, and M. Yamaguchi, "Multijunction solar cell technologies-high efficiency, radiation resistance, and concentrator applications, " in *Proc. WCPEC-3*, Osaka, pp. 581 – 586, May 2003.

[14] W. Shockley and H. J. Queisser, "Detailed Balance Limit of Efficiency of p-n Junction Solar Cells," *J. Appl. Phys.*, vol. 32, no. 3, pp. 510–519, 1961.

[15] C. H. Henry, "Limiting efficiencies of ideal single and multiple energy gap terrestrial solar cells," *J. Appl. Phys.*, vol. 51, no. 8, pp. 4494–4500, 1980.

[16] A. Martí and G. L. Araújo, "Limiting efficiencies for photovoltaic energy conversion in multigap systems," *Sol. Energ. Mat. Sol. C.*, vol. 43, no. 2, pp. 203–222, Sep. 1996.

[17] A. S. Brown and M. A. Green, "Detailed balance limit for the series constrained two terminal tandem solar cell," *Physica E*, vol. 14, no. 1–2, pp. 96–100, 2002.

[18] S. P. Bremner, M. Y. Levy, and C. B. Honsberg, "Analysis of tandem solar cell efficiencies under AM1.5G spectrum using a rapid flux calculation method," *Prog. Photovolt: Res. Appl.*, vol. 16, no. 3, pp. 225–233, 2008.

[19] U. Rau and J. H. Werner, "Radiative efficiency limits of solar cells with lateral band-gap fluctuations," *Appl. Phys. Lett.*, vol. 84, no. 19, pp. 3725–3728, 2004.

[20] S. Kurtz, D. Myers, W. E. McMahon, J. Geisz, and M. Steiner, "A comparison of theoretical efficiencies of multi-junction concentrator solar cells," *Prog. Photovolt: Res. Appl.*, vol. 16, no. 6, pp. 537–546, 2008.

[21] D. Ding, S. R. Johnson, S. Q. Yu, S. N. Wu, and Y.-H. Zhang, "A semi-analytical model for semiconductor solar cells," *J. Appl. Phys.*, vol. 110, no. 12, p. 123104, 2011.

[22] R. R. King, C. M. Fetzer, K. M. Edmondson, D. C. Law, P. C. Colter, H. L. Cotal, R. A. Sherif, H. Yoon, T. Isshiki, D. D. Krut, G. S. Kinsey, J. H. Ermer, Sarah Kurtz, T. Moriarty, J. Kiehl, K. Emery, W. K. Metzger, R. K. Ahrenkiel, and N. H. Karam, "Metamorphic III-V materials, sublattice disorder, and multijunction solar cell approaches with over 37% efficiency," in *Proc. 19th EU PVSEC*, Paris, pp. 3587–3593, Jun. 2004.

[23] R. R. King, D. C. Law, K. M. Edmondson, C. M. Fetzer, G. S. Kinsey, H. Yoon, R. A. Sherif, and N. H. Karam, "40% efficient metamorphic GaInP/GaInAs/Ge multijunction solar cells," *Appl. Phys. Lett.*, vol. 90, p. 183516, 2007.

[24] W. Guter, J. Schöne, S. P. Philipps, M. Steiner, G. Siefer, A. Wekkeli, E. Welser, E. Oliva, A. W. Bett and F. Dimroth, "Current-matched triple-junction solar cell reaching 41.1% conversion efficiency under concentrated sunlight," *Appl. Phys. Lett.*, vol. **94**, p. 223504, 2009.

[25] J. F. Geisz, S. Kurtz, M. W. Wanlass, J. S. Ward, A. Duda, D. J. Friedman, J. M. Olson, W. E. McMahon, T. E. Moriarty, and J. T. Kiehl, "High-efficiency GaInP/GaAs/InGaAs triple-junction solar cells grown inverted with a metamorphic bottom junction," *Appl. Phys. Lett.*, vol. **91**, p. 023502, 2007.

[26] J. F. Geisz, D. J. Friedman, J. S. Ward, A. Duda, W. J. Olavarria, T. E. Moriarty, J. T. Kiehl, M. J. Romero, A. G. Norman and K. M. Jones, 40.8% efficient inverted triple-junction solar cell with two independently metamorphic junctions, *Appl. Phys. Lett.*, vol. 93, p. 123505, 2008.

[27] S. Wojtczuk, P. Chiu, X. Zhang, D. Derkacs, C. Harris, D. Pulver1 and M. Timmons, "InGaP/GaAs/InGaAs 41% concentrator cells using bi-facial epigrowth," in *Proc. 35th IEEE PVSC*, Hawaii, pp. 1259–1264, Jun. 2010.

[28] P. Chiu, S. Wojtczuk, X. Zhang, C. Harris, D. Pulver, and M. Timmons, "42.3% efficient InGaP/GaAs/InGaAs concentrators using bifacial epigrowth," in *Proc. 37th IEEE PVSC*, Seattle, Jun. 2011, in press

[29] D. J. Friedman, J. F. Geisz, S. R. Kurtz and J. M. Olson, "1-eV GaInNAs solar cells for ultrahigh-efficiency multijunction devices," in *Proc. WCPEC-2*, Vienna, pp. 3–7, Jul. 1998.

[30] R. R. King, P. C. Colter, D. E. Joslin, K. M. Edmondson, D. D. Krut, N. H. Karam, and S. Kurtz, "Hig-voltage, low-current GaInP/GaInP/GaAs/GaInNAs/Ge solar cells," in *Proc. 29th IEEE PVSC*, New Orleans, pp. 852–855, May 2002.

[31] D. J. Friedman, A. J. Ptak, S. R. Kurtz, J. F. Geisz, and J. Kiehl, "GaInNAs junctions for next-generation concentrators: progress and prospects," in *Proc. ICSC-3*, Scottsdale, pp. NREL/CD-520-38172, May 2005.

[32] R. P. Raffaelle, S. Sinharoy, and J. Andersen, "Multi-junction solar cell spectral tuning with quantum dots," in *Proc. WCPEC-4*, pp. 162–166, Waikoloa, May 2006.

[33] C. G. Bailey, D. V. Forbes, R. P. Raffaelle, and S. M. Hubbard, "Near 1 V open circuit voltage InAs/GaAs quantum dot solar cells," *Appl. Phys. Lett.*, vol. 98, no. 16, p. 163105, 2011.

[34] http://www.sj-solar.com/downloads/Solar_Junction_World_Record_%20Efficiency_14April11.pdf

[35] http://www.cyriumtechnologies.com/products

[36] Y.-H. Zhang, S.-N. Wu, D. Ding, S.-Q. Yu, S. R. Johnson, "A proposal of monolithicly integrated multijunction solar cells using lattice-matched II/VI and III/V semiconductors," in *Proc. 33th IEEE PVSC*, New Jersey, pp. 1–5, May 2008.

[37] S.-N. Wu, D. Ding, S. R. Johnson, S.-Q. Yu and Y.-H. Zhang, "Four-junction solar cells using lattice-matched II-VI and III-V semiconductors", *Prog. Photovoltaic. Res. Appl.*, vol. 18, pp. 328–333, 2010.

[38] H. B. Serreze, "Optimizing Solar Cell Performance by Simultaneous Consideration of Grid Pattern Design and Interconnect Configuration," in *Proc. 13th IEEE PVSC*, Washington, pp. 609–614, Jun. 1978.

[39] B. Galiana, C. Algora, I. Rey-Stolle, and I. G. Vara, "A 3D model for concentrator solar cells based on distributed circuit units," *IEEE T. Electron. Dev.*, vol. 52, no. 12, pp. 2552–2558, 2005.

[40] M. Meusel, C. Baur, G. Letay, A. W. Bett, W. Warta and E. Fernandez, "Spectral response measurements of monolithic GaInP/Ga(In)As/Ge triple-junction solar cell: measurement artifacts and their explanation," *Prog. Photovolt: Res. Appl.*, vol. 11, no. 8, pp. 499–514, 2003.

II CDSE/CDTE TYPE-II SUPERLATTICES

2.1 Introduction

Monolithically integrated II-VI (MgZnCd)(SeTe) and III-V (AlGaIn)(AsSb) semiconductors on commercially available GaSb or InAs substrates are good candidates for high efficiency multi-junction (MJ) solar cells [1]–[3]. Several multi-junction solar cell structures have been designed with the potential to reach ultra-high conversion efficiency [4]. In the proposed solar cell designs, a zinc blende CdSeTe alloy lattice matched to the GaSb substrates is used as one of the subcells. However, there have been only a few successful attempts reported at growing zinc-blende CdSeTe random alloys on Si substrates, and it is difficult to achieve large Se compositions because of the high vapor pressure of group VI elements and the low sticking probability of Se atoms [5]–[8]. In the current work, CdSe/CdTe superlattices are proposed as an alternative to the random CdSeTe alloys, and a series of the superlattice structures are grown on GaSb (001) substrates using molecular beam epitaxy (MBE). While the ZnSe/ZnTe system has been intensively investigated [9], [10], little work has so far been done for the CdSe/CdTe system [11]–[13]. This chapter reports the growth and the structural and optical characterization of the CdSe/CdTe superlattices [14], [15].

2.2 Material Growth

The epitaxial growth of the superlattice samples was carried out using a dual-chamber Riber 32P MBE system consisting of III-V and II-VI chambers

connected by an ultra high-vacuum transfer module. The structures were grown on undoped epi-ready GaSb (001) substrates. First, the substrate oxide was thermally removed by heating up to 510 ℃ under an antimony flux in the III-V chamber, while the process was monitored using reflection high-energy electron diffraction (RHEED). Next, a 100 nm GaSb buffer layer was grown at 470 ℃. The substrate was then transferred to the II-VI chamber, where a ZnTe buffer layer was grown at 320 ℃ under a Zn flux initiated prior to the growth.[2] The CdSe/CdTe superlattice was then grown at 320 ℃ using the modulation of Te and Se shutters while keeping the Cd shutter open. During the growth, the beam equivalent pressure (BEP) ratio of Te/Cd and Se/Cd were kept at 2:1 and 4:1, respectively.

Three CdSe/CdTe superlattice structures (labeled A, B and C) were grown with the various layer thicknesses shown in Table 2.1 and are expected to have different effective bandgap energies. During the growth of sample B, the Cd shutter remained open for 5 sec while all the other shutters were closed after the growth of the CdSe layer, in order to reduce the intermixing of Se and Te at the CdSe/CdTe interface. The RHEED patterns of Samples A and C changed from streaky to spotty during the growth, suggesting a 3D growth mode at the end of the growth. In contrast, the RHEED pattern of Sample B remained streaky through to the end, which suggests that this sample has better crystalline quality and layer uniformity than the other two samples. Note that all the CdSe/CdTe superlattices have the same zinc blende structure as the substrate, as shown by the

RHEED patterns and confirmed by the X-ray diffraction (XRD) and transmission electron microscopy (TEM) observations.

Table 2.1. Structures and optical transition energies of the studied samples

Sample	$a_{//}$ (Å)	$a_{\perp}$ (Å)	Thickness (nm)		PL peak position at 10 K (eV)	Calculated Eg at 0 K (eV)
			CdSe	CdTe		
A	6.103	6.101	10.52	1.51	1.04	1.05
B	6.097	6.120	5.47	0.88	1.18	1.22
C	6.096	6.096	5.99	0.75	1.30	1.26

2.3 Structures

High-resolution XRD measurements of the samples were performed for the symmetric (004) and asymmetric (113) reflections using the Cu $K\alpha_1$ radiation on a PANalytical X'Pert PRO Materials Research Diffractometer. Fig. 2.1 (a), (b), and (c) show the (004) ω-2θ diffraction patterns of samples A, B, and C, which respectively consists of 40, 40, and 50 periods of CdTe and CdSe layers. The lattice constants of GaSb and ZnTe are 6.096 Å and 6.105 Å, respectively, and the lattice constants of CdSe and CdTe are 6.052 Å and 6.482 Å, respectively. Therefore, the CdTe layer is compressively strained to the GaSb substrate or the ZnTe buffer layer, while the CdSe layer is tensilely strained. The high structural qualities of the samples are evidenced by the sharp satellite peaks and the absence of appreciable peak broadening. The lateral and average vertical lattice constants

$a_{//}$ and $a_{\perp}$ of the superlattices shown in Table 2.1 are determined from the zeroth superlattice peaks in the (004) and (113) XRD patterns, and the layer thicknesses are determined from the separation of the first-order superlattice peaks in the (004) XRD patterns. Sample A has a ZnTe buffer layer of approximately 200 nm, and the superlattice is strained as shown by its lateral and vertical lattice constants. The ZnTe buffer layers of samples B and C are about 10 nm thick, and the superlattice of sample B is strained while that of sample C is almost perfectly lattice matched to the substrate. It can also be seen in Fig. 2.1 that the superlattice peaks of sample B have the narrowest FWHM, indicating that this sample has minimal interface roughness as well as the fewest defects.

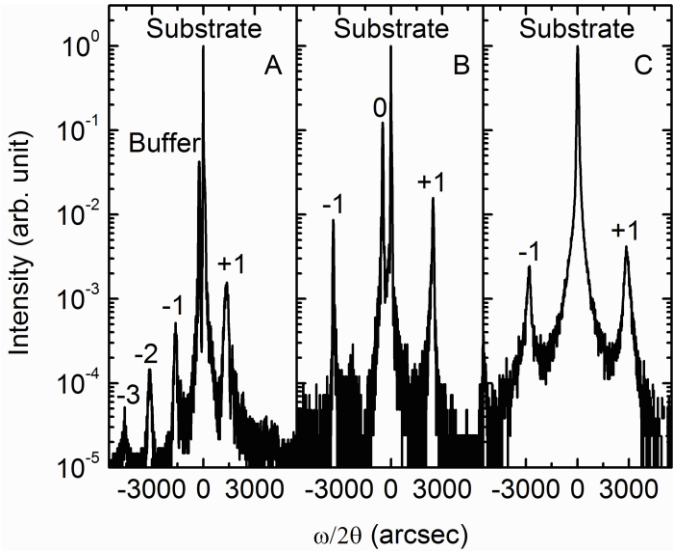

Fig. 2.1. X-ray (004) ω/2θ diffraction patterns of samples A , B , and C.

Specimens of sample B suitable for cross-sectional TEM observation were prepared by standard mechanical polishing, dimpling, and a final argon-ion-milling at reduced energy (2-2.5 keV), with the sample being held at liquid-

nitrogen temperature to minimize artifacts due to thermal or ion-beam damage during milling. The low magnification image shown in Fig. 2.2 (a) demonstrates the overall high structural-quality and regularity of the CdSe/CdTe superlattice. In addition, the satellite diffraction spot adjacent to the major diffraction spot visible in selected area electron diffraction pattern, as shown in the inset of Fig. 2 (a), confirms the uniformity of the layer thicknesses. The high-resolution lattice image of this same specimen shown in Fig. 2.2 (b) demonstrates very-high crystalline-quality at the atomic length scale.

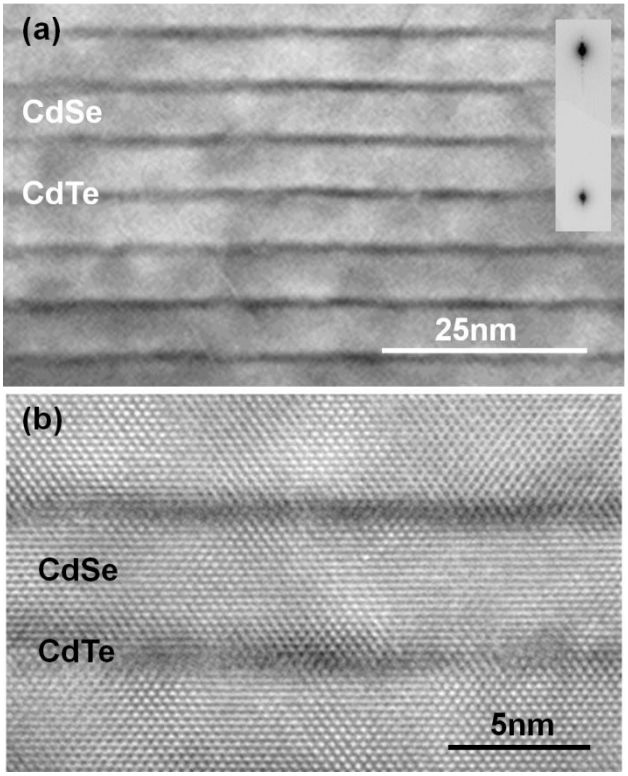

Fig. 2.2. Structural characterization of sample B using TEM. (a) Cross-sectional image showing regular superlattice periodicity and the absence of major structural defects, as confirmed by the selected area electron diffraction pattern shown in the inset. (b) High-resolution lattice image showing excellent crystallinity.

2.4 Photoluminescence

2.4.1 Steady-State Photoluminescence

It has been reported that the unstrained CdTe and CdSe forms a type-II band edge alignment [11], [12] with the respective bandgap energies 1.76 eV [12], [22] and 1.61 [12], [18], [26] eV at 10 K. The band edges of the superlattices are modified by the strain effects, and the superlattice minibands are formed as the hybridization of the bound states in the quantum wells coupled through the barriers. To study the impact of band alignment on the proposed superlattice materials, photoluminescence (PL) measurements of samples A, B, and C were performed using a 660-nm diode laser with an excitation power density of 180 W/cm^2. The PL signals were collected using a grating monochromator and measured using a Ge detector cooled to liquid nitrogen temperature. The PL of the three samples is observed at both room temperature and low temperature. The 10 K measurement results plotted in Fig. 2.3 show that the PL spectra of the three samples peak at different wavelengths due to the different superlattice period of each sample. The ground state transition energy of sample B shows the strongest PL intensity and the narrowest FWHM. Furthermore, due to the type-II band edge alignment between CdTe and CdSe (see Fig. 2.3 inset), the PL peak energies are considerably lower than the bandgap energy of either CdTe or CdSe.

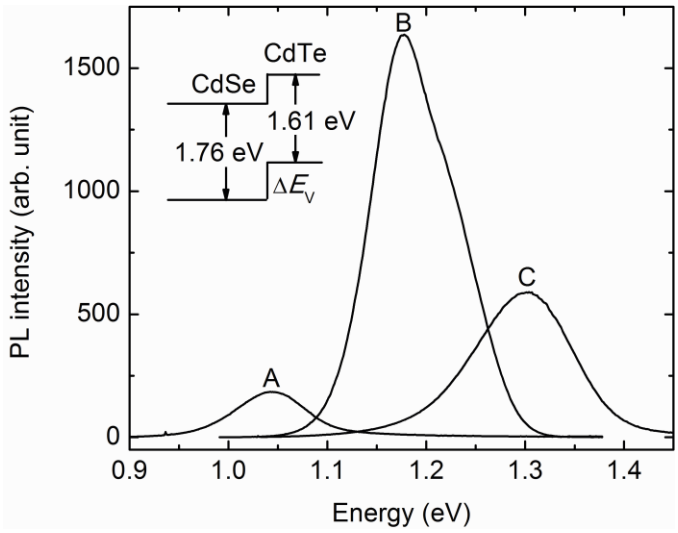

Fig. 2.3. Photoluminescence (PL) spectra of samples A, B, and C measured at 10 K. The difference in the PL peak positions is a result of the different layer thicknesses in each superlattice.

The conduction and valence band ground state energy levels of the three samples were calculated using the Kronig-Penney model [16], with the layer thicknesses given in Table 2.1, the material parameters shown in Table 2.2, and the valence band offset ΔE_V as a fitting parameter. The valence band offset ΔE_V determined by fitting the calculated ground state transition energies to the measured PL peak positions is 0.63 ± 0.06 eV, which agrees with the theoretical prediction of 0.57 eV [12] within the experimental error. The calculated ground state transition energies of the samples are in reasonable agreement with the measured PL peak positions as shown in Table 2.1.

Table 2.2. Material parameters for zinc-blende CdTe and CdSe [a: lattice constant, E_g: bandgap energy, VBO: valence band offset, m_e: electron effective mass, m_{hh}^z (m_{lh}^z) and m_{hh}^t (m_{lh}^z): heavy-hole (light-hole) effective mass in the growth direction and in plane, a_c, a_v and b: deformation potentials, ε: dielectric constant, C_{11} and C_{12} : elastic stiffness constants].

	a (Å)	E_g (eV)	VBO (eV) [14]	m_e	m_{hh}^t	m_{hh}^z	m_{lh}^t	m_{lh}^z
CdSe	6.052 [12]	1.76 [12], [22]	0.63	0.12 [17]	0.17 [21]	0.83 [21]	0.36 [21]	0.13 [21]
CdTe	6.482 [12], [24], [26]	1.61 [12], [18], [26]		0.088 [19]	0.14 [19], [20]	0.53 [19], [20]	0.28 [19], [20]	0.11 [19], [20]
	a_c (eV) [27]	a_v (eV) [27]	b (eV) [25]	ε	C_{11} (10^{11} dyne/cm^2)		C_{12} (10^{11} dyne/cm^2)	
CdSe	-3.77	-1.81	-0.8	9.6 [25]	8.8 [24]		5.3 [24]	
CdTe	-5.09	-2.14	-1	10.4 [25], [26]	5.35 [23], [24], [26]		3.68 [23], [24], [26]	

In order to further corroborate the type-II band alignment, the PL of sample C was measured at 10 K using a 488 nm Ar-ion laser, with the excess carrier concentration ranging from approximately 9.0×10^{15} cm^{-3} to 6.3×10^{18} cm^{-3}. As shown in Fig. 2.4 (a), the PL peak shifts to higher energy as the excess carrier concentration increases. This blue shift is caused by the spatial separation of electrons and holes generated by the optical excitation in the type-II superlattice. Figure 2.4 (b) shows the band edge alignments and the minibands of the conduction band and heavy-hole band as well as the ground state probability densities, at an excess carrier concentration of 6.3×10^{18} cm^{-3}. The electrons and holes are spatially separated as shown by their probability densities, and their Coulomb attraction pulls them toward the interfaces of the two materials. Consequently, the bands are bent towards the interfaces, pushing the minibands to

higher energies as the excess carrier concentration increases with increasing excitation power density. The blue shift in the PL peak is therefore the result of the enhanced band bending caused by the increased excess carrier concentration.

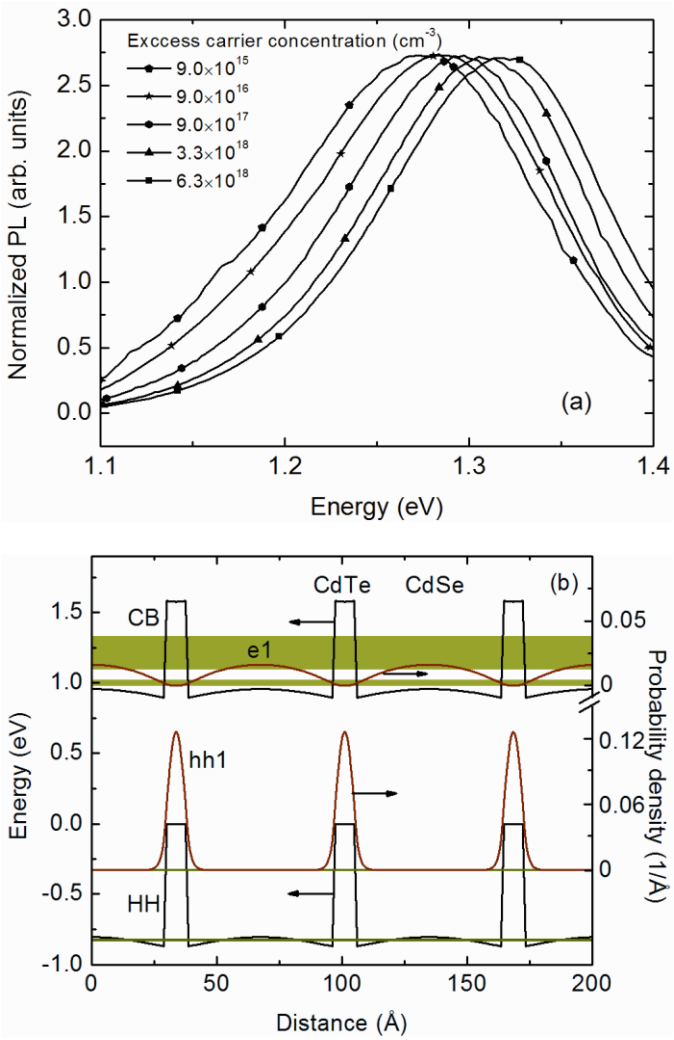

Fig. 2.4. (a) Steady-state photoluminescence spectra measured at 10 K with estimated excess carrier concentrations ranging from 8.3×10^{15} cm^{-3} to 6.3×10^{18} cm^{-3}. (b) Calculated band edge alignments (black), minibands (green), and the corresponding ground state probability densities of the conduction band and heavy-hole band (red) at a carrier concentration of 5.8×10^{18} cm^{-3}.

2.4.2 Time-Resolved Photoluminescence

The time-dependent PL decay of Sample C was measured at 10 K using time-correlated single photon counting and is shown in Fig. 2.5 for two optical excitation intensities. The excitation source was a 405 nm pulsed laser with a 50 ps pulse width and a 2.5 MHz repetition rate, and the detector was a Hamamatsu H10330-75 near infrared photomultiplier tube. The initial excess carrier concentrations are estimated to be 5.0×10^{18} cm^{-3} (red curve) and 4.0×10^{17} cm^{-3} (blue curve) using the measured laser powers of 554.0 mW and 44.3 mW, laser spot diameter of 15 μm, and the absorption coefficient of 1.5×10^{5} cm^{-1} measured using UV-visible variable-angle spectroscopic ellipsometry.

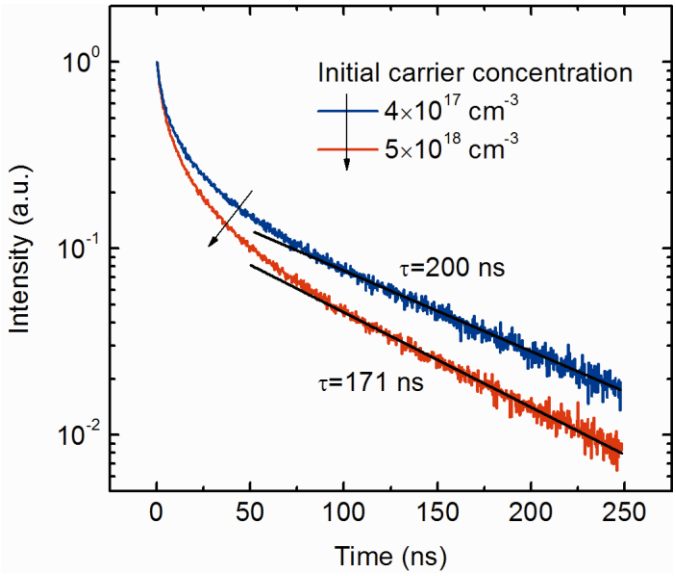

Fig. 2.5. Time-resolved photoluminescence decays of Sample C measured at 10 K with initial carrier concentrations on the order of 4×10^{17} cm^{-3} and 5×10^{18} cm^{-3}, respectively.

The PL decay evolves from a steep initial descent with a rapidly increasing instantaneous lifetime in the first 75 ns to a gradual decay with a single exponential tail. The strong dependence of carrier lifetime on the excess carrier concentration in the initial decay can be partly attributed to concentration-dependent recombination mechanisms such as radiative and Auger recombination. [28]. However, the similarity in the initial slopes of the PL decay curves, in spite of the very different initial excess carrier concentrations, suggests that other mechanisms are also involved in the initial steep PL decay, e.g. carrier diffusion and the direct band-to-band transition in CdSe as observed in steady-state PL on Sample B.

The excess carrier concentrations at the onset of the exponential decay tails are on the order of 10^{18} cm^{-3} (red curve) and 10^{17} cm^{-3} (blue curve) respectively. The net background doping concentration at room temperature is estimated to be below 10^{17} cm^{-3} from the free carrier absorption measured using an infrared variable angle spectroscopic ellipsometer. Therefore, the excess carrier concentrations at the onset of the exponential decay tails are assumed to be much larger than the background doping concentration considering carrier freeze-out at 10 K. In this case, the constant lifetimes in the exponential decay tails can be attributed to Shockley-Read-Hall (SRH) recombination, and the PL intensity has a quadratic dependence on the excess carrier concentration. The PL decay lifetimes are fit as 171 ns and 200 ns for the initial excess carrier concentrations of 5.0×10^{18} cm^{-3} and mid 4.0×10^{17} cm^{-3}, respectively. The slight difference

between the observed lifetimes may be due to the limited time range taken in the measurements, and the SRH lifetime is taken as 186 ns from the average of those fit values.

2.5 Modeling

The pronounced band bending effect shown in Fig. 2.4 (a) has been observed primarily in type-II quantum wells and quantum dots [11], [29]. In superlattices, however, the coupling between the quantum wells tends to reduce the charge localization and separation as shown by the probability densities in Fig. 2(b). To confirm the band bending effect in the type-II superlattice, self-consistent solutions of the Schrödinger and Poisson equations [16] are performed to model the increase of ground state transition energy with the accumulation of excess carriers.

The modeling starts with the calculation of strain effects on the band edges. The strain effects on the band edges are caused by a superposition of the hydrostatic strain δE_{hy} and shear strain δE_{sh},

$$\begin{aligned} \delta E_{hy} &= -a\left(2\varepsilon_{//} + \varepsilon_{zz}\right) \\ \frac{1}{2}\delta E_{sh} &= -\frac{b}{2}\left(2\varepsilon_{//} - 2\varepsilon_{zz}\right) \end{aligned} \tag{2.1}$$

where

$$\varepsilon_{//} = \frac{a_{sub} - a_{epi}}{a_{epi}} \tag{2.2}$$

$$\varepsilon_{zz} = -\frac{2C_{12}}{C_{11}}\varepsilon_{xx}$$

with C_{12} and C_{11} being the elastic stiffness constants, and $a=a_c-a_v$ is the hydrostatic deformation potential. The hydrostatic strain shifts the conduction band and valence band edges, while the shear strain splits the heavy-hole and light-hole bands,

$$\begin{aligned} \delta E_{C-HH} &= -\delta E_{hy} + \frac{1}{2}\delta E_{sh} \\ \delta E_{C-LH} &= -\delta E_{hy} - \frac{1}{2}\delta E_{sh} \end{aligned} \tag{2.3}$$

The superlattice minibands are formed as the hybridization of bound states of the quantum wells coupled through the barriers, which can be obtained by solving the Schrödinger equation

$$-\frac{\hbar^2}{2}\frac{d}{dz}\left[\frac{1}{m(z)}\frac{d}{dz}\right]\Psi(z) + \left[V_{SL}(z) - V_E(z)\right]\Psi(z) = E\Psi(z) \tag{2.4}$$

where m(z) is the effective mass in the growth direction z, Ψ(z) is the wave function of the energy state E, and V_{SL}(z) and V_E(z) are respectively the band edge alignment of the superlattice and the electrostatic potential induced by the charges. For a superlattice of N periods of a period L, the wave vector q has N values in the first Brillouin zone with the spacing of $2\pi/NL$ according to the envelope function approximation and the cyclic boundary condition. The energy states corresponding to $+q$ and $-q$ are degenerate. Eq. (2.4) is solved respectively for the conduction band, the heavy-hole band and the light-hole band using the

propagation matrix method, in order to obtain the energy states and wave functions corresponding to the wave vectors.

The charges accumulated under the optical excitation generate an electrostatic potential $V_E(z)$ as described by the Poisson equation

$$\frac{d}{dz}\left[\varepsilon(z)\frac{d}{dz}\right]V_E(z) = -|e|\left[p(z)-n(z)\right] \tag{2.5}$$

where ε(z) is the dielectric function and n(z) and p(z) are the electron and hole densities. The boundary conditions for a period of the superlattice is $V(L/2)=V(-L/2)=V_{QW}$. The electron concentration $n(z)$ is

$$n(z) = \sum_m \sum_n \left|\Psi_{nm}(z)\right|^2 N_{nm} \tag{2.6}$$

where $|\Psi_{nm}(z)|^2$ and N_{nm} are the electron probability density in the growth direction and the electron concentration perpendicular to the growth direction in the n^{th} energy state E_{nm} of the m_{th} miniband in the conduction band. The electron concentration perpendicular to the growth direction on the energy state E_{nm} is

$$N_{nm} = \frac{k_B T m_e}{\pi\hbar^2}\ln\left(1+e^{[F_N-E_{nm}]/k_B T}\right) \tag{2.7}$$

The electron quasi-Fermi level F_N can thus be solved using Eqs. (2.6) and (2.7) assuming the incident light is evenly absorbed in every period of the superlattice. The hole quasi-Fermi level F_P is obtained similarly considering both the heavy-hole and light-hole bands. Consequently, the electron concentration, the heavy-hole and light-hole concentrations are obtained, and Eq. (2.5) is solved for the electrostatic potential V_E(z). This procedure of solving the coupled Schrödinger

and Poisson equations is iterated until it converges. The flow chart of the calculation program is shown in Fig. 2.6.

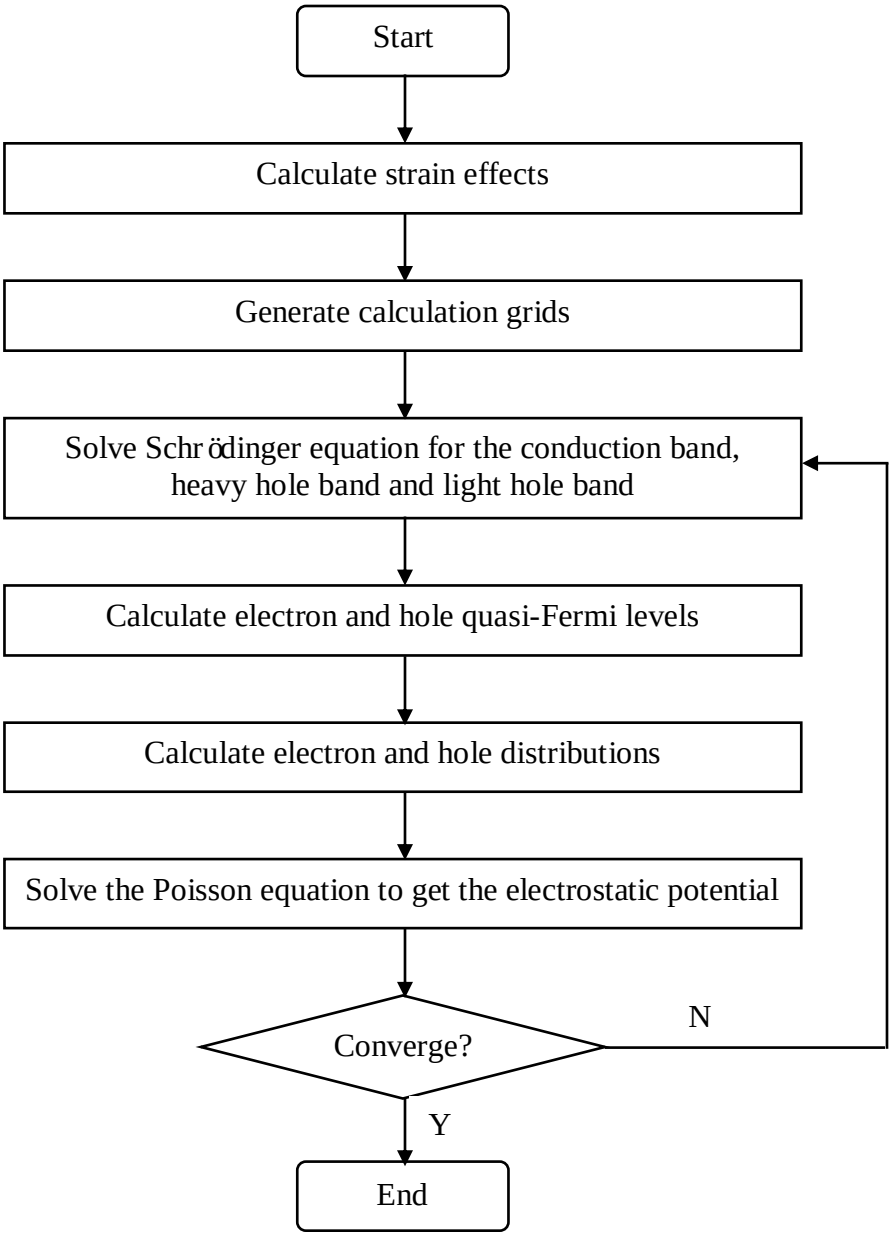

Fig. 2.6. Program flow chart of self-consistently solving the Schrödinger and Poisson equations.

The material parameters used in the calculations are shown in Table 2.3. The absorption coefficient and the surface reflectivity at the 488 nm laser wavelength are 10^5 cm^{-1} and 28% respectively, as determined from the ellipsometry measurements. The electron and hole concentrations are assumed to be uniform due to carrier diffusion. The surface recombination is not expected to be significant because of the strong hole confinement in the structure. The carrier lifetime used in the calculations is 186 ns as obtained from the TRPL measurements, because most of the carrier concentrations that caused the blue shift in the PL peak position are in the range of carrier concentrations that exist during the PL decay tails.

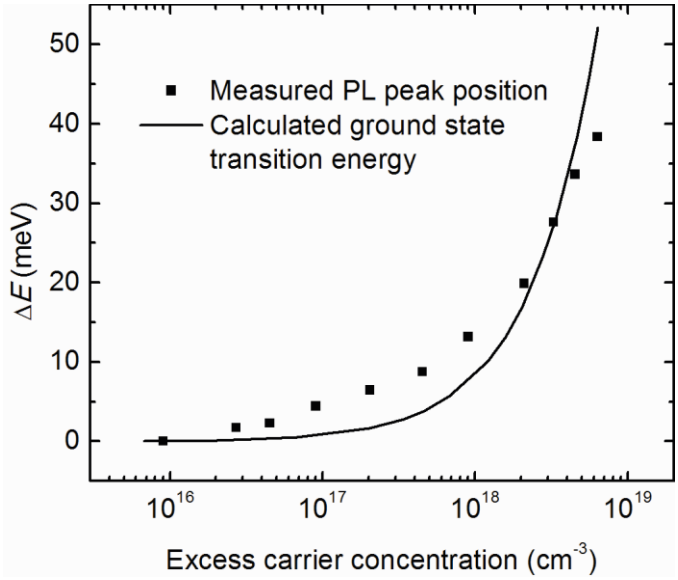

Fig. 2.7. The blue shift ΔE in the measured PL peak position and the calculated ground state transition energy as a function of the excess carrier concentration.

The calculated ground state transition energy is compared with the blue shift in PL peak position as a function of the excess carrier concentration in Fig. 2.7. The calculated ground state transition energy increases by 52 meV, which is in reasonable agreement with the 40 meV blue shift observed in the PL peak position. The larger blue shift of measured PL peak position at low carrier concentrations could be caused by the filling of the tail states below the band edges, which is not considered in the calculations. The smaller blue shift of the measured PL peak position at large carrier concentrations could be attributed to the decrease of carrier lifetime due to the increase of wave function overlap at the high excitation levels.

References

[1] Y.-H. Zhang, S.-N. Wu, D. Ding, S.-Q. Yu, S. R. Johnson, "A proposal of monolithicly integrated multijunction solar cells using lattice-matched II/VI and III/V semiconductors," in *Proc. 33th IEEE PVSC*, San Diego, 2008, pp. 1–5.

[2] S. Wang, D. Ding, X. Liu, X.-B. Zhang, D. J. Smith, J.K. Furdyna, Y.-H. Zhang, "MBE growth of II-VI materials on GaSb substrates for photovoltaic applications," *J. Cryst. Growth*, vol. 311, pp. 2116–2119, Mar. 2009.

[3] J. Fan, L. Ouyang, X. Liu, D. Ding, J. K. Furdyna, D. J. Smith, and Y.-H. Zhang, "Growth and material properties of ZnTe on GaAs, InP, InAs and GaSb (001) substrates for electronic and optoelectronic device applications," *J. Cryst. Growth*, vol. 323, pp. 127–131, May 2011.

[4] S.-N. Wu, D. Ding, S. R. Johnson, S.-Q. Yu, and Y.-H. Zhang, "Four-junction solar cells using lattice-matched II-VI and III-V semiconductors," *Prog. Photovoltaics Res. Appl.*, vol. 18, pp. 328–333, Aug. 2010.

[5] N. Matsumura, T. Sakamoto, and J. Saraie, "Growth conditions in molecular beam epitaxy for controlling CdSeTe epilayer composition," *J. Cryst. Growth*, vol. 251, pp. 602–606, Apr. 2003.

[6] Y.P. Chen, G. Brill and N.K. Dhar, "MBE growth of CdSeTe/Si composite substrate for long-wavelength IR HgCdTe applications," *J. Cryst. Growth*, vol. 252, pp. 270–274, May 2003.

[7] G. Brill, Y. Chen, P. M. Amirtharaj, W. Sarney, D. Chandler-Horowitz, and N. K. Dhar, "Molecular beam epitaxial growth and characterization of Cd-based II–VI wide-bandgap compounds on Si substrates," J. Electron. Mater., vol. 34, pp. 655–661, 2005.

[8] F. Z. Amir, K. Clark, E. Maldonado, W. P. Kirk, J. C. Jiang, J. W. Ager III, K. M. Yu, W. Walukiewicz, "Epitaxial growth of CdSexTe1−x thin films on Si(1 0 0) by molecular beam epitaxy using lattice mismatch graded structures," *J. Cryst. Growth*, vol. 310, pp. 1081–1087, Mar. 2008.

[9] I. L. Kuskovsky, C. Tian, G. F. Neumark, J. E. Spanier, I. P. Herman, W.-C. Lin, S. P. Guo, and M. C. Tamargo, "Optical properties of δ-doped ZnSe: Te grown by molecular beam epitaxy: The role of tellurium," *Phys. Rev. B*, vol. **63**, 155205, 2001.

[10] Y. Gu, Igor L. Kuskovsky, M. van der Voort, G. F. Neumark, X. Zhou, and M. C. Tamargo, "Zn-Se-Te multilayers with submonolayer quantities of Te: Type-II quantum structures and isoelectronic centers," *Phys. Rev. B*, vol. **71**, 045340, 2005.

[11] C. H. Wang, T. T. Chen, K. W. Tan, Y. F. Chen, C. T. Cheng, and P. T. Chou, "Photoluminescence properties of CdTe/CdSe core-shell type-II quantum dots," *J. Appl. Phys.*, vol. 99, 123521, 2006.

[12] S.-H. Wei, S. B. Zhang, and A. Zunger, "First-principles calculation of band offsets, optical bowings, and defects in CdS, CdSe, CdTe, and their alloys," *J. Appl. Phys.*, vol. 87, 1304, 2000.

[13] X. Zhang, S. Wang, D. Ding, X. Liu, J.-H. Tan, J. K. Furdyna, Y.-H. Zhang, and D.J. Smith, "Structural characterization of integrated II–VI and III–V heterostructures for solar cell applications," J. Electron. Mater., vol. 38, pp. 1558–1562, 2009.

[14] J.-J. Li, X. Liu, Shi Liu, S. Wang, D. J. Smith, D. Ding, S. R. Johnson, J. K. Furdyna, and Y.-H. Zhang, "CdSe-CdTe type-II superlattices grown on GaSb substrates by molecular beam epitaxy," *Appl. Phys. Lett.*, vol. 100, 121908, 2012.

[15] J.-J. Li, L. Yin, S. R. Johnson, B. Skromme, S. Wang, X. Liu, D. Ding, C.-Z. Ning, J. K. Furdyna and Y.-H. Zhang, "Photoluminescence studies of type-II CdTe-CdSe superlattices," *Appl. Phys. Lett.*, accepted.

[16] S. L. Chuang, *Physics of Optoelectronic Devices*, New York: Wiley, 1995.

[17] Y. D. Kim, M. V. Klein, S. F. Ren, Y. C. Chang, H. Luo, N. Samarth, and J. K. Furdyna, "Optical properties of zinc-blende CdSe and ZnxCd1-xSe films grown on GaAs," *Phys. Rev. B*, vol. 49, pp. 7262–7270, 1994.

[18] J. Camassel and D. Auvergne, "Temperature dependence of the fundamental edge of germanium and zinc-blende-type semiconductors," *Phys. Rev. B*, vol. 12, pp. 3258–3267, 1975.

[19] L. S. Dang, G. Neu and R. Romestain, "Optical detection of cyclotron resonance of electron and holes in CdTe," *Solid State Comm.*, vol. 44, pp. 1187–1190, Nov. 1982.

[20] P. Lawaetz, "Valence-Band Parameters in Cubic Semiconductors," *Phys. Rev. B*, vol. 4, pp. 3460–3467, 1971.

[21] M. Willatzen, M. Cardona and N. Christensen, "Spin-orbit coupling parameters and electron g factor of II-VI zinc-blende materials," *Phys. Rev. B*, vol. 51, pp. 17992–17994, 1995.

[22] W. Shan, J. Song, H. Luo and J. Furdyna, "Determination of the fundamental and split-off band gaps in zinc-blende CdSe by photomodulation spectroscopy," *Phys. Rev. B*, vol. 50, pp. 8012–8015, 1994.

[23] H. J. McSkimin and D. G. Thomas, "Elastic Moduli of Cadmium Telluride," *J. Appl. Phys.*, vol. 33, pp. 56–59, 1962.

[24] E. Deligoz, K. Colakoglu, and Y. Ciftci, "Elastic, electronic, and lattice dynamical properties of CdS, CdSe, and CdTe," *Physica B*, vol. 373, pp. 124–130, Mar. 2006.

[25] S. Adachi, *Properties of Group-IV, III-V and II-VI Semiconductors*, Chichester : Wiley, 2005.

[26] A. J. Strauss, "The physical properties of Cadmium Telluride," *Rev. Phys. Appl.*, vol. 12, pp. 167–184, 1977.

[27] S.-H. Wei and A. Zunger, "Predicted band-gap pressure coefficients of all diamond and zinc-blende semiconductors: Chemical trends," *Phys. Rev. B*, vol. 60, pp. 5404–5411, 1999.

[28] B. C. Connelly, G. D. Metcalfe, Hongen Shen and M. Wraback, "Direct minority carrier lifetime measurements and recombination mechanisms in long-wave infrared type II superlattices using time-resolved photoluminescence," *Appl. Phys. Lett.*, vol. 97, 251117, 2010.

[29] N. N. Ledentsov, J Böhrer, M. Beer, F. Heinrichsdorff, M. Grundmann and D. Bimberg, "Radiative states in type-II GaSb/GaAs quantum wells," *Phys. Rev. B*, vol. 52, pp. 14058–14066, 1995.

III CONTACT GRID DESIGN

3.1 Introduction

The optimization of front contact layout is critical for improving the efficiency of concentrator solar cells. The minimum power loss (MPL) method [1]–[5], or similarly the maximum power output (MPO) method [6]–[9], has been used to optimize the finger spacing and bus bar width in order to maximize the efficiency. However, there are some assumptions in these methods that should be put under scrutiny. In this Chapter, these assumptions are carefully examined and a rigorous MPO method based on the distributed series resistance model (MPODSR) is proposed. Unlike the conventional methods, this method does not need any prerequisite knowledge of the operating voltage and current density.

3.2 Minimum Power Loss Method

The MPL method is taken as an example to examine the assumptions in the conventional methods. In the MPL method, the total power loss associated with the front contact is divided into the shadowing loss caused by the reflection of light from the metal contact and the Joule heating loss generated on the series resistance by the current flow. The shadowing loss p_{sh} is defined as

$$p_{sh} = \frac{P_{in} A_{metal}}{P_{in} A_{cell}} = \frac{A_{metal}}{A_{cell}} \ , \tag{3.1}$$

where P_{in} is the power density of the incident light and A_{metal} and A_{cell} are the areas of the metal contact and the solar cell respectively. To make its definition

consistent with the series resistance loss, p_{sh} is defined alternatively with respect to the electric power

$$p_{sh} = \frac{J_m V_m A_{metal}}{J_m V_m A_{cell}} = \frac{A_{metal}}{A_{cell}} \quad , \tag{3.2}$$

where J_m and V_m are the current density and voltage measured at the operating point. The series resistance loss p_{sr} is defined as

$$p_{sr} = \frac{\sum_{i=1}^{3} \int_{l_i} I_{sri}^2 dR_{si}}{J_m V_m A_{cell}}, \tag{3.3}$$

where R_{si} is the semiconductor series resistance, the metal series resistance or the contact resistance, and I_{sri} is the current flowing through the path l_i of the respective series resistance.

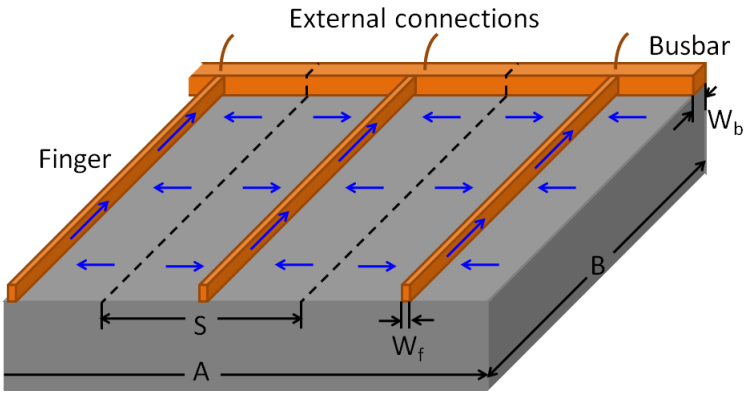

Fig. 3.1. Contact layout and current flow directions of a square solar cell.

To facilitate the discussions, we will consider a square solar cell with a busbar at one edge and fingers perpendicular to the busbar as shown in Fig. 3.1. The solar cell is divided into unit cells of identical areas shown by the dashed

lines. Since the finger length is usually much longer than the finger spacing, it is assumed that the current generated at the junction flows laterally in the emitter and is collected by the fingers. For simplicity, the current loss due to surface recombination is not considered here.

For the contact pattern in Fig. 3.1, the shadowing loss is

$$p_{\mathrm{srs}} = \frac{W_{\mathrm{f}}\left(B - W_{\mathrm{b}}\right)}{BS} + \frac{W_{\mathrm{b}}}{B}. \tag{3.4}$$

The semiconductor series resistance loss, metal series resistance loss and contact resistance loss are given by

$$p_{srs} = \frac{\int_0^{\frac{S}{2}} \left(J_{\mathrm{m}} B y\right)^2 \rho_{\mathrm{s}} / B \, dy}{J_{\mathrm{m}} V_{\mathrm{m}} B S / 2}, \tag{3.5}$$

$$p_{\mathrm{srm}} = \frac{\int_0^{B} \left(J_{\mathrm{m}} S x\right)^2 \rho_{\mathrm{m}} / W_{\mathrm{f}} \, dx}{J_{\mathrm{m}} V_{\mathrm{m}} BS} \tag{3.6}$$

and

$$p_{\mathrm{src}} = \frac{\left(J_{\mathrm{m}} BS\right)^2 \rho_{\mathrm{c}} / \left(BW_{\mathrm{f}}\right)}{J_{\mathrm{m}} V_{\mathrm{m}} BS}, \tag{3.7}$$

respectively, where ρ_{srs}, ρ_{srm} and ρ_{src} are the emitter sheet resistance, the metal sheet resistance and the contact resistance.

There are several assumptions in J_{m} and V_{m} in Eqs. (3.5)-(3.7). Firstly, in practice, J_{m} and V_{m} are usually measured from one or more prototype devices [3]–[5] as input parameters for the series resistance losses. However, since J_{m} and V_{m} vary with the contact pattern, the series resistance losses in Eqs. (3.5)-(3.7) are

only valid for the devices with finger spacing close to that of the prototype devices. Secondly, because there is only dark recombination current underneath the metal contact, J_m obtained by averaging the operating current over the entire solar cell area underestimates the current density in the open areas between the fingers. Furthermore, for a certain contact pattern, the local J_m and V_m vary at each point along the path of lateral current flow. Under illumination, the lateral current flow in the emitter causes an increase in the junction voltage from the center to the edges of a unit cell. Therefore, V_m measured from the contact terminals is less than the local junction voltage in the open areas. Due to the increased junction voltage, the recombination current density is increased near the edges of the unit cell. Nevertheless, the recombination current density is much less than the photocurrent density at the operating point for most solar cells with optimal contact patterns. It is therefore reasonable to assume that the junction current density is uniform in the open areas. If the finger spacing is too large, however, the junction voltage may build up so much that it causes a significant increase in the recombination current density near the edges of the unit cell. Consequently, the junction current density may not be uniform in the open areas. This effect of large recombination current will be referred to as the diode loss hereafter. The diode loss in conjunction with the series resistance loss causes the fingers to be placed close together, at the expense of the increased shadowing effect. The optimal finger spacing is therefore a tradeoff between these conflicting

criteria. In the conventional design methods, the neglect of diode loss may cause the finger spacing to be larger than the optimal finger spacing.

3.3 Maximum Power Output Method Based on the Distributed Series Resistance Model

Considering the effects discussed above, the contact grid optimization can be achieved by maximizing the output power using the distributed series resistance model [10]. For a solar cell of a particular size, the finger spacing and thus the number of unit cells are varied in order to find the maximum output power at the external connection. The equivalent circuit of a unit cell is shown in Fig. 3.2. Each of the open areas in the unit cell is divided into many slices in the direction of lateral current flow. Every slice has the photocurrent dI_{ph}, the recombination currents dI_{r1} in the quasineutral region and dI_{r2} in the depletion region, the lateral emitter resistance dR_l and the vertical base plus back contact resistance dR_b. The substrate resistance is negligible for highly doped GaAs substrates. Underneath the finger, the vertical emitter resistance is R_{ef}, the base plus back contact resistance is R_{bf}, and the recombination currents are I_{r1f} and I_{r2f}. For simplicity, the series resistance and contact resistance of the finger are lumped into a resistance R_f. In Fig. 3.1, the busbar is bonded to the external connection at the end of every finger, so there is no lateral current flow in the busbar and it does not generate any series resistance loss. The busbar width is therefore set to the minimum width necessary for bonding to reduce its shadowing loss. A program using Matlab and SPICE is developed to simulate the equivalent

circuit and find out the optimum finger spacing where the output power is maximized. The parameters of a p/n GaAs solar cell used in this study are shown in Table 3.1.

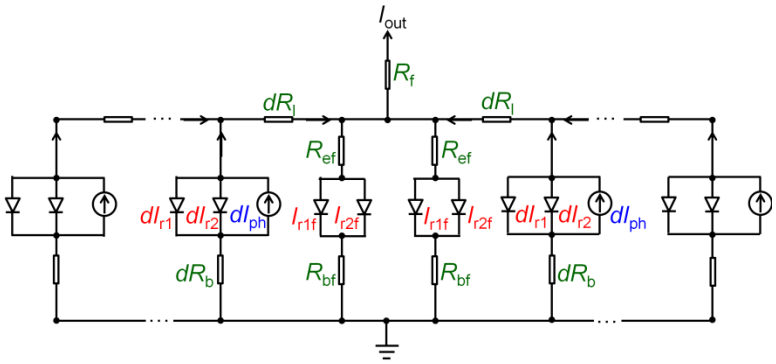

Fig. 3.2. Equivalent circuit of a unit cell based on the distributed series resistance model.

Table 3.1 Parameters of the GaAs solar cell [7], [9], [11]

Area (cm^2)	1×1	Emitter thickness (μm)	0.7
Base thickness (μm)	3.8	Emitter doping (cm^{-3})	2.5×10^{18}
Base doping (cm^{-3})	5×10^{17}	Emitter sheet resistance (Ω/□)	300
Base resistivity (Ωcm)	4×10^{-3}	J_{01} (mA/cm^2)	10^{-16}
J_{02} (mA/cm^2)	10^{-8}	n_1	1
n_2	2	J_{ph} (mA/cm^2)	27
Contact resistance (Ωcm^2)	10^{-5}	Finger line resistance (Ω/cm)	0.1
Finger width (μm)	5	Busbar width (μm)	100

Fig. 3.3 shows the power losses for the MPL method for the GaAs solar cell at 1000 suns concentration. It can be seen in Fig. 3.3 that the series resistance loss in Eq. (3.3) increases to about 100% at the finger spacing of 400 μm,

showing that the absolute power loss on the series resistance is about the same as the output power.

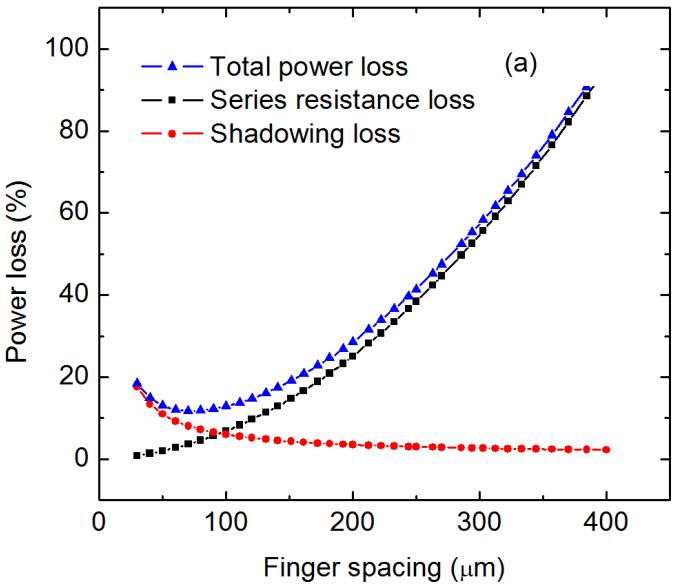

Fig. 3.3. Calculated power losses of the GaAs solar cell under 1000 suns concentration using the MPL method.

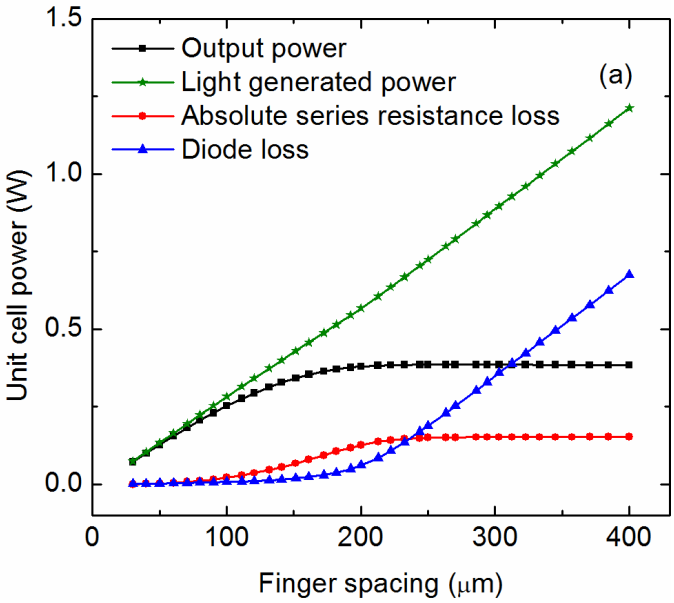

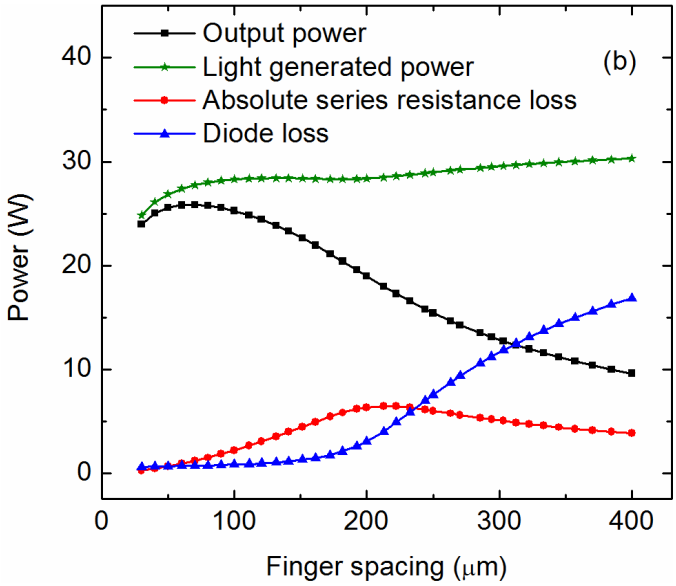

Fig. 3.4. Calculated light generated power and its allocation between the output power and power losses of (a) a unit cell and (b) the entire GaAs solar cell under 1000 suns concentration using the MPODSR method.

Fig. 3.4 shows the light generated power and its allocation between the output power and power losses of a unit cell (a) and the entire GaAs solar cell (b) calculated using the MPODSR method at 1000 suns concentration. In Fig. 3.4(a), it can be seen as the light generated power increases almost linearly with the finger spacing, the absolute series resistance loss increases and saturates, while the diode loss starts to increase linearly at the finger spacing around 200 μm. The output power also starts to saturate at about 200 μm, because the light generated power is all consumed by the diode loss. The finger spacing 200 μm can therefore be considered as the critical finger spacing, above which the increase of the open area does not produce any extra power. In Fig. 3.4(b), the output power and

absolute series resistance loss of the entire solar cell are reduced above the critical finger spacing, because the unit cell number decreases with the increased finger spacing.

The monotonic increase in the series resistance loss for the MPL method is due to the assumption of uniform junction current density in the open areas. This assumption is valid only when the local junction voltages in the open areas are sufficiently small such as at the operating points of most solar cells with optimized contact patterns. Fig. 3.5(a) shows the lateral distribution of junction voltage of a unit cell with the optimal finger spacing of 68 μm at 1000 suns concentration calculated using the distributed series resistance model. It can be seen that the local junction voltage increases by about 40 mV from the center to the edges of the unit cell, which is larger than kT/q reported previously [12], [13] for the optimum finger spacing. The voltage on the finger in the center of the unit cell is uniform. Due to the increased junction voltage, the recombination current density increases from the center to the edges of the unit cell as shown in Fig. 3.5(b). However, the recombination current density is still negligible compared to the photocurrent density. Therefore, the lateral current density increases linearly from the edges to the center of the unit cell.

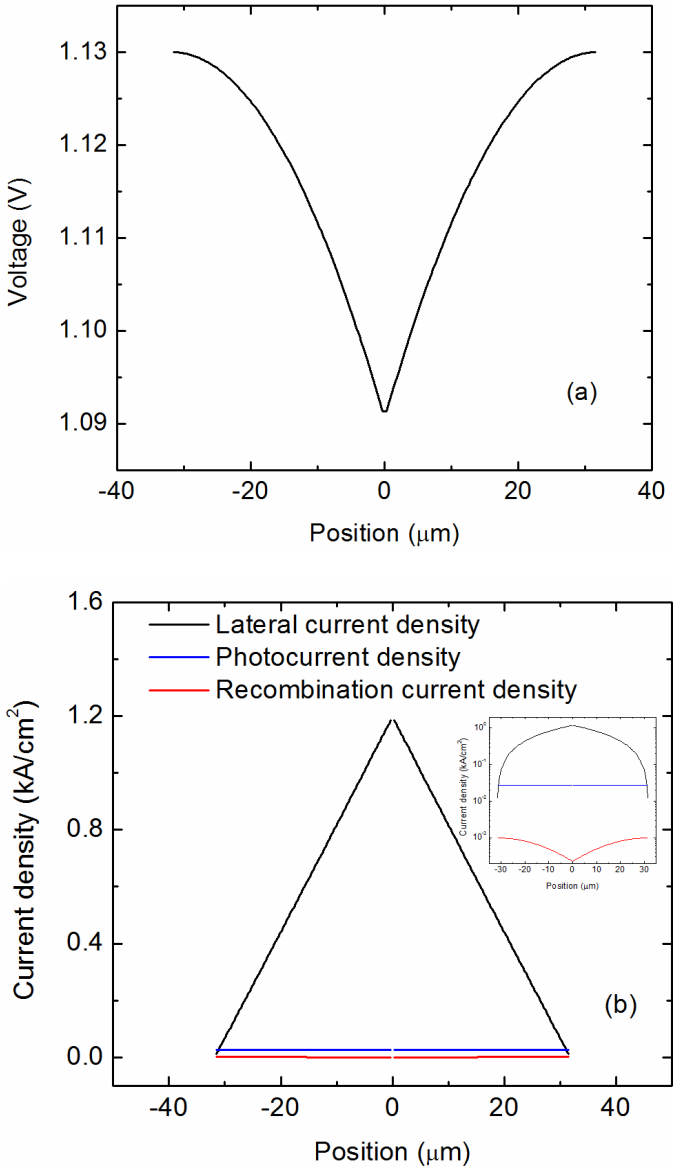

Fig. 3.5 (a) Lateral voltage distribution and (b) the distributions of lateral current density, photocurrent density and recombination current density in a unit cell with the optimal finger spacing at 1000 suns concentration.

If the finger spacing is larger than the critical finger spacing, however, the nonuniform recombination current density in a unit cell may significantly affect

the current collected by the finger at the operating point. For instance, at the finger spacing of 400 μm and 1000 suns concentration as shown in Fig. 3.6(a), the local junction voltage increases by about 370 meV from the center to the edges of the unit cell due to the lateral current flow. The junction voltage becomes saturated near the edges of the unit cell, because the recombination current consumes nearly all the photocurrent in those areas as shown in Fig. 3.6(b). Consequently, there is little lateral current flow in those areas.

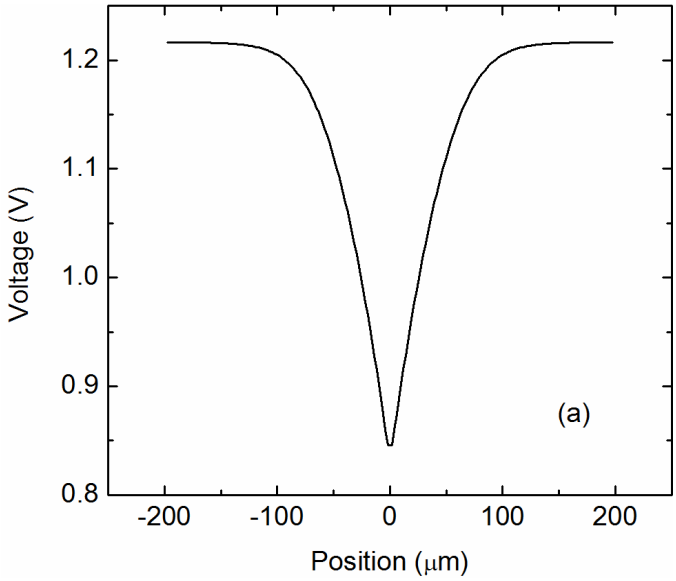

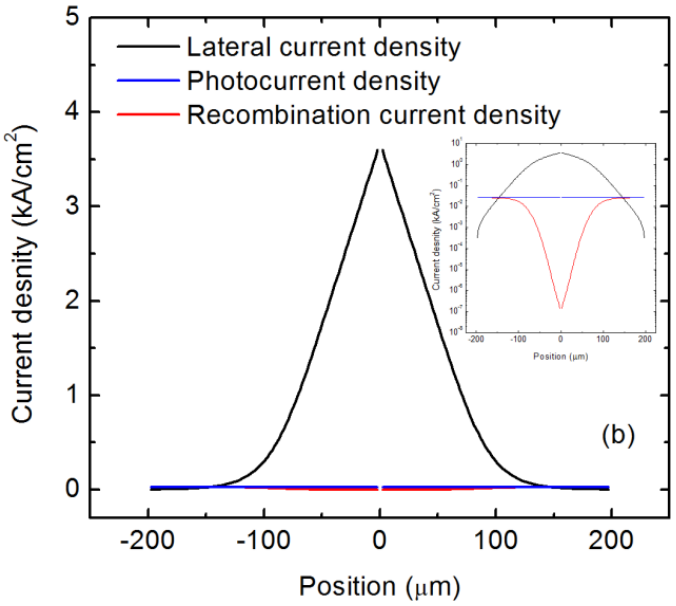

Fig. 3.6. (a) Lateral voltage distribution and (b) the distributions of lateral current density, photocurrent density and recombination current density in a unit cell with large finger spacing at 1000 suns concentration.

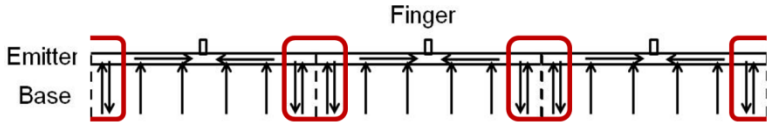

Fig. 3.7. Schematic cross section of a solar cell showing the photocurrent depletion effect.

This effect of photocurrent depletion shown in Fig. 3.6(b) can be visualized with the schematic cross section of the solar cell in Fig. 3.7. The areas near the edges of the unit cell produce little power because almost all the photogenerated carriers are recombined at the junction. This effect is equivalent to the shadowing effect although there is no metal coverage in this area. Fig. 3.8

compares the optimal finger spacing and critical finger spacing of the GaAs solar cell calculated by MPODRS method under various concentrations. It can be seen that the difference between the critical finger spacing and optimal finger spacing decreases rapidly with the increase of concentration. The photocurrent depletion effect can be used to explain the concentration dependent series resistance [15]. Under concentrations, the semiconductor series resistance depending on the lateral current path is one of the major contributors to the total series resistance. It can be seen from Fig. 3.8 if a solar cell with the finger spacing optimized at 100 suns is to work at above 1000 suns concentrations, the finger spacing becomes larger than the critical finger spacing. Therefore, the lateral current path may be reduced due to the photocurrent depletion, causing the decrease in the series resistance. It indicates that the superposition principle does not hold when the concentration level is varied in a large range.

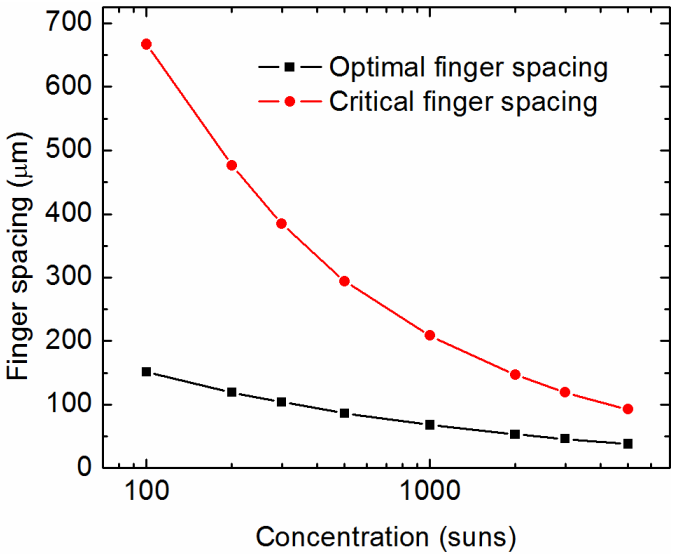

Fig. 3.8 Comparison of the optimal finger spacing and critical finger spacing of the GaAs solar cell calculated by MPODRS method under various concentrations.

3.4 Comparisons of the Methods

Fig. 3.9 compares the optimal finger spacing and maximum efficiency of the GaAs solar cell at various concentrations calculated using the MPL method and MPODRS method. It can be seen that the optimal finger spacing and maximum efficiency calculated by the former method are larger than those of the latter one due to the neglect of diode loss in the latter. Nevertheless, the optimal finger spacing and maximum efficiency determined by the two methods are close. It should be noted that the operating current density and voltage used in the calculation of MPL method is obtained from the contact pattern optimized using the MPODRS method. In practice, the prototype devices used for the MPL method may not have optimal contact patterns, and it may take several iterations for the optimization.

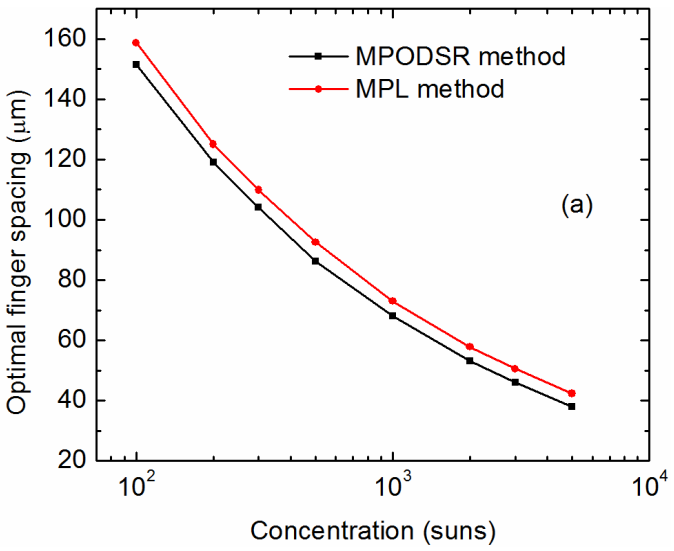

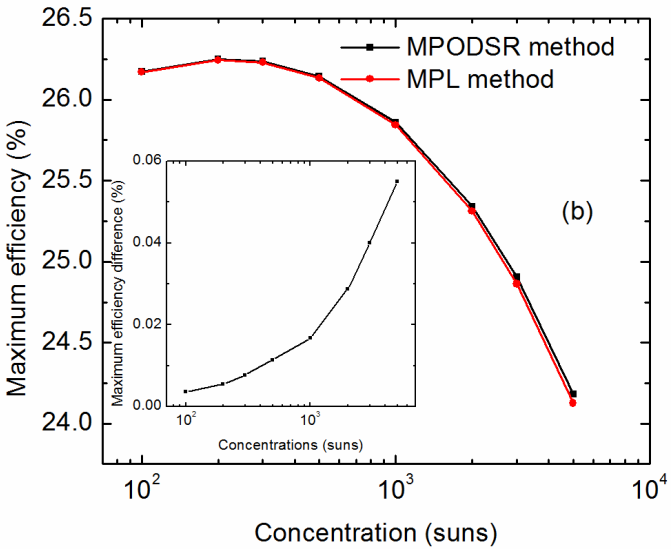

Fig. 3.9. (a) Comparisons of optimal finger spacing and (b) maximum efficiency of the GaAs solar cell calculated by the MPL method and MPODRS method under various concentrations.

The difference between the two methods is dependent on the series resistance and saturation currents of solar cells. Because the fingers can be put further apart for smaller series resistance and saturation currents, the series resistance loss and diode loss become more significant than the shadowing loss, and the difference between the two methods is larger due to the simplified assumptions in the MPL method. For instance, if a ZnO window layer with the parameters in Table 3.2 is put on the GaAs solar cell, the sheet resistance of the current collecting layer is reduced owing to the low resistivity of the ZnO layer. The differences in the optimal finger spacing and maximum efficiency calculated with the two methods are increased as shown in Fig. 3.10(a) and (b), assuming there is no optical loss caused by the ZnO window layer.

Table 3.2 Parameters of the ZnO window layer.

Thickness (μm)	0.1	Doping (cm^{-3})	5×10^{20}
Sheet resistance (Ω/□)	50	Contact resistance (Ωcm^2)	10^{-5}

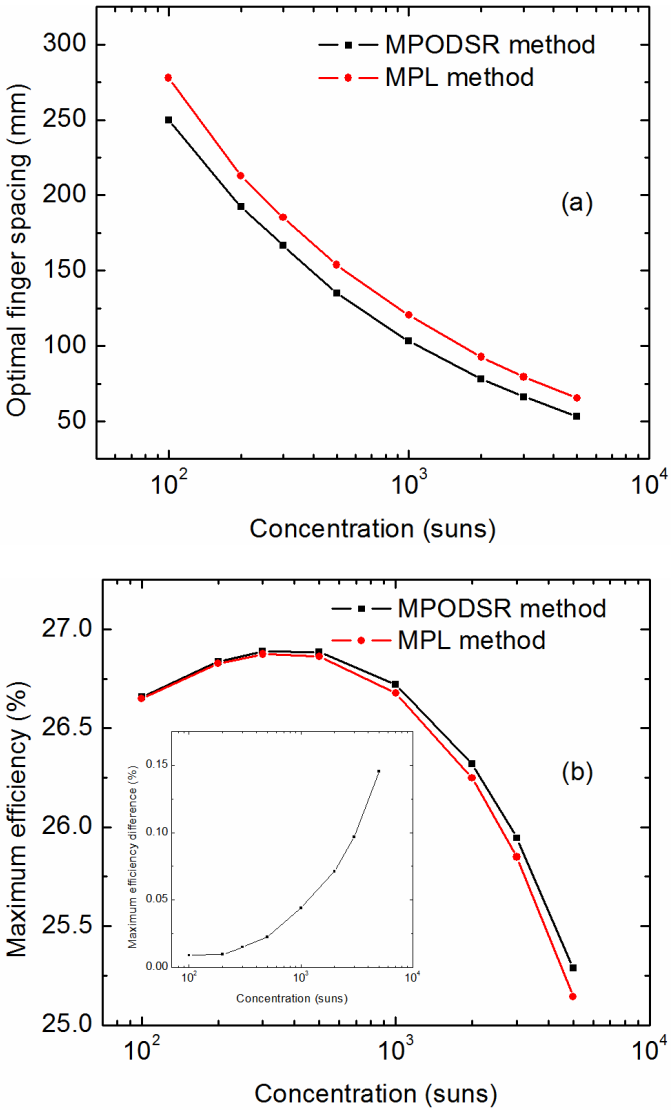

Fig. 3.10. (a) Comparisons of optimal finger spacing and (b) maximum efficiency of the GaAs solar cell with a ZnO window layer calculated by the MPL method and MPODRS method under various concentrations.

References

[1] H.B. Serreze, "Optimizing Solar Cell Performance by Simultaneous Consideration of Grid Pattern Design and Interconnect Configuration," in *Proc. 13th PVSC*, Washington, pp. 609–614, Jun. 1978.

[2] A.R. Moore, "An Optimized Grid Design for a Sun-Concentrator Solar Cell," *RCA Review*, vol. 40, pp. 140–152, Jun. 1979.

[3] M.A. Green, *Solar Cells: Operating Principles, Technology, and System Applications*, Englewood Cliffs: Prentice- Hall, 1982.

[4] T.A. Gessert and T.J. Coutts, "Grid Metallization and Antireflection Coating Optimization for Concentrator and One-sun Photovoltaic Solar Cells," *J. Vac. Sci. Technol. A*, vol. 10, no. 4, pp. 2013–2024, Jul. 1992.

[5] P. Morvillo, E. Bobeico, F. Formisano and F. Roca, "Influence of metal grid patterns on the performance of silicon solar cells at different illumination levels," *Mater. Sci. Eng. B*, vol. 159-160, pp. 318–321, Mar. 2009.

[6] L.S. Napoli, G.A. Swartz, S.G. Liu, N. Klein, D. Fairbanks and D. Tamutus, "High Level Concentration of Sunlight on Silicon Solar Cells," *RCA Review*, vol. 38, pp. 76–108, 1977.

[7] U. Blieske, U. Blieske, A. Baldus, A. Bett, F. Lutz, T. Nguyen, Ch. Schetter, K. Schitterer, O.V. Sulima and W. Wettling, "Concentrator Module Cased on LPE-Grown GaAs Solar Cells," in *Proc. 23rd IEEE PVSC*, Louisville, pp. 735–740, May 1993.

[8] A.R. Burgers, "How to Design Optimal Metallization Patterns for Solar Cells," *Prog. Photovoltaic. Res. Appl.*, vol. **7**, no. 6, pp. 457–461, Dec. 1999.

[9] A.R. Burgers and J.A. Eikelboom, "Optimizing Metalization Patterns for Yearly Yield," in *Proc. 26th IEEE PVSC*, Anaheim, pp. 219–212, Sep. 1997.

[10] B. Galiana, C. Algora, and I. Rey-Stolle, "Comparison of 1D and 3D analysis of the front contact influence on GaAs concentrator solar cell performance," *Sol. Energ. Mat. Sol. C.*, vol. 90, pp. 2589–2640, Apr. 2006.

[11] H.F. MacMillan, H.C. Hamaker, N.R. Kaminar, M.S. Kuryla, M.L. Ristow, D.D. Liu, G.F. Virshup and J.M. Gee, "28% Efficient GaAs Concentrator

Solar Cells," in Proc. 20th IEEE PVSC, Las Vegas, pp. 462–468, Sep. 1988.

[12] S. M. Sze, *Physics of Semiconductor Devices*, 2nd ed., New York: Jon Wiley & Sons, 1981.

[13] J.L. Boone and T.P. van Doren, "On the analysis and design of grid structures for p-n junction solar cells," in *Proc. J. Conf. Amer. Sect. International Sol. Energ. Soc. Sol. Energ. Soc. Can*., Cape Canaveral, vol. 10, pp. 212–217, Aug.1976.

[14] J.R. Hauser and P.M. Dunbar, "Performance limitations of silicon solar cells," *IEEE T Electron Dev*, vol. 24, no. 4, pp. 305–321, Apr. 1977.

[15] A.G. Aberle, S.R. Wenham and M.A. Green, "A new method for accurate measurements of the lumped series resistance of solar cells," *Proc. 23th IEEE PVSC*, Louisville, pp. 133–139, May 1993.

[16] J. J. Li, D. Ding, S. H. Lim, and Y.-H. Zhang, "Contact optimization for concentrator solar cells," in *Proc. 35th IEEE PVSC*, Hawaii, pp. 2074–2078, Jun. 2010.

IV EXTERNAL QUANTUM EFFICIENCY MEASUREMENTS OF MULTI-JUNCTION SOLAR CELLS

4.1 Introduction

The spectral external quantum efficiency (EQE) is an indispensible tool for the design and development of multi-junction solar cells [1]–[10]. By partitioning the solar spectrum into narrow absorption bands, multijunction solar cells utilize the photon energies more effectively. The EQE of multijunction solar cells is a measure of the photocurrent generated by each subcell under a certain solar spectrum. It is useful in making current-matched subcells, and can also be used in diagnosing problems such as poor material absorption and carrier diffusion, high surface and interface recombination rates and light absorption in undesired parts such as the tunnel junctions.

However, the EQE measurement of multi-junction solar cells is not an easy task, especially for solar cells with more junctions and more spectral interference between the junctions. EQE measurement artifacts are often observed, characterized by the erroneous responses outside the wavelength range of the subcell under test and the correspondingly lower responses in the wavelength range of the subcell under test [12]–[18]. Fig. 4.1 shows the EQE spectra of the Ge subcells of a commercial InGaP/InGaAs/Ge triple junction solar cell (S1) under varied DC bias voltage (a) and another commercial InGaP/InGaAs/Ge triple junction solar cell (S2) under varied DC bias light intensity on the InGaAs subcell when the solar cell is biased at the optimal bias voltage 0 V (b) and at -0.5 V (c).

The EQE measurement artifacts observed primarily in the InGaAs and Ge wavelength ranges can be attributed to the shunt effect, the luminescence coupling effect, and the combined effects of shunt and luminescence coupling, respectively.

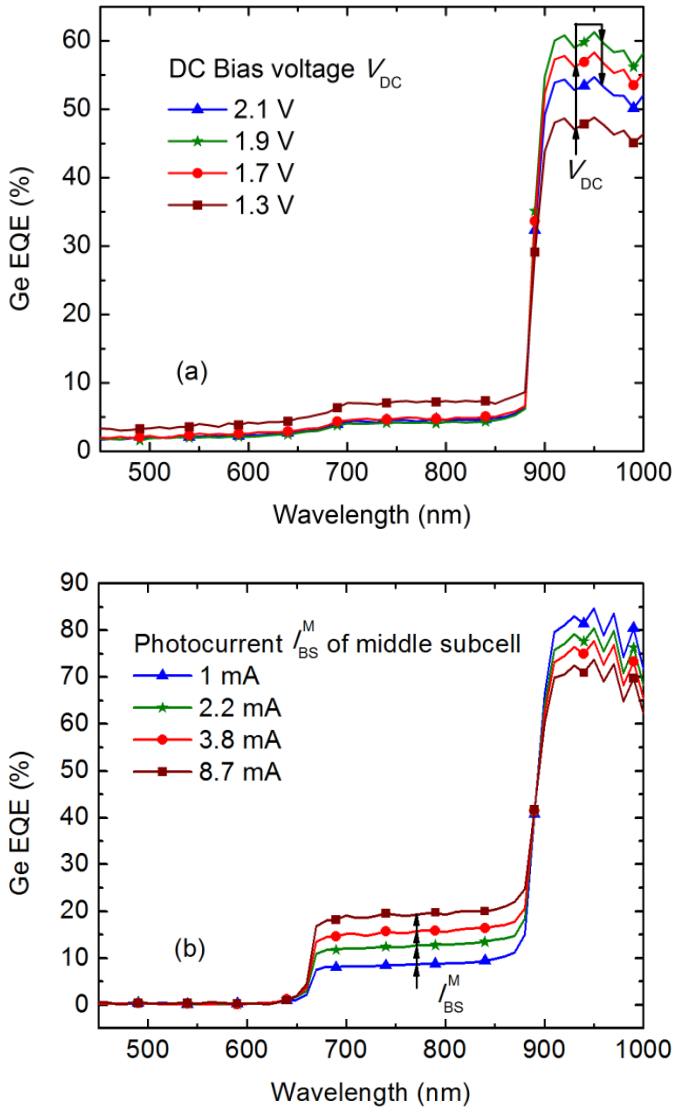

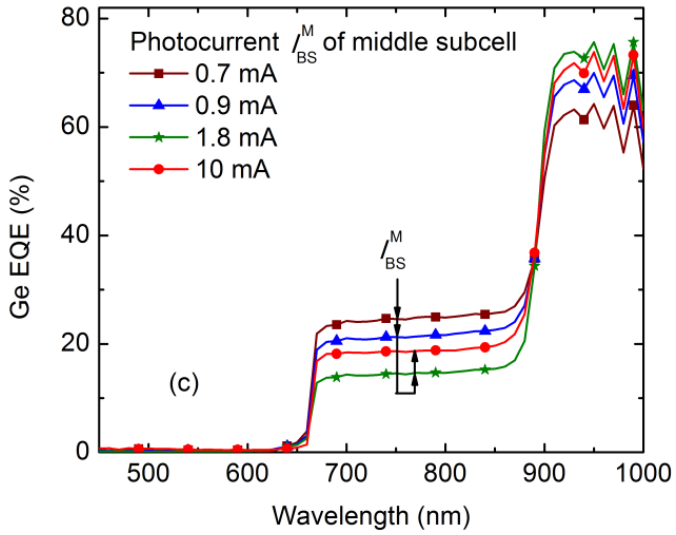

Fig. 4.1. EQE spectra with measurement artifacts caused by the shunt effect (a), the luminescence coupling effect (b), and the combined effects of shunt and luminescence coupling (c).

4.2 Measurement Setup

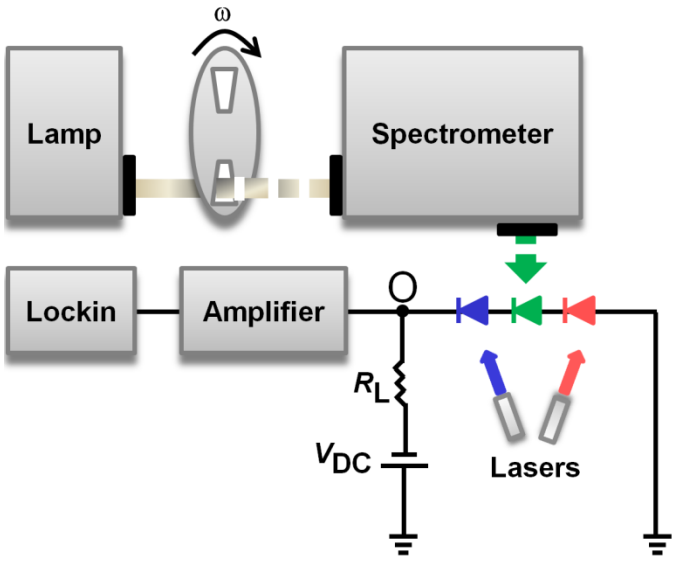

Fig. 4.2. EQE measurement setup for multi-junction solar cells.

Fig. 4.2 shows the schematic diagram of the EQE measurement setup (Newport QE/IPCE). It consists of a Xe arc lamp as a sun simulator, a chopper, a grating monochromator, a lock-in amplifier, and a calibrated Si detector to measure the spectrum of the sun simulator. The white light from the sun simulator is modulated by the chopper at 33 Hz and collected by the monochromator to generate the probing monochromatic light used in the EQE measurements. A 405 nm, 780 nm and 980 nm laser diode are used to light bias the InGaP, InGaAs and Ge subcells, respectively. Laser diodes are used instead of LEDs because their smaller line widths minimize the spectral interferences between the adjacent subcells. A source meter (Keithley 2420) is used in conjunction with a load resistor to provide the DC voltage bias and measure the DC output current of the solar cells. The AC component of the output current generated by the chopped monochromatic light is converted to a voltage signal by a load resistor, amplified by a voltage amplifier (ITHACO 1201), and then measured by the lock-in amplifier.

4.3 DC Measurement Condition

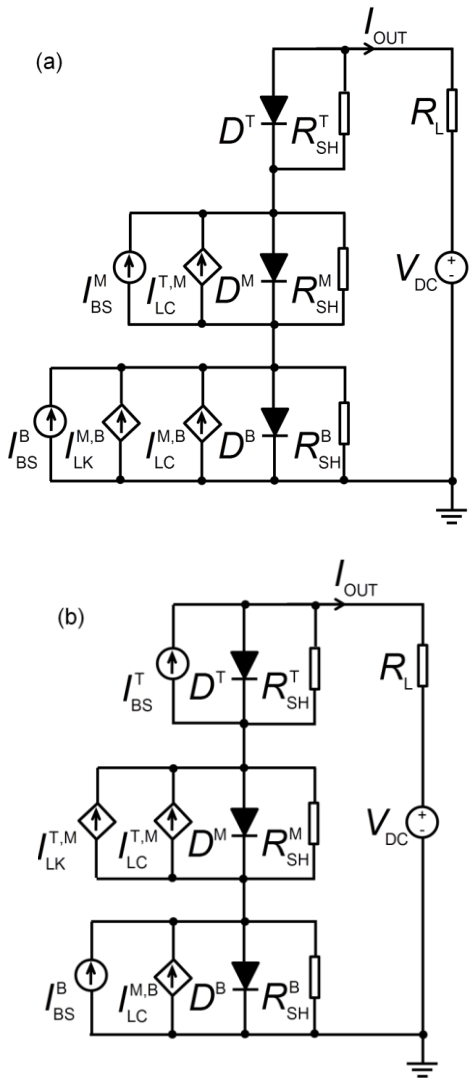

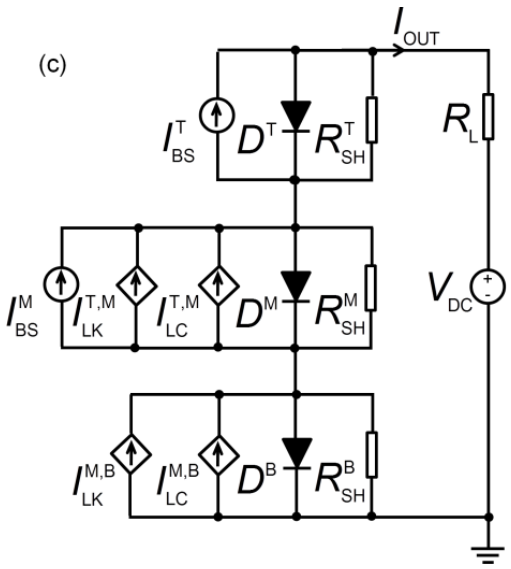

Fig. 4.3. Circuit models of triple junction solar cells under the DC bias condition in the EQE measurement of the top subcell (a), middle subcell (b) and bottom subcell (c). Superscripts T, M, B: top, middle and bottom subcells. Subscript BS: bias light; L: load; SH: shunt; A: applied; LK: light leakage through the upper subcell; D: Diode; LC: luminescence coupling.

Fig. 2 (a), (b) and (c) show the circuit models of triple junction solar cells under the DC light and voltage bias condition in the EQE measurement of the top, middle, and bottom subcell, respectively [15], [17], [18]. The current sources $I_{\mathrm{BS}}^{\mathrm{T}}$, $I_{\mathrm{BS}}^{\mathrm{M}}$ and $I_{\mathrm{BS}}^{\mathrm{B}}$ are the photocurrents generated by the intentional light biases on the three subcells. Because the bias light on an upper subcell may not be completely absorbed, additional photocurrent can be generated in the lower subcell by the unabsorbed bias light. This leakage current is modeled as the current controlled current source $I_{\mathrm{LK}}^{\mathrm{T,M}} = \alpha_{\mathrm{LK}}^{\mathrm{T,M}} I_{\mathrm{BS}}^{\mathrm{T}}$ from the top to the middle subcell and $I_{\mathrm{LK}}^{\mathrm{M,B}} =$

$\alpha_{\mathrm{LK}}^{\mathrm{M,B}} I_{\mathrm{BS}}^{\mathrm{M}}$ from the middle to the bottom subcell, respectively. The leakage strengths $\alpha_{\mathrm{LK}}^{\mathrm{T,M}}$ and $\alpha_{\mathrm{LK}}^{\mathrm{M,B}}$ depending on the absorbance of a subcell and the refractive indices of the subcell and the adjacent subcells are constants at a certain wavelength. Moreover, the radiative recombination in an upper subcell with a larger bandgap generates photons that can be reabsorbed in the lower subcell. This luminescence coupling effect, as will be discussed in more detail in section 4.6.1, is modeled by the current controlled current source $I_{\mathrm{LC}}^{\mathrm{T,M}} = f_{\mathrm{LC}}^{\mathrm{T,M}}(I(\mathrm{D^T}))$ from the top to the middle subcell and $I_{\mathrm{LC}}^{\mathrm{M,B}} = f_{\mathrm{LC}}^{\mathrm{M,B}}(I(\mathrm{D^M}))$ from the middle to the bottom subcell, respectively. Note that the light leakage and luminescence coupling effect have more prominent effect on the DC and AC performance of the solar cells respectively, and are only considered for adjacent subcells in the models. The voltage source V_{DC} is used with the load resistor R_{L}=51 to provide the DC voltage bias to the solar cells. V_{DC} is distributed to the series connected subcells and the load resistor R_{L} as follows

$$V^{\mathrm{T}} + V^{\mathrm{M}} + V^{\mathrm{B}} = V_{\mathrm{DC}} + V_{R_{\mathrm{L}}}. \tag{4.1}$$

The operating points of the subcells in EQE measurements are determined by the DC bias conditions and the coupling effects between the subcells. The *I-V* relations of the three subcells under the DC bias condition are

$$I_{\mathrm{O}} = I_{\mathrm{SC}}^{\mathrm{T}} - \left(I_0^{\mathrm{T}} e^{\frac{qV^{\mathrm{T}}}{n^{\mathrm{T}}kT}} + \frac{V^{\mathrm{T}}}{R_{\mathrm{SH}}^{\mathrm{T}}} \right), \tag{4.2}$$

$$I_{\mathrm{O}} = I_{\mathrm{SC}}^{\mathrm{M}} - \left(I_0^{\mathrm{M}} e^{\frac{qV^{\mathrm{M}}}{n^{\mathrm{M}}kT}} + \frac{V^{\mathrm{M}}}{R_{\mathrm{SH}}^{\mathrm{M}}} \right), \tag{4.3}$$

$$I_{\mathrm{O}} = I_{\mathrm{SC}}^{\mathrm{B}} - \left(I_0^{\mathrm{B}} e^{\frac{qV^{\mathrm{B}}}{n^{\mathrm{B}}kT}} + \frac{V^{\mathrm{B}}}{R_{\mathrm{SH}}^{\mathrm{B}}} \right). \tag{4.4}$$

where I_0^{T}, I_0^{M} and I_0^{B} are the saturation currents and n^{T}, n^{M} and n^{B} are the ideality factors of the three subcells respectively. In the EQE measurements of the top subcell, the middle and bottom subcells are intentionally light biased, as shown in Fig. 4.3 (a), and therefore the short-circuit currents of the three subcells are

$$\begin{aligned} I_{\mathrm{SC}}^{\mathrm{T}} &= 0, \\ I_{\mathrm{SC}}^{\mathrm{M}} &= I_{\mathrm{BS}}^{\mathrm{M}}, \\ I_{\mathrm{SC}}^{\mathrm{B}} &= I_{\mathrm{BS}}^{\mathrm{B}} + I_{\mathrm{LK}}^{\mathrm{M,B}} + I_{\mathrm{LC}}^{\mathrm{M,B}}. \end{aligned} \tag{4.5}$$

In the EQE measurements of the middle subcell, the top and bottom subcells are intentionally light biased, while the middle subcell is unintentionally light biased by the light leakage and luminescence coupling from the top subcell, as shown in Fig. 4.3 (b). The short-circuit currents of the three subcells are therefore

$$\begin{aligned} I_{\mathrm{SC}}^{\mathrm{T}} &= I_{\mathrm{BS}}^{\mathrm{T}}, \\ I_{\mathrm{SC}}^{\mathrm{M}} &= I_{\mathrm{LK}}^{\mathrm{T,M}} + I_{\mathrm{LC}}^{\mathrm{T,M}}, \\ I_{\mathrm{SC}}^{\mathrm{B}} &= I_{\mathrm{BS}}^{\mathrm{B}} + I_{\mathrm{LC}}^{\mathrm{M,B}}. \end{aligned} \tag{4.6}$$

In the EQE measurements of the bottom subcell, the top two subcells are intentionally light biased, while the bottom subcell is unintentionally light biased by the light leakage and luminescence coupling from the middle subcell, as shown in Fig. 4.3 (b). The short-circuit currents of the three subcells are therefore

$$I_{\mathrm{SC}}^{\mathrm{T}} = I_{\mathrm{BS}}^{\mathrm{T}}, \tag{4.7}$$

$$I_{\mathrm{SC}}^{\mathrm{M}} = I_{\mathrm{BS}}^{\mathrm{M}} + I_{\mathrm{LK}}^{\mathrm{T,M}} + I_{\mathrm{LC}}^{\mathrm{T,M}},$$

$$I_{\mathrm{SC}}^{\mathrm{B}} = I_{\mathrm{LK}}^{\mathrm{M,B}} + I_{\mathrm{LC}}^{\mathrm{M,B}}.$$

4.4 Small Signal Analysis

Under the DC bias condition, the EQE spectrum of a subcell is measured by scanning the wavelength of the chopped monochromatic light. Because the photocurrent i_{ph} generated under the chopped monochromatic light can be considered as a small signal perturbation around the DC operating points, the small signal analysis can be used for the AC responses of solar cells in the EQE measurements. In this chapter and the following chapter, the DC signals are denoted as uppercase letters with uppercase subscripts and superscripts, AC signals are denoted as lowercase letters with lowercase subscripts and superscripts, and the signals consisting of both DC and AC components are in uppercase letters with lowercase subscripts and superscripts.

Under the small signal perturbation, the *I-V* relation of a subcell diode becomes

$$I(\mathrm{D})\big|_{V_0} + i(\mathrm{D}) = I_0 e^{\frac{q(V_0+v)}{nkT}} \tag{4.8}$$

If $v \ll V_0$, the right hand side of Eq. (4.8) can be expanded using its Taylor series, and the first two terms are taken as an approximation as

$$I(D)\big|_{V_0} + i(D) \approx I(D)\big|_{V_0} + r\big|_{V_0} v \tag{4.9}$$

where

$$r = \left.\frac{dV}{dI(D)}\right|_{V_0} = \left.\frac{nkT}{I(D)}\right|_{V_0} \tag{4.10}$$

is the small signal resistance of the diode at the operating point $\left(I(D)|_{V_0}, V_0\right)$. Similarly, the *I-V* relation of a shunt resistance that varies with the subcell voltage can be linearized as

$$I(R_{\mathrm{SH}})|_{V_0} + i\left(R_{\mathrm{SH}}\right) = f_{R_{\mathrm{SH}}}\left(V_0 + v\right) \approx I(R_{\mathrm{SH}})|_{V_0} + \frac{v}{r_{\mathrm{sh}}} \tag{4.11}$$

where

$$r_{\mathrm{sh}} = \left.\frac{dV}{dI(R_{\mathrm{SH}})}\right|_{V_0} \tag{4.12}$$

is the small signal shunt resistance at the operating point $\left(I(D)|_{V_0}, V_0\right)$. In addition, the luminescence coupling current in a subcell as a function of the recombination current in the upper subcell can be linearized as

$$I_{\mathrm{LC}}|_{V_0} + i_{\mathrm{lc}} = f_{\mathrm{LC}}\left(I(D)|_{V_0} + i(D)\right) \approx I_{\mathrm{LC}}|_{V_0} + \alpha_{\mathrm{lc}} i(D), \tag{4.13}$$

where

$$\alpha_{\mathrm{lc}} = \left.\frac{dI_{\mathrm{LC}}}{dI(D)}\right|_{V_0}, \tag{4.14}$$

is the small signal luminescence coupling strength at the operating point $\left(I(D)|_{V_0}, V_0\right)$.

For EQE measurements in the wavelength range of the top subcell, the *I-V* relations of the three subcells under the chopped monochromatic light are

$$I_{\mathrm{O}}+i_{\mathrm{o}}=I_{\mathrm{SC}}^{\mathrm{T}}+i_{\mathrm{ph}}^{\mathrm{t}}-\left[I_{0}^{\mathrm{T}}e^{\frac{q\left(V^{\mathrm{T}}+v^{\mathrm{t}}\right)}{n^{\mathrm{T}}kT}}+f_{R_{\mathrm{SH}}}^{\mathrm{T}}\left(V^{\mathrm{T}}+v^{\mathrm{t}}\right)\right],$$

$$I_{\mathrm{O}}+i_{\mathrm{o}}=I_{\mathrm{SC}}^{\mathrm{M}}+i_{\mathrm{lk}}^{\mathrm{t,m}}+i_{\mathrm{lc}}^{\mathrm{t,m}}-\left[I_{0}^{\mathrm{M}}e^{\frac{q\left(V^{\mathrm{M}}+v^{\mathrm{m}}\right)}{n^{\mathrm{M}}kT}}+f_{R_{\mathrm{SH}}}^{\mathrm{M}}\left(V^{\mathrm{M}}+v^{\mathrm{m}}\right)\right], \tag{4.15}$$

$$I_{\mathrm{O}}+i_{\mathrm{o}}=I_{\mathrm{SC}}^{\mathrm{B}}+i_{\mathrm{lc}}^{\mathrm{m,b}}-\left[I_{0}^{\mathrm{B}}e^{\frac{q\left(V^{\mathrm{B}}+v^{\mathrm{b}}\right)}{n^{\mathrm{B}}kT}}+f_{R_{\mathrm{SH}}}^{\mathrm{B}}\left(V^{\mathrm{B}}+v^{\mathrm{b}}\right)\right].$$

With the small signal approximation and the DC operating condition, the small signal *I-V* relations of the three subcells can be obtained from Eq. set (4.15) as

$$i_{\mathrm{o}}=i_{\mathrm{ph}}^{\mathrm{t}}-\frac{v^{\mathrm{t}}}{r^{\mathrm{t}}//r_{\mathrm{sh}}^{\mathrm{t}}},$$

$$i_{\mathrm{o}}=i_{\mathrm{lk}}^{\mathrm{t,m}}+i_{\mathrm{lc}}^{\mathrm{t,m}}-\frac{v^{\mathrm{m}}}{r^{\mathrm{m}}//r_{\mathrm{sh}}^{\mathrm{m}}}, \tag{4.16}$$

$$i_{\mathrm{o}}=i_{\mathrm{lc}}^{\mathrm{m,b}}-\frac{v^{\mathrm{b}}}{r^{\mathrm{b}}//r_{\mathrm{sh}}^{\mathrm{b}}}.$$

For EQE measurements in the wavelength range of the middle subcell, the *I-V* relations of the three subcells under the chopped monochromatic light are,

$$I_{\mathrm{O}}+i_{\mathrm{o}}=I_{\mathrm{SC}}^{\mathrm{T}}-\left[I_{0}^{\mathrm{T}}e^{\frac{q\left(V^{\mathrm{T}}+v^{\mathrm{t}}\right)}{n^{\mathrm{T}}kT}}+f_{R_{\mathrm{SH}}}^{\mathrm{T}}\left(V^{\mathrm{T}}+v^{\mathrm{t}}\right)\right],$$

$$I_{\mathrm{O}}+i_{\mathrm{o}}=I_{\mathrm{SC}}^{\mathrm{M}}+i_{\mathrm{ph}}^{\mathrm{m}}+i_{\mathrm{lc}}^{\mathrm{t,m}}-\left[I_{0}^{\mathrm{M}}e^{\frac{q\left(V^{\mathrm{M}}+v^{\mathrm{m}}\right)}{n^{\mathrm{M}}kT}}+f_{R_{\mathrm{SH}}}^{\mathrm{M}}\left(V^{\mathrm{M}}+v^{\mathrm{m}}\right)\right], \tag{4.17}$$

$$I_{\mathrm{O}}+i_{\mathrm{o}}=I_{\mathrm{SC}}^{\mathrm{B}}+i_{\mathrm{lk}}^{\mathrm{m,b}}+i_{\mathrm{lc}}^{\mathrm{m,b}}-\left[I_{0}^{\mathrm{B}}e^{\frac{q\left(V^{\mathrm{B}}+v^{\mathrm{b}}\right)}{n^{\mathrm{B}}kT}}+f_{R_{\mathrm{SH}}}^{\mathrm{B}}\left(V^{\mathrm{B}}+v^{\mathrm{b}}\right)\right].$$

With the small signal approximation and the DC operating condition, the small signal *I-V* relations of the three subcells can be obtained from Eq. set (4.17) as

$$\begin{aligned} i_{\mathrm{o}} &= -\frac{v^{\mathrm{t}}}{r^{\mathrm{t}} // r_{\mathrm{sh}}^{\mathrm{t}}}, \\ i_{\mathrm{o}} &= i_{\mathrm{ph}}^{\mathrm{m}} + i_{\mathrm{lc}}^{\mathrm{t,m}} - \frac{v^{\mathrm{m}}}{r^{\mathrm{m}} // r_{\mathrm{sh}}^{\mathrm{m}}}, \\ i_{\mathrm{o}} &= i_{\mathrm{lk}}^{\mathrm{m,b}} + i_{\mathrm{lc}}^{\mathrm{m,b}} - \frac{v^{\mathrm{b}}}{r^{\mathrm{b}} // r_{\mathrm{sh}}^{\mathrm{b}}}. \end{aligned} \tag{4.18}$$

For EQE measurements in the wavelength range of the bottom subcell, the *I-V* relations of the three subcells under the chopped monochromatic light are

$$\begin{aligned} I_{\mathrm{O}} + i_{\mathrm{o}} &= I_{\mathrm{SC}}^{\mathrm{T}} - \left[I_0^{\mathrm{T}} e^{\frac{q\left(V^{\mathrm{T}} + v^{\mathrm{t}}\right)}{n^{\mathrm{T}} kT}} + f_{R_{\mathrm{SH}}}^{\mathrm{T}} \left(V^{\mathrm{T}} + v^{\mathrm{t}}\right) \right], \\ I_{\mathrm{O}} + i_{\mathrm{o}} &= I_{\mathrm{SC}}^{\mathrm{M}} + i_{\mathrm{lc}}^{\mathrm{t,m}} - \left[I_0^{\mathrm{M}} e^{\frac{q\left(V^{\mathrm{M}} + v^{\mathrm{m}}\right)}{n^{\mathrm{M}} kT}} + f_{R_{\mathrm{SH}}}^{\mathrm{M}} \left(V^{\mathrm{M}} + v^{\mathrm{m}}\right) \right], \\ I_{\mathrm{O}} + i_{\mathrm{o}} &= I_{\mathrm{SC}}^{\mathrm{B}} + i_{\mathrm{ph}}^{\mathrm{b}} + i_{\mathrm{lc}}^{\mathrm{m,b}} - \left[I_0^{\mathrm{B}} e^{\frac{q\left(V^{\mathrm{B}} + v^{\mathrm{b}}\right)}{n^{\mathrm{B}} kT}} + f_{R_{\mathrm{SH}}}^{\mathrm{B}} \left(V^{\mathrm{B}} + v^{\mathrm{b}}\right) \right]. \end{aligned} \tag{4.19}$$

With the small signal approximation and the DC operating condition, the small signal *I-V* relations of the three subcells can be obtained from Eq. set (4.19) as

$$\begin{aligned} i_{\mathrm{o}} &= -\frac{v^{\mathrm{t}}}{r^{\mathrm{t}} // r_{\mathrm{sh}}^{\mathrm{t}}}, \\ i_{\mathrm{o}} &= i_{\mathrm{lc}}^{\mathrm{t,m}} - \frac{v^{\mathrm{m}}}{r^{\mathrm{m}} // r_{\mathrm{sh}}^{\mathrm{m}}}, \end{aligned} \tag{4.20}$$

$$i_{\mathrm{o}} = i_{\mathrm{ph}}^{\mathrm{b}} + i_{\mathrm{lc}}^{\mathrm{m,b}} - \frac{v^{\mathrm{b}}}{r^{\mathrm{b}} // r_{\mathrm{sh}}^{\mathrm{b}}} .$$

In addition, the voltage drops of the three subcells generated by the chopped monochromatic light obey

$$v^{\mathrm{t}} + v^{\mathrm{m}} + v^{\mathrm{b}} = i_{\mathrm{o}} R_{\mathrm{L}} . \tag{4.21}$$

Eq. set (4.16) and Eq. (4.21), Eq. set (4.18) and Eq. (4.21) and Eq. set (4.20) and Eq. (4.21) represent the small signal equivalent circuits of the EQE measurements in the wavelength range of the top subcell, the middle subcell and the bottom subcell, as shown in Fig. 4.4 (a), (b) and (c) respectively [15], [17], [18].

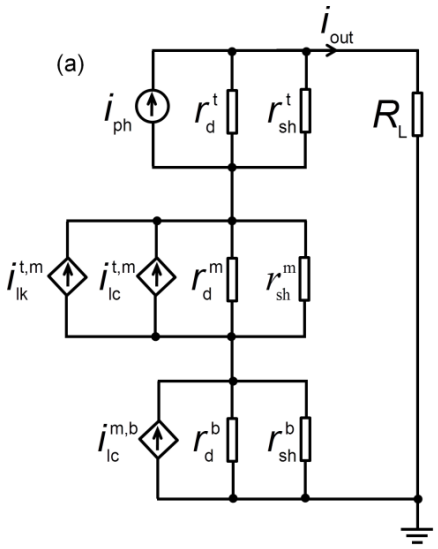

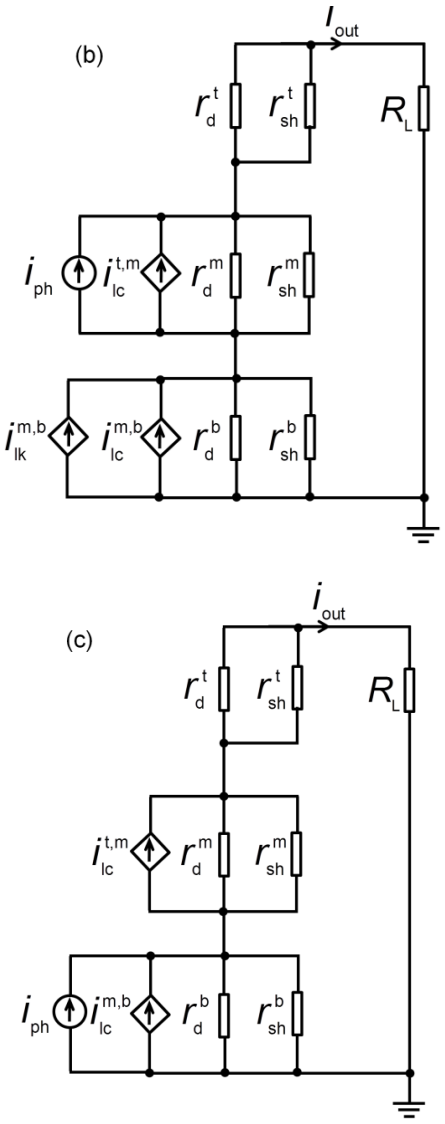

Fig. 4.4. Small signal models of triple junction solar cells in EQE measurements in the wavelength range of the top subcell (a), middle subcell (b) and bottom subcell (c). Small letters stand for the small signal counterparts of the DC elements shown in Fig. 4.3. Subscript ph: AC photocurrent; d: diode.

The output current i_o and the voltage drops of the subcells generated by the chopped monochromatic light are calculated as

$$i_{\mathrm{o}}=i_{\mathrm{ph}}^{\mathrm{t}}\frac{\left(r^{\mathrm{t}}//r_{\mathrm{sh}}^{\mathrm{t}}\right)+\left(\gamma^{\mathrm{t,m}}+\alpha_{\mathrm{lk}}^{\mathrm{t,m}}\right)\left(r^{\mathrm{m}}//r_{\mathrm{sh}}^{\mathrm{m}}\right)+\left(\gamma^{\mathrm{t,m}}+\alpha_{\mathrm{lk}}^{\mathrm{t,m}}\right)\gamma^{\mathrm{m,b}}\left(r^{\mathrm{b}}//r_{\mathrm{sh}}^{\mathrm{b}}\right)}{\left(r^{\mathrm{t}}//r_{\mathrm{sh}}^{\mathrm{t}}\right)+\left(1+\gamma^{\mathrm{t,m}}\right)\left(r^{\mathrm{m}}//r_{\mathrm{sh}}^{\mathrm{m}}\right)+\left[1+\left(1+\gamma^{\mathrm{t,m}}\right)\gamma^{\mathrm{m,b}}\right]\left(r^{\mathrm{b}}//r_{\mathrm{sh}}^{\mathrm{b}}\right)+R_{\mathrm{L}}},\qquad(4.22a)$$

$$v^{\mathrm{t}}=\left(i_{\mathrm{ph}}^{\mathrm{t}}-i_{\mathrm{o}}\right)\left(r^{\mathrm{t}}//r_{\mathrm{sh}}^{\mathrm{t}}\right),\qquad(4.22b)$$

$$v^{\mathrm{m}}=\left[\left(\alpha_{\mathrm{lk}}^{\mathrm{t,m}}+\gamma^{\mathrm{t,m}}\right)i_{\mathrm{ph}}^{\mathrm{t}}-\gamma^{\mathrm{t,m}}i_{\mathrm{o}}\right]\left(r^{\mathrm{m}}//r_{\mathrm{sh}}^{\mathrm{m}}\right),\qquad(4.22c)$$

$$v^{\mathrm{b}}=\left\{\left(\gamma^{\mathrm{t,m}}+\alpha_{\mathrm{lk}}^{\mathrm{t,m}}\right)\gamma^{\mathrm{m,b}}i_{\mathrm{ph}}^{\mathrm{t}}-\left[1+\left(1+\gamma^{\mathrm{t,m}}\right)\gamma^{\mathrm{m,b}}\right]i_{\mathrm{o}}\right\}\left(r^{\mathrm{b}}//r_{\mathrm{sh}}^{\mathrm{b}}\right),\qquad(4.22d)$$

in the wavelength range of the top subcell, and

$$i_{\mathrm{o}}=i_{\mathrm{ph}}^{\mathrm{m}}\frac{\left(r^{\mathrm{m}}//r_{\mathrm{sh}}^{\mathrm{m}}\right)+\left(\gamma^{\mathrm{m,b}}+\alpha_{\mathrm{lk}}^{\mathrm{m,b}}\right)\left(r^{\mathrm{b}}//r_{\mathrm{sh}}^{\mathrm{b}}\right)}{\left(r^{\mathrm{t}}//r_{\mathrm{sh}}^{\mathrm{t}}\right)+\left(1+\gamma^{\mathrm{t,m}}\right)\left(r^{\mathrm{m}}//r_{\mathrm{sh}}^{\mathrm{m}}\right)+\left[1+\left(1+\gamma^{\mathrm{t,m}}\right)\gamma^{\mathrm{m,b}}\right]\left(r^{\mathrm{b}}//r_{\mathrm{sh}}^{\mathrm{b}}\right)+R_{\mathrm{L}}},\qquad(4.23a)$$

$$v^{\mathrm{t}}=-i_{\mathrm{o}}\left(r^{\mathrm{t}}//r_{\mathrm{sh}}^{\mathrm{t}}\right),\qquad(4.23b)$$

$$v^{\mathrm{m}}=\left[i_{\mathrm{ph}}^{\mathrm{m}}-\gamma^{\mathrm{t,m}}i_{\mathrm{o}}\right]\left(r^{\mathrm{m}}//r_{\mathrm{sh}}^{\mathrm{m}}\right),\qquad(4.23c)$$

$$v^{\mathrm{b}}=\left\{\left(\gamma^{\mathrm{m,b}}+\alpha_{\mathrm{lk}}^{\mathrm{m,b}}\right)i_{\mathrm{ph}}^{\mathrm{m}}-\left[1+\left(1+\gamma^{\mathrm{t,m}}\right)\gamma^{\mathrm{m,b}}\right]i_{\mathrm{o}}\right\}\left(r^{\mathrm{b}}//r_{\mathrm{sh}}^{\mathrm{b}}\right),\qquad(4.23d)$$

in the wavelength range of the middle subcell, and

$$i_{\mathrm{o}}=i_{\mathrm{ph}}^{\mathrm{b}}\frac{\left(r^{\mathrm{b}}//r_{\mathrm{sh}}^{\mathrm{b}}\right)}{\left(r^{\mathrm{t}}//r_{\mathrm{sh}}^{\mathrm{t}}\right)+\left(1+\gamma^{\mathrm{t,m}}\right)\left(r^{\mathrm{m}}//r_{\mathrm{sh}}^{\mathrm{m}}\right)+\left[1+\left(1+\gamma^{\mathrm{t,m}}\right)\gamma^{\mathrm{m,b}}\right]\left(r^{\mathrm{b}}//r_{\mathrm{sh}}^{\mathrm{b}}\right)+R_{\mathrm{L}}},\qquad(4.24a)$$

$$v^{\mathrm{t}}=-i_{\mathrm{o}}\left(r^{\mathrm{t}}//r_{\mathrm{sh}}^{\mathrm{t}}\right),\qquad(4.24b)$$

$$v^{\mathrm{m}}=-i_{\mathrm{o}}\left(1+\gamma^{\mathrm{t,m}}\right)\left(r^{\mathrm{m}}//r_{\mathrm{sh}}^{\mathrm{m}}\right),\qquad(4.24c)$$

$$v^{\mathrm{b}}=\left\{i_{\mathrm{ph}}^{\mathrm{b}}-\left[1+\left(1+\gamma^{\mathrm{t,m}}\right)\gamma^{\mathrm{m,b}}\right]i_{\mathrm{o}}\right\}\left(r^{\mathrm{b}}//r_{\mathrm{sh}}^{\mathrm{b}}\right),\qquad(4.24d)$$

in the wavelength range of the bottom subcell. In Eq. sets (4.22)-(4.24), $\gamma^{\mathrm{t,m}}=\alpha_{\mathrm{lc}}^{\mathrm{t,m}}\frac{r_{\mathrm{sh}}^{\mathrm{t}}}{r^{\mathrm{t}}+r_{\mathrm{sh}}^{\mathrm{t}}}$,$\gamma^{\mathrm{m,b}}=\alpha_{\mathrm{lc}}^{\mathrm{m,b}}\frac{r_{\mathrm{sh}}^{\mathrm{m}}}{r^{\mathrm{m}}+r_{\mathrm{sh}}^{\mathrm{m}}}$, and $r^{\mathrm{t}}//r_{\mathrm{sh}}^{\mathrm{t}}$, $r^{m}//r_{\mathrm{sh}}^{m}$ and $r^{\mathrm{b}}//r_{\mathrm{sh}}^{\mathrm{b}}$ are the parallel

resistances of the small signal diode resistance and shunt resistance of the top, middle and bottom subcell respectively.

The above equations link the output current i_o to the subcell characteristics at the DC operating points. It can be seen from Eq. (4.22a), (4.23a) and (4.24a) that the measured output current i_o is not always the same as the photocurrent generated under the chopped monochromatic light, because of the shunt and luminescence coupling effects. Furthermore, the DC voltage and light biases can be used to control and minimize the EQE measurement artifacts. When the bias light intensity on a subcell is varied, it primarily changes the operating point of the subcell, and therefore controls its radiative recombination rate and the luminescence coupling to the lower subcell. When the bias voltage is varied, it primarily changes the operating point of the subcell under test and therefore controls the shunt effect.

4.5 Special Cases

In reality, not every solar cell has all the characteristics of shunts and luminescence coupling. For high quality solar cells with strong luminescence coupling effects and large shunt resistances, Eq. (4.22a), (4.23a) and (4.24a) in the wavelength range of the three subcells are simplified to

$$\begin{aligned} i_o &= i_{ph}^t, \\ i_o &= 0, \\ i_o &= 0, \end{aligned} \tag{4.25}$$

for the EQE measurements of the top subcell, which shows the EQE is not affected by the luminescence coupling effect. For the EQE measurements of the middle subcells, Eq. (4.22a), (4.23a) and (4.24a) in the wavelength range of the three subcells are simplified to

$$\begin{aligned} i_{\mathrm{o}} &= i_{\mathrm{ph}}^{\mathrm{t}} \frac{\alpha_{\mathrm{lc}}^{\mathrm{t,m}} + \alpha_{\mathrm{lk}}^{\mathrm{t,m}}}{1+\alpha_{\mathrm{lc}}^{\mathrm{t,m}}}, \\ i_{\mathrm{o}} &= i_{\mathrm{ph}}^{\mathrm{m}} \frac{1}{1+\alpha_{\mathrm{lc}}^{\mathrm{t,m}}}, \\ i_{\mathrm{o}} &= 0, \end{aligned} \tag{4.26}$$

which shows that the EQE of the middle subcell is larger than the leakage response in the wavelength range of the top subcell, and it is smaller than the real response in the wavelength range of the middle subcell, because of the luminescence coupling effect between the top and middle subcells. For the EQE measurements of the bottom subcells, Eq. (4.22a), (4.23a) and (4.24a) in the wavelength range of the three subcells are simplified to

$$\begin{aligned} i_{\mathrm{o}} &= i_{\mathrm{ph}}^{\mathrm{t}} \frac{\left(\alpha_{\mathrm{lc}}^{\mathrm{t,m}} + \alpha_{\mathrm{lk}}^{\mathrm{t,m}}\right)\alpha_{\mathrm{lc}}^{\mathrm{m,b}}}{1+\left(1+\alpha_{\mathrm{lc}}^{\mathrm{t,m}}\right)\alpha_{\mathrm{lc}}^{\mathrm{m,b}}}, \\ i_{\mathrm{o}} &= i_{\mathrm{ph}}^{\mathrm{m}} \frac{\alpha_{\mathrm{lc}}^{\mathrm{m,b}} + \alpha_{\mathrm{lk}}^{\mathrm{m,b}}}{1+\left(1+\alpha_{\mathrm{lc}}^{\mathrm{t,m}}\right)\alpha_{\mathrm{lc}}^{\mathrm{m,b}}}, \\ i_{\mathrm{o}} &= i_{\mathrm{ph}}^{\mathrm{b}} \frac{1}{1+\left(1+\alpha_{\mathrm{lc}}^{\mathrm{t,m}}\right)\alpha_{\mathrm{lc}}^{\mathrm{m,b}}}, \end{aligned} \tag{4.27}$$

which show that the EQE of the bottom subcells is larger than the leakage response in the wavelength ranges of the top and middle subcells, and it is smaller

than the real response in the wavelength range of the bottom subcells, because of the luminescence coupling effect between each adjacent subcells.

For poor quality solar cells, there is no luminescence coupling between subcells and the shunt resistances are low. The EQE responses of the three subcells are simplified to

$$
\begin{aligned}
i_{\mathrm{o}} &= i_{\mathrm{ph}}^{\mathrm{t}} \frac{r^{\mathrm{t}} // r_{\mathrm{sh}}^{\mathrm{t}}}{\left(r^{\mathrm{t}} // r_{\mathrm{sh}}^{\mathrm{t}}\right)+\left(r^{\mathrm{m}} // r_{\mathrm{sh}}^{\mathrm{m}}\right)+\left(r^{\mathrm{b}} // r_{\mathrm{sh}}^{\mathrm{b}}\right)+R_{\mathrm{L}}} \\
i_{\mathrm{o}} &= i_{\mathrm{ph}}^{\mathrm{m}} \frac{r^{\mathrm{m}} // r_{\mathrm{sh}}^{\mathrm{m}}}{\left(r^{\mathrm{t}} // r_{\mathrm{sh}}^{\mathrm{t}}\right)+\left(r^{\mathrm{m}} // r_{\mathrm{sh}}^{\mathrm{m}}\right)+\left(r^{\mathrm{b}} // r_{\mathrm{sh}}^{\mathrm{b}}\right)+R_{\mathrm{L}}} \\
i_{\mathrm{o}} &= i_{\mathrm{ph}}^{\mathrm{b}} \frac{r^{\mathrm{b}} // r_{\mathrm{sh}}^{\mathrm{b}}}{\left(r^{\mathrm{t}} // r_{\mathrm{sh}}^{\mathrm{t}}\right)+\left(r^{\mathrm{m}} // r_{\mathrm{sh}}^{\mathrm{m}}\right)+\left(r^{\mathrm{b}} // r_{\mathrm{sh}}^{\mathrm{b}}\right)+R_{\mathrm{L}}}
\end{aligned}
\tag{4.28}
$$

For some special structures such as the bi-facial triple junction solar cells [18], the upper two subcells are grown on the different side of the wafers from the bottom cell, and therefore there is no luminescence coupling from the middle subcell to the bottom subcell. The EQE responses are therefore

$$
\begin{aligned}
i_{\mathrm{o}} &= i_{\mathrm{ph}}^{\mathrm{t}} \frac{\left(r^{\mathrm{t}} // r_{\mathrm{sh}}^{\mathrm{t}}\right)+\left(\gamma^{\mathrm{t,m}}+\alpha_{\mathrm{lk}}^{\mathrm{t,m}}\right)\left(r^{\mathrm{m}} // r_{\mathrm{sh}}^{\mathrm{m}}\right)}{\left(r^{\mathrm{t}} // r_{\mathrm{sh}}^{\mathrm{t}}\right)+\left(1+\gamma^{\mathrm{t,m}}\right)\left(r^{\mathrm{m}} // r_{\mathrm{sh}}^{\mathrm{m}}\right)+\left(r^{\mathrm{b}} // r_{\mathrm{sh}}^{\mathrm{b}}\right)+R_{\mathrm{L}}} \\
i_{\mathrm{o}} &= i_{\mathrm{ph}}^{\mathrm{m}} \frac{r^{\mathrm{m}} // r_{\mathrm{sh}}^{\mathrm{m}}}{\left(r^{\mathrm{t}} // r_{\mathrm{sh}}^{\mathrm{t}}\right)+\left(1+\gamma^{\mathrm{t,m}}\right)\left(r^{\mathrm{m}} // r_{\mathrm{sh}}^{\mathrm{m}}\right)+\left(r^{\mathrm{b}} // r_{\mathrm{sh}}^{\mathrm{b}}\right)+R_{\mathrm{L}}} \\
i_{\mathrm{o}} &= i_{\mathrm{ph}}^{\mathrm{b}} \frac{\left(r^{\mathrm{b}} // r_{\mathrm{sh}}^{\mathrm{b}}\right)}{\left(r^{\mathrm{t}} // r_{\mathrm{sh}}^{\mathrm{t}}\right)+\left(1+\gamma^{\mathrm{t,m}}\right)\left(r^{\mathrm{m}} // r_{\mathrm{sh}}^{\mathrm{m}}\right)+\left(r^{\mathrm{b}} // r_{\mathrm{sh}}^{\mathrm{b}}\right)+R_{\mathrm{L}}}
\end{aligned}
\tag{4.29}
$$

4.6 Graphical Illustrations

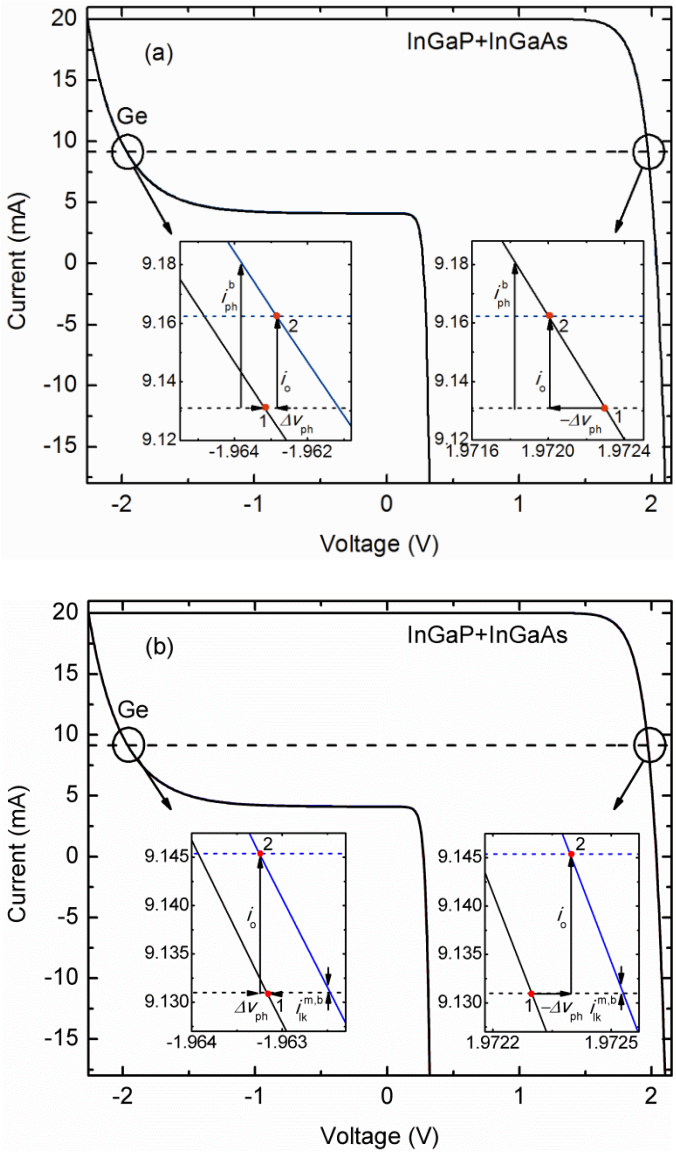

Fig. 4.5. Origin of EQE measurement artifacts in the Ge wavelength range (a) and in the InGaAs wavelength range (b).

The origin of EQE measurement artifacts of the Ge subcells in the Ge wavelength range and in the InGaAs wavelength range is explained in Fig. 4.5 (a)

and (b), respectively. In Fig. 4.5, the *I-V* curves of the Ge subcell and the top two subcells under the DC biases are shown in the dark solid lines, and the DC output current of the triple junction solar cell is shown in the dark dashed line. When the monochromatic light is switched on in the Ge wavelength range or in the InGaAs wavelength range, as shown in Fig. 4.5 (a) and (b) respectively, the *I-V* curve of the Ge subcell or the top two subcells is shifted up to the blue solid line. In addition, in the InGaAs wavelength range in Fig. 4.5 (b), the *I-V* of the Ge subcell is also shifted up, because of the increased light leakage and luminescence coupling. As a result, the output current under the monochromatic light is increased as shown in the blue dashed line. The intersections of the subcell *I-V* curves and the output current lines are the subcell operating points in the measurements.

The EQE measurement artifacts arise when i_o, i.e. the incremental current from the DC bias condition at points 1 to the operating points under the monochromatic light at points 2 as shown in the insets of Figure 4.5 (a) and (b), is different from the photocurrent i_{ph}^{b} generated in the Ge wavelength range or the optical leakage current $i_{lk}^{m,b}$generated in the InGaAs wavelength range. It can be seen that the Ge *I-V* curve is tilted at the operating points because of the low shunt resistance of the Ge subcell. Furthermore, the luminescence coupling effect causes a negative feedback on i_o in the Ge wavelength range and an additional photocurrent in the InGaAs wavelength range. As a result, i_o is smaller than i_{ph}^{b} in the Ge wavelength range, and it is larger than $i_{lk}^{m,b}$ in the InGaAs wavelength

range. Meanwhile, the voltage drops on the Ge subcell Δv_{ph} and on the top two subcells $-\Delta v_{\mathrm{ph}}$ generated under the chopped monochromatic light cancel with each other.

4.7 Characterization

4.7.1 Shunt Effect

The EQE measurement artifacts shown in Fig. 4.1 (a) are caused by the low shunt resistance of the Ge subcell, as the luminescence coupling effect is not observed for the solar cell S1. The shunt effect can be characterized using the small signal resistances obtained from the subcell *I-V* curves. In order to probe the subcell *I-V* curves, the subcells not under test have to be strongly light biased to make the subcell under test current limiting. Furthermore, the voltage of a subcell is difficult to determine due to the series connection of the subcells. A reciprocity relation between the photovoltaic quantum efficiency and the electroluminescence has been used to determine the subcell voltages, although with considerable complexity in implementation [20]. In the current work to determine the smalls signal resistances, the accurate subcell voltages are not required, and therefore the I_{sc}-V_{oc} method [15], [18], [21]–[23] is used to measure the *I-V* curves of the forward biased InGaP and InGaAs subcells, and the *I-V* curve of the Ge subcell that is reverse biased or weakly forward biased is deduced from a voltage sweep, as shown in Fig. 4.6. With the I_{sc}-V_{oc} method, the bias light intensity on the InGaP or InGaAs subcell increases gradually while the other subcells are strongly light biased. The pseudo *I-V* of the subcell formed by the points (I_{sc}, V_{oc}) is equivalent

to the dark *I-V* without the effect of the series resistance [21]–[23]. In practice, the bias light intensity on the subcell under test is usually varied near one sun, because the I_{sc}-V_{oc} method based on the superposition principle is valid when the bias light intensity does not vary too much. In addition, I_{sc} of a subcell with a low shunt resistance is taken at a weakly forward biased voltage where the current is close to the short circuit current and the shunt effect is minimized. The *I-V* curve of the Ge subcell is measured from a voltage sweep when the Ge subcell is current limiting, with the photocurrent due to optical leakage subtracted from the measured current and the voltages of the top two subcells subtracted from the measured voltage. It can be seen that the Ge *I-V* curve shows a soft breakdown at the reverse bias. Note that the subcell voltages are not accurately determined, so they are left in arbitrary units in Fig. 4.6.

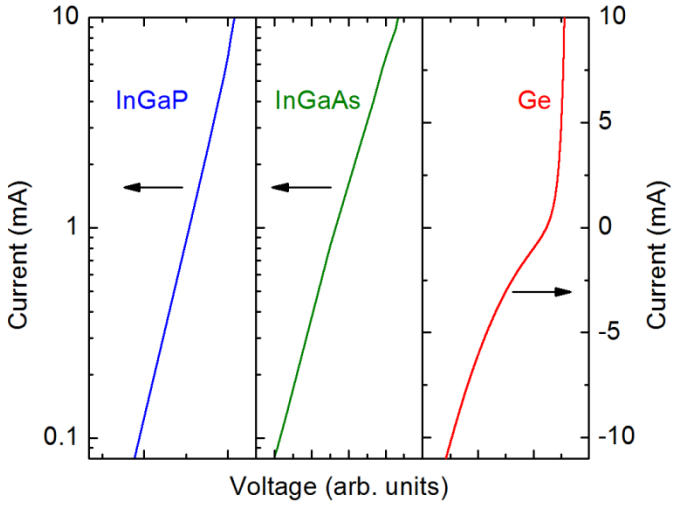

Fig. 4.6. Measured *I-V* curves of the InGaP, InGaAs and Ge subcells of the triple junction solar cell S1.

Fig. 4.7 compares i_o/i_{ph}^b and i_o/i_{ph}^m obtained at 980 nm and 780 nm of the EQE spectra in Fig. 4.1 (a), and those calculated using Eq. set (4.28). i_{ph}^m is taken from the EQE measurement in the InGaAs wavelength range, and i_{ph}^b is obtained using the pulse bias methods in Chapter V. At the optimal bias voltage 1.9 V, the measurement artifacts are minimized and the measured output current i_o reaches the maximum at 980 nm and the minimum at 780 nm. When V_{DC} decreases or increases, i_o decreases at 980 nm and increases at 780 nm, because of the decreases of the small signal shunt resistance and the small signal diode resistance, respectively. Fig. 4.7 shows a good agreement between the measurement and calculation results.

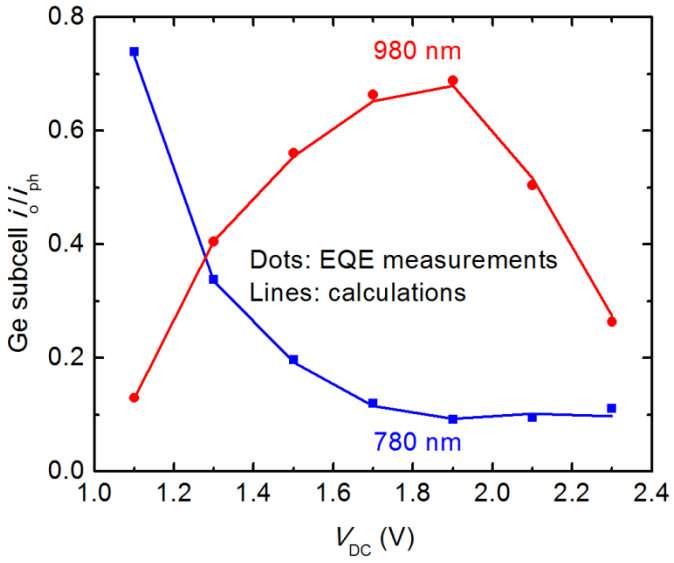

Fig. 4.7. i_o/i_{ph} of the Ge subcell in the Ge and InGaAs wavelength ranges obtained from Fig. 4.1 (a) (dots) and from the calculations (lines) using Eq. set (4.28).

4.7.2 Luminescence Coupling Effect

The measurement artifacts in the EQE spectra of the Ge subcell of the triple junction solar cell S2 at the optimal bias voltage 0 V, as shown in Fig. 4.1 (b), are caused by the luminescence coupling effect because the shunt effect is minimized. The optimal bias voltage usually does not change much with the bias light intensity when the luminescence coupling is dominant. For the solar cell S2, the luminescence coupling effect is only observed between the InGaAs and Ge subcells, and the light leakage between the InGaP and InGaAs subcells can be neglected because there is no EQE response in the InGaP wavelength range in Fig. 4.1 (b). Therefore, Eq. set (4.27) is further simplified to

$$\begin{aligned} i_o &= 0, \\ i_o &= i_{ph}^{m} \frac{\alpha_{lc}^{m,b} + \alpha_{lk}^{m,b}}{1+\alpha_{lc}^{m,b}}, \\ i_o &= i_{ph}^{b} \frac{1}{1+\alpha_{lc}^{m,b}}. \end{aligned} \tag{4.30}$$

The luminescence coupling strength and the leakage strength in Eq. set (4.30) can be characterized by probing the luminescence of the subcells [17],[18], [24]. The radiative recombination in a subcell generates photons with the energy at the bandgap of the subcell. After going through photon recycling inside the subcell, a few percent of the photons within the narrow escape cone at the semiconductor/air interface escape from the solar cell surface generating luminescence (*L*), while most of them are transimitted to the following subcell with a smaller bandgap and contribute to its photocurrent. The relationship between the number of photons emitted into the free space and the number being

reabsorbed, as shown in Eq. (4.31), is characteristic of the solar cell at a given set of voltage and light biases,

$$\int \frac{L(\lambda)\lambda}{hc} d\lambda = \frac{\chi}{q} I_{\mathrm{LC}} \tag{4.31}$$

where the parameter χ depends on the geometries and refractive indices of the two subcells and the internal quantum efficiency of the lower subcell. In luminescence measurements, χ is further scaled according to the solid angle and responsivity of the detector. The small signal luminescence coupling strength is therefore

$$\alpha_{\mathrm{lc}} = \frac{dI_{\mathrm{LC}}}{dI(\mathrm{D})} = \frac{d\left(q\int \frac{L(\lambda)\lambda}{hc} d\lambda \Big/ \chi \right)}{dI(\mathrm{D})}. \tag{4.32}$$

The luminescence intensity L in Eq. (4.32) is measured using a fiber-coupled radiometer (EPP2000), while the bias light intensity on the InGaAs subcell is varied. The recombination current I(D) in Eq. (4.32) is determined as the photocurrent of the InGaAs subcell subtracted by the output current of the triple junction.

Fig. 4.8 compares $i_{\mathrm{o}}/i_{\mathrm{ph}}^{\mathrm{b}}$ and $i_{\mathrm{o}}/i_{\mathrm{ph}}^{\mathrm{m}}$ obtained at 980 nm and 780 nm of the EQE spectra in Fig. 4.1 (b), and those calculated using Eq. set (4.30) with $\square_{\mathrm{lc}}^{\mathrm{m,b}}$ obtained from EL measurements and χ and $i_{\mathrm{lk}}^{\mathrm{m,b}}$ as fitting parameters. $i_{\mathrm{ph}}^{\mathrm{m}}$ is taken from the EQE measurement in the InGaAs wavelength range, and $i_{\mathrm{ph}}^{\mathrm{b}}$ is obtained using the pulse bias methods in Chapter V. The leakage strength $i_{\mathrm{lk}}^{\mathrm{m,b}}$ is

determined as 8.5% at 780 nm from the fitting. The luminescence coupling strength calculated from the luminescence coupling current $I_{LC}^{M,B}$ shown in Fig. 4.9 increases with the recombination current $I(D^M)$ of the InGaAs subcell, because of the increased radiative recombination efficiency. As shown in Fig. 4.8, the luminescence coupling effect becomes more severe with the increase of the photocurrent I_{BS}^{M}, because the measured output current i_o decreases at 980 nm and increases at 780 nm. Therefore, the bias light intensity on the InGaAs subcell should be set as low as possible to minimize the luminescence coupling effect.

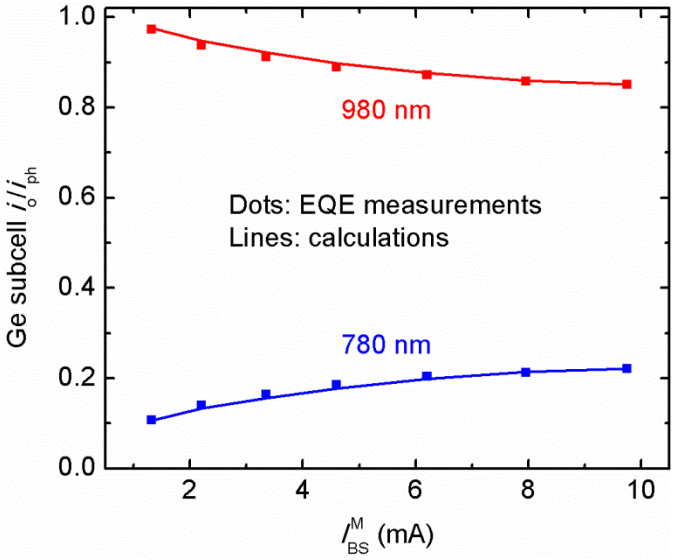

Fig. 4.8. i_o/i_{ph} of the Ge subcell in the Ge and InGaAs wavelength ranges obtained from Fig. 4.1 (b) (dots) and from the calculations (lines) using Eq. set (4.30) at the optimal bias voltage 0 V.

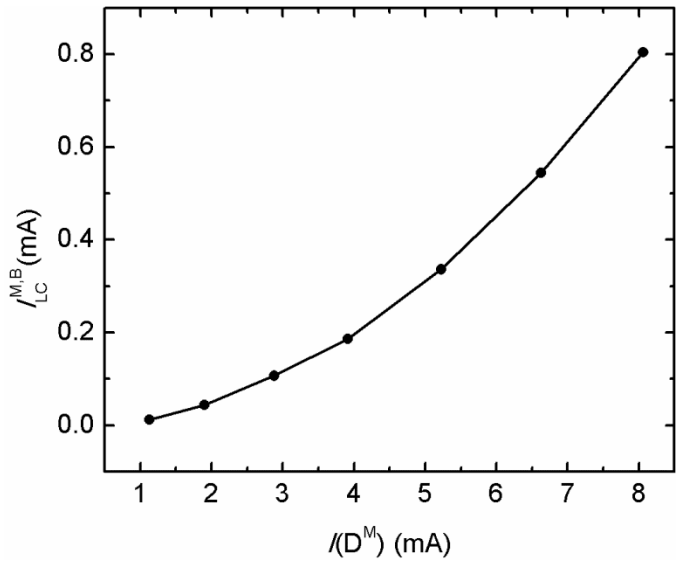

Fig. 4.9. The luminescence coupling current $i_{\mathrm{LC}}^{\mathrm{M,B}}$ from the InGaAs middle cell to the Ge bottom cell versus the recombination current $I(\mathrm{D^M})$ of the InGaAs middle cell.

4.7.3 Combined Effects of Shunt and Luminescence Coupling

The measurement artifacts of the Ge subcell of the triple junction solar cell S2 shown in Fig. 4.1 (c) are caused by the combined effects of shunt and luminescence coupling at the bias voltage -0.5 V. According to Eq. (4.22a), (4.23a) and (4.24a), the combined effects of shunt and luminescence coupling can be characterized using the optical leakage strength, the luminescence coupling strength and the small signal resistances. The optical leakage strength and luminescence coupling strength for solar cell S2 are determined at the optimal bias voltage 0 V as shown in Section 4.5.1. The small signal resistances are determined from the subcell *I*-*V* in Fig. 4.10 at the operating points in the EQE

measurements. The *I-V* curves of the forward biased InGaP and InGaAs subcells are measured using the I_{sc}-V_{oc} method. The solar cell S2 does not have the luminescence coupling effect between the InGaP and InGaAs subcells. For solar cells with luminescence coupling between the InGaP and InGaAs subcells, the luminescence coupling current in the InGaAs subcell is increased from the short circuit to the open circuit condition with the increase of the recombination current of the InGaP subcell, and therefore V_{oc} is increased and the points (I_{sc}, V_{oc}) are not on the pseudo *I-V* of the InGaAs subcell anymore. However, this effect is usually insignificant because the luminescence coupling current is much less than the photocurrent generated by the bias light and the light leakage. The reverse *I-V* of the Ge subcell is obtained from a reverse voltage sweep. The photocurrent measured at the short circuit is caused by the optical leakage and luminescence coupling effect. The luminescence coupling current varies with the bias voltage, while the optical leakage current is a constant under a certain light bias. The luminescence coupling current as a function of bias voltage or recombination current of the InGaAs subcell is calculated from Fig. 4.7, and is subtracted from the current measured at the corresponding voltage. The rest of the short circuit current is attributed to the leakage light. The extracted *I-V* of the Ge subcell of the triple junction solar cell S2 also shows a soft breakdown in the reverse bias as shown in Fig. 4.10.

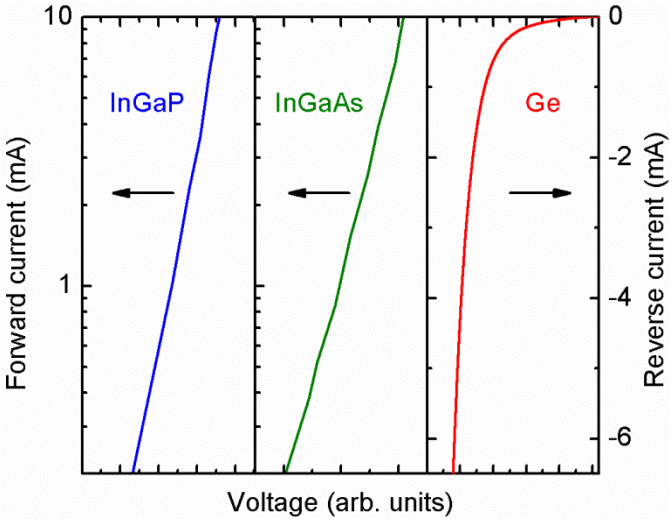

Fig. 4.10. Measured forward *I-V* curves of the InGaP and InGaAs subcells and the reverse *I-V* curve of the Ge subcell of the triple junction solar cell S2.

Fig. 4.11 compares i_o/i_{ph}^{b} and i_o/i_{ph}^{m} obtained at 980 nm and 780 nm of the EQE spectra in Fig. 4.1 (c), and those calculated using Eq. (4.23a) and (4.24a). It can be seen that i_o/i_{ph}^{b} increases and then decreases with the photocurrent i_{BS}^{M} of the InGaAs subcell at 980 nm, and the trend of i_o/i_{ph}^{m} is opposite at 780 nm. When i_{BS}^{M} decreases, the InGaAs subcell becomes less forward biased and its small signal resistance becomes comparable to the shunt resistance of the Ge subcell, making the artifact become worse. When i_{BS}^{M} increases, the voltage as well as the radiative recombination efficiency of InGaAs subcell increases, making the artifact become worse as well. The EQE measurement artifact is minimized at the i_{BS}^{M} of 1.8 mA which corresponds to the optimal bias light intensity on the InGaAs subcell, when the measured output current i_o reaches the

maximum at 980 nm and the minimum at 780 nm. It is dominated by the shunt effect at smaller bias light intensity and by the luminescence coupling effect at larger bias light intensity.

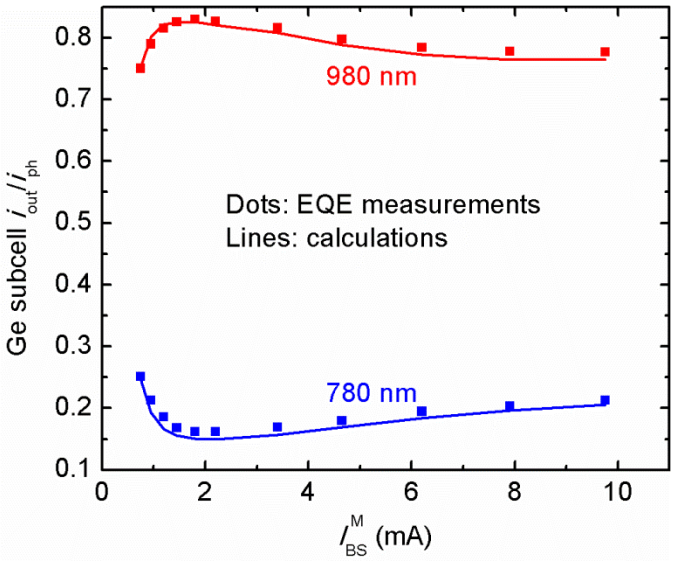

Fig. 4.11. i_o/i_{ph} of the Ge subcell in the Ge and InGaAs wavelength ranges obtained from Fig. 4.1 (c) (dots) and from the calculations (lines) using Eq. (4.23a) and (4.24a) at the bias voltage -0.5 V.

In order to understand the interplay of the shunt and luminescence coupling effects, SPICE simulations are performed for EQE measurement artifacts of a Ge subcell caused by both the shunt and luminescence coupling effects and by the shunt effect or the luminescence coupling effect alone, with the subcell parameters and bias conditions shown in Table 4.1. As shown in Fig. 4.12, i_o/i_{ph} calculated for both the shunt and luminescence coupling effects (squares) follows those with only the shunt effect (open triangles) at small I_{BS}^{M}, indicating

that the shunt effect dominates. As I_{BS}^{M} increases, the shunt effect is reduced (open triangles), because the small signal resistance of the InGaAs subcell decreases rapidly and the small signal resistance of the Ge subcell becomes dominant. At large I_{BS}^{M}, i_o/i_{ph} due to both effects follows those with only the luminescence coupling effect (open dots), indicating that the luminescence coupling effect dominates. Note that the luminescence coupling effect is slightly enhanced when the shunt effect is absent (open dots) at large I_{BS}^{M}. This is because the small signal resistance of the Ge subcell becomes larger as the shunt resistance increases, and the InGaAs subcell becomes more forward biased and generates stronger luminescence coupling to the Ge subcell. The optimal bias light intensity on the InGaAs subcell that minimizes the EQE measurement artifact of the Ge subcell is therefore determined by the tradeoff between the shunt and luminescence coupling effects.

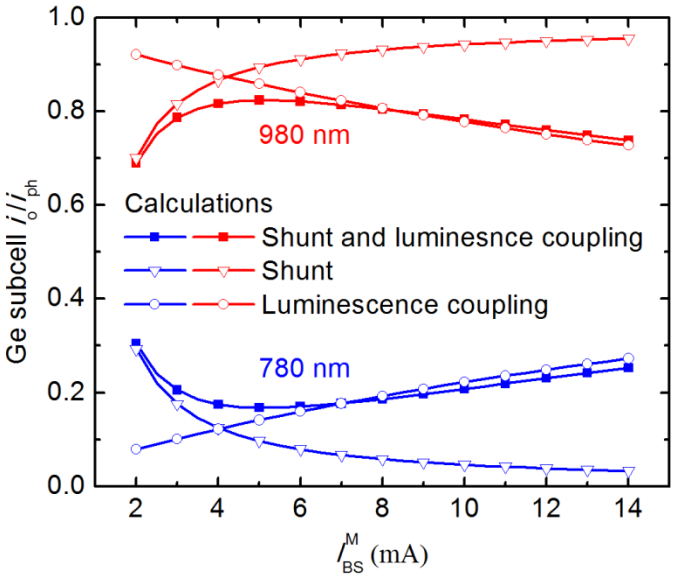

Fig. 4.12. Calculated i_o/i_{ph} of the Ge subcell in the Ge and InGaAs wavelength ranges, with both the shunt and luminescence coupling effects (squares), only the shunt effect (open triangles) and only the luminescence coupling effect (open dots), when the InGaAs photocurrent I_{BS}^{M} is increased.

Table 4.1. Subcell parameters and bias conditions in the simulations of Fig. 4.11

I_{0InGaP} (mA)	4.16×10^{-10}	I_{BS}^{M} (mA)	2-14
n_{InGaP}	2	V_A (V)	1.2 (reverse biased)
$I_{0InGaAs}$ (mA)	8×10^{-6}	$_{lk}$	0
n_{InGaAs}	2	$\alpha_{lc}^{t,m}$	0
I_{0Ge} (mA)	1.6×10^{-4}	$\alpha_{lc}^{m,b}$	$15I(D^M)^2$ (0 for shunt alone)
n_{Ge}	1	R_{SH}^{T} (Ω)	10^{10}
R_L (Ω)	1	R_{SH}^{M}(Ω)	10^{10}
I_{BS}^{T} (mA)	10	R_{SH}^{B}(Ω)	$10^6 exp[2.1V(D^B)]$ (10^{10} for only luminescence coupling)

References

[1] R. R. King, D. C. Law, C. M. Fetzer, R. A. Sherif, K. M. Edmondson, S. Kurtz, G. S. Kinsey, H. L. Cotal, D. D. Krut, J. H. Ermer, and N. H. Karam, "Pathways to 40%-efficient concentrator photovoltaics," in *Proc. 20th EU PVSEC*, Barcelona, pp. 118–123, Jun. 2005.

[2] R. R. King, C. M. Fetzer, D. C. Law, K. M. Edmondson, H. Yoon, G. S. Kinsey, D. D. Krut, J. H. Ermer, P. Hebert, B. T. Cavicchi, and N. H. Karam, "Advanced III-V multijunction cells for space," in *Proc. 4th WCPEC*, Waikoloa, pp. 1757–1762, May 2006.

[3] R. R. King, D. C. Law, K. M. Edmondson, C. M. Fetzer, G. S. Kinsey, H. Yoon, D. D. Krut, J. H. Ermer, R. A. Sherif, and N. H. Karam, "Advances in high-efficiency III-V multijunction solar cells," *Adv. Optoelectron.*, vol. 2007, pp. 1–9, 2007

[4] F. Dimroth and S. Kurtz, "High efficiency multijunction solar cells," MRS Bulletin, vol. 32, pp. 230–235, Mar. 2007.

[5] U. Rau, "Reciprocity relation between photovoltaic quantum efficiency and electroluminescent emission of solar cells," *Phys. Rev. B*, vol. 76, no. 8, pp. 085303-1–085303-8, Aug. 2007.

[6] G. S. Kinsey and K. M. Edmondson, "Spectral response and energy output of concentrator multijunction solar cells," *Prog. Photovolt: Res. Appl.*, vol. 17, no. 5, pp. 279–288, Aug. 2009.

[7] R. R. King, A. Boca, W. Hong, X.-Q. Liu, D. Bhusari, D. Larrabee, K. M. Edmondson, D. C. Law, C. M. Fetzer, S. Mesropian and N. H. Karam, "Band-gap-engineered architectures for high-efficiency multijunction concentrator solar cells," in *Proc. 24th EU PVSC*, Hamburg, pp. 55–61, Sep. 2009.

[8] D. J. Friedman, "Progress and challenges for next-generation high-efficiency multijunction solar cells," *Curr. Opin. Solid St. M.*, vol. 14, no. 6, pp. 131–138, 2010.

[9] D. C. Lawa, R. R. Kinga, H. Yoona, M. J. Archerb, A. Bocaa, C. M. Fetzera, S. Mesropiana, T. Isshikia, M. Haddada, K. M. Edmondsona, D. Bhusaria, J. Yena, R. A. Sherifa, H. A. Atwaterb, N. H. Karama, "Future technology pathways of terrestrial III-V multijunction solar cells for concentrator photovoltaic systems," Sol. Energ. Mat. Sol. C., vol. 94, no. 8, pp. 1314–1318, Aug. 2010.

[10] M. A. Steiner, J. F. Geisz, D. J. Friedman, W. J. Olavarria, A. Duda, and T. E. Moriarty, "Temperature-dependent measurements of an inverted metamorphic multijunction (IMM) solar cell," in *Proc. 37th IEEE PVSC*, Seattle, Jun. 2011, in press.

[11] S. H. Lim, J.-J. Li, C. R. Allen and Y.-H. Zhang, Characterization and modeling of spontaneous emission efficiency of forward biased multi-junction solar cells, *Proc. 37th IEEE PVSC*, Seattle, Jun. 2011, in press.

[12] M. Meusel, C. Baur, G. Létay, A. W. Bett, W. Warta, and E. Fernandez, "Spectral response measurements of monolithic GaInP/Ga (In) As/Ge triple-junction solar cells: Measurement artifacts and their explanation," *Prog. Photovolt: Res. Appl.*, vol. 11, no. 8, pp. 499–514, Dec. 2003.

[13] H. Yoon, R. R. King, G. S. Kinsey, S. Kurtz, and D. D. Krut, "Radiative coupling effects in GaInP/GaAs/Ge multijunction solar cells," in *Proc. 3rd WCPEC*, pp. 745–748, May 2003.

[14] C. Baur, M. Hermle, F. Dimroth, and A. W. Bett, "Effects of optical coupling in III-V multilayer systems," *Appl. Phys. Lett.*, vol. 90, pp. 192109-1–192109-3, May 2007.

[15] S. H. Lim, K. O'Brien, E. H. Steenbergen, J.-J. Li, D. Ding, and Y.-H. Zhang, "Analysis of spectral photocurrent response from multi-junction solar cells under variable voltage bias," in *Proc. 35th IEEE PVSC*, Hawaii, pp. 712–716, Jun. 2010.

[16] G. Siefer, C. Baur, and A. W. Bett, "External quantum efficiency measurements of germanium bottom subcells: measurement artifacts and correction procedures," in *Proc. 35th IEEE PVSC*, Hawaii, pp. 704–707, Jun. 2010.

[17] S. H. Lim, J.-J. Li, E. H. Steenbergen, and Y.-H. Zhang, "Luminescence coupling effects on multi-junction solar cell external quantum efficiency measurement," *Prog. Photovolt: Res. Appl.*, DOI: 10.1002/pip.1215, Nov. 2011.

[18] J.-J. Li, S. H. Lim, C. R. Allen, D. Ding, and Y. H. Zhang, "Combined effects of shunt and luminescence coupling on external quantum efficiency of multijunction solar cells," *IEEE J. Photovoltaics*, vol. 1, no. 2, pp. 225–230, Oct. 2011.

[19] P. T. Chiu, S. J. Wojtczuk, X. Zhang, C. Harris, and M. Timmons, "World record 42.3% efficient InGaP/GaAs/InGaAs concentrators using bifacial epigrowth," in *Proc. 37th IEEE PVSC*, Seattle, Jun. 2011, in press.

[20] T. Kirchartz, U. Rau, M. Hermle, A. W. Bett, A. Helbig, and J. H. Werner, "Internal voltages in GaInP⁄ GaInAs⁄ Ge multijunction solar cells determined by electroluminescence measurements," *Appl. Phys. Lett.*, vol. **92**, no. 12, pp. 123502–123502-3, 2008.

[21] R. A. Sinton and A. Cuevas, "A quasi-steady-state open-circuit voltage method for solar cell characterization," in *Proc. 16th EU PVSEC*, Glasgow, pp. 1152–1155, May 2000.

[22] A.G. Aberle, S. R. Wenham and M. A. Green, "A new method for accurate measurements of the lumped series resistance of solar cells," *Proc. 23th IEEE PVSC*, Louisville, pp. 133–139, May 1993.

[23] B. Chhabra, S. Jacobs and C. B. Honsberg, "Suns-Voc and Minority Carrier Lifetime Measurements of III-V Tandem Solar Cells," in *4th IEEE WCPEC*, pp. 791–794, Waikoloa, May 2006.

[24] C. R. Allen, S. H. Lim, J.-J. Li, and Y.-H. Zhang, "Simple method for determining luminescence coupling in multi-junction solar cells," in *Proc. 37th IEEE PVSC*, Seattle, Jun. 2011, in press.

V ELIMINATION OF MEASUREMENT ARTIFACTS IN EXTERNAL QUANTUM EFFICIENCY OF MULTI-JUNCTION SOLAR CELLS

5.1 Introduction

It has been demonstrated in Chapter IV that the EQE measurement artifacts can be minimized using proper DC light and voltage biases, but they cannot be completely eliminated by varying the DC biases for subcells with low shunt resistances and large luminescence coupling effects. This chapter presents the methods to eliminate the EQE measurement artifacts.

5.2 The Unity Rule

A unity rule derived from Eq. (4.22a), (4.23a) and (4.24a) as follows

$$\frac{i_{\mathrm{o}}^{\mathrm{t}}}{i_{\mathrm{ph}}^{\mathrm{t}}}+\frac{i_{\mathrm{o}}^{\mathrm{m}}}{i_{\mathrm{ph}}^{\mathrm{m}}}+\frac{i_{\mathrm{o}}^{\mathrm{b}}}{i_{\mathrm{ph}}^{\mathrm{b}}}=1\,, \tag{5.1}$$

has been proposed to recover the true EQE of a subcell when the series resistance and light leakage can be neglected [1], [2]. This can be proved using. For instance, if the photocurrent $i_{\mathrm{ph}}^{\mathrm{t}}$ and $i_{\mathrm{ph}}^{\mathrm{m}}$ of the top and middle subcells can be measured, the photocurrent $i_{\mathrm{ph}}^{\mathrm{b}}$ of the bottom subcell can be obtained using Eq. (5.1) with the measured output current $i_{\mathrm{o}}^{\mathrm{t}}$, $i_{\mathrm{o}}^{\mathrm{m}}$ and $i_{\mathrm{o}}^{\mathrm{b}}$ of the three subcells under the DC voltage and light biases.

The applicability of the unity rule has been limited by several constraints. Firstly, the light leakage may not be negligible for some solar cells. The leakage light generates the EQE that decreases with decreasing wavelength because of the increased absorption coefficient. The leakage strength is larger for thinner

subcells with lower absorption coefficients. Furthermore, the series resistance has to be considered in some cases. For example, if the voltage of the triple junction solar cells is measured as the EQE response, the load resistor R_L is necessary and a large resistance is desirable for a large measurement signal. In addition, the photocurrents of the InGaP and InGaAs subcells may not be ready to be obtained when they have large measurement artifacts.

5.3 Pulse Voltage Bias (PVB) Method

A more universal approach to eliminate the measurement artifacts is to use a pulse voltage bias [3], [4] or a pulse light bias [5] superimposed on the DC light and voltage biases to control the subcell operating points during the measurements and counterbalance the effects of shunt and luminescence coupling. This section discusses the pulse voltage bias (PVB) method.

5.3.1 Models and Principles

Fig. 5.1 shows the circuit models of EQE measurements of the Ge subcells of triple junction solar cells under the bias condition (a), and under the chopped monochromatic light in the Ge wavelength range (b) and in the InGaAs wavelength range (c) using the PVB method. The symbol definitions are the same as in Chapter IV. The output current i_o of the solar cells under the chopped monochromatic light is converted by R_{DC}=51 Ω to the voltage $v_{o,dc}$ (with the DC biases in the conventional method) or $v_{o,ac}$ (with the AC bias and the DC biases in the PVB method), and is then amplified by the voltage amplifier and measured by the lock-in amplifier.

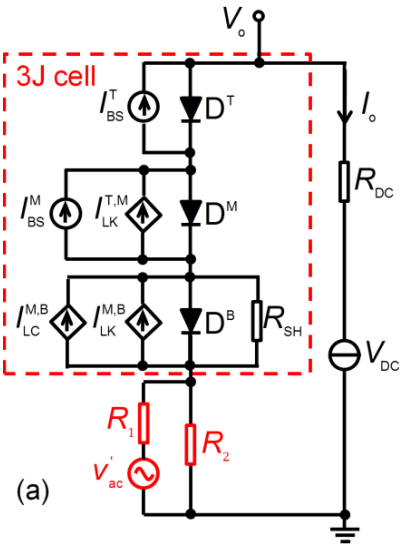
V_o
3J cell
I_{BS}^{T}
D^T
I_o
R_{DC}
I_{BS}^{M}
$I_{LK}^{T,M}$
D^M
$I_{LC}^{M,B}$
$I_{LK}^{M,B}$
D^B
R_{SH}
V_{DC}
R_1
R_2
v_{ac}'
(a)

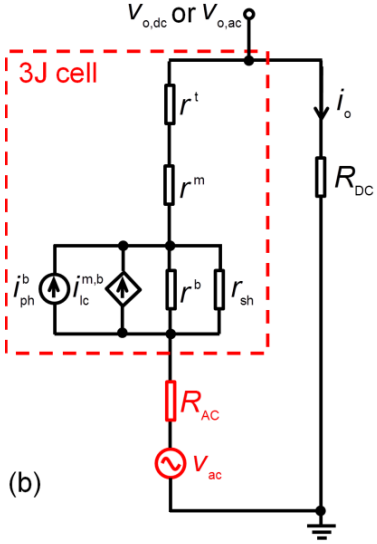
$v_{o,dc}$ or $v_{o,ac}$
3J cell
r^t
i_o
r^m
R_{DC}
i_{ph}^{b}
$i_{lc}^{m,b}$
r^b
r_{sh}
R_{AC}
v_{ac}
(b)

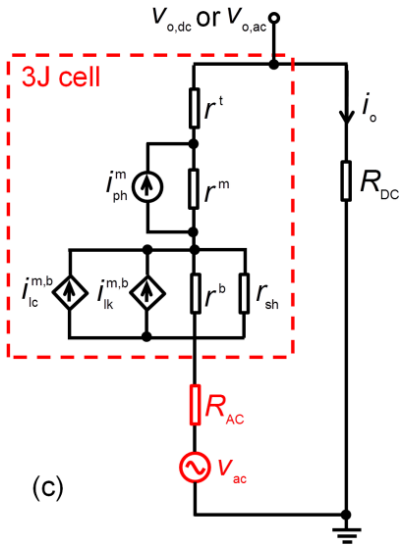

Fig. 5.1. Equivalent circuit models of EQE measurements of the Ge subcells of triple-junction solar cells under the bias condition using the PVB method (a), and under the chopped monochromatic light in the Ge wavelength range (b) and in the InGaAs wavelength range (c). The symbol D: Diode. Superscripts T (t), M (m), B (b): top, middle and bottom subcells. Subscript BS: bias light; SH (sh): shunt; LK (lk): light leakage; LC (lc): luminescence coupling and ph: photocurrent.

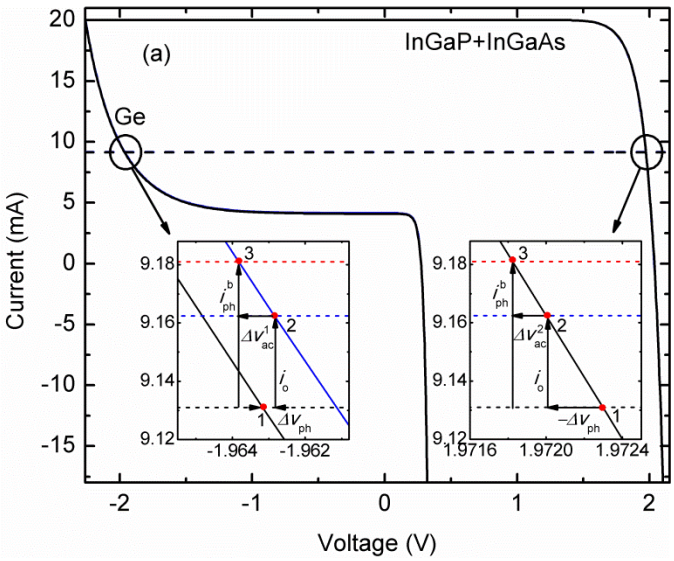

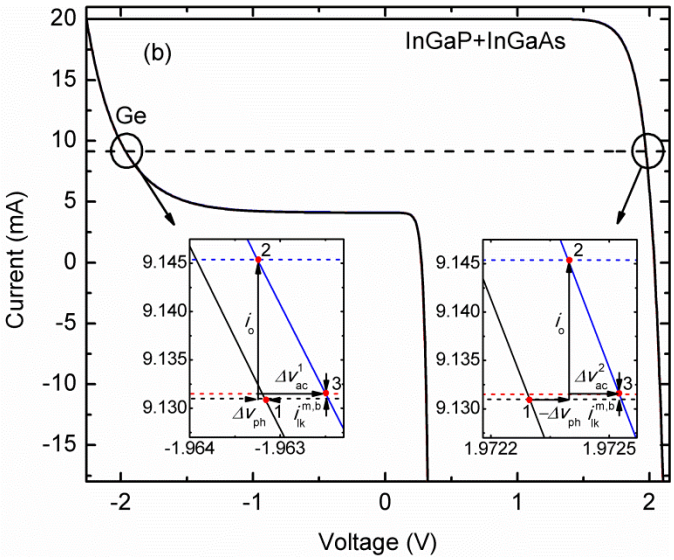

Fig. 5.2. Principle to eliminate the measurement artifacts using the pulse voltage bias in the Ge wavelength range (a) and in the InGaAs wavelength range (b).

As explained in Chapter IV, the EQE measurement artifacts comes from the fact that the AC output current i_o between the DC operating points 1 in Fig. 5.2 and the operating points 2 under the chopped monochromatic light is smaller than the photocurrent i_{ph}^{b} in the Ge wavelength range, and it is larger than the optical leakage current $i_{lk}^{m,b}$ in the InGaAs wavelength range. If the subcell operating points are moved to points 3 in Fig. 5.2 instead of points 2 under the chopped monochromatic light, i_o is equal to i_{ph}^{b} in the Ge wavelength range and it is equal to $i_{lk}^{m,b}$ in the InGaAs wavelength range. Therefore, the EQE measurement artifacts are eliminated [8]. A pulse voltage bias v_{ac} can be used to achieve this. The voltage v_{ac} is equal to the sum of the voltage drop Δv_{ac}^{1} on the Ge subcell and Δv_{ac}^{2} on the top two subcells.

5.3.2 Necessary Pulse Voltage Bias

A pulse generator (SRS DG535) $v_{\mathrm{ac}}^{'}$ with a voltage divider consisting of two resistors R_1 and R_2 is added into the bias condition shown in Fig. 5.1 (a), in order to eliminate the measurement artifacts. The pulse generator is synchronized to the chopped monochromatic light, and provides an effective voltage bias $v_{\mathrm{ac}} = v_{\mathrm{ac}}^{'} R_2/(R_1 + R_2)$ to the solar cells as shown in Fig. 5.1 (b) and (c). In order to make v_{ac} comparable to the voltage drops generated on the subcells by the chopped monochromatic light, R_1 and R_2 are chosen as 1 kΩ and 4.8 Ω in the Ge wavelength range and 10 kΩ and 2.4 Ω in the InGaAs wavelength range. v_{ac} can therefore be controlled to as low as 0.48 mV and 0.02 mV, and the equivalent load resistor $R_{\mathrm{AC}} = R_1 R_2/(R_1 + R_2)$ is approximately 4.8 Ω and 2.4 Ω, respectively

The output current i_{o} in the Ge wavelength range can be obtained from Fig. 5.1 (b) as

$$i_{\mathrm{o}} = \frac{v_{\mathrm{o,ac}}}{R_{\mathrm{DC}}} = \frac{i_{\mathrm{ph}}^{\mathrm{b}}\, r^{\mathrm{b}} r_{\mathrm{sh}} / \left(r^{\mathrm{b}} + r_{\mathrm{sh}}\right) + v_{\mathrm{ac}}}{r^{\mathrm{t}} + r^{\mathrm{m}} + \left(1 + \alpha_{\mathrm{lc}}^{\mathrm{m,b}}\right) r^{\mathrm{b}} r_{\mathrm{sh}} / \left(r^{\mathrm{b}} + r_{\mathrm{sh}}\right) + R_{\mathrm{AC}} + R_{\mathrm{DC}}}, \tag{5.2}$$

If there is no measurement artifact, i_{o} is equal to $i_{\mathrm{ph}}^{\mathrm{b}}$. Substituting this condition into Eq. (5.2), the magnitude of the necessary v_{ac}^{0} to recover the true EQE of the Ge subcell can be obtained as

$$\begin{aligned} v_{\mathrm{ac}}^{0} &= i_{\mathrm{ph}}^{\mathrm{b}} \left[r^{\mathrm{t}} + r^{\mathrm{m}} + \alpha_{\mathrm{lc}}^{\mathrm{m,b}}\, r^{\mathrm{b}} r_{\mathrm{sh}}^{\mathrm{b}} / \left(r^{\mathrm{b}} + r_{\mathrm{sh}}^{\mathrm{b}}\right) + R_{\mathrm{AC}} + R_{\mathrm{DC}} \right] \\ &= \frac{v_{\mathrm{o,ac}}^{0}}{R_{\mathrm{DC}}} \left[r^{\mathrm{t}} + r^{\mathrm{m}} + \alpha_{\mathrm{lc}}^{\mathrm{m,b}}\, r^{\mathrm{b}} r_{\mathrm{sh}}^{\mathrm{b}} / \left(r^{\mathrm{b}} + r_{\mathrm{sh}}^{\mathrm{b}}\right) + R_{\mathrm{AC}} + R_{\mathrm{DC}} \right], \end{aligned} \tag{5.3}$$

which shows that v_{ac}^{0} is in phase with $i_{\mathrm{ph}}^{\mathrm{b}}$ or the voltage $v_{\mathrm{o,dc}}$ measured by the lock-in amplifier under the DC bias condition. In practice, v_{ac}^{0} can be obtained by varying v_{ac} and measuring $v_{\mathrm{o,ac}}$ iteratively until Eq. (5.3) is satisfied. $v_{\mathrm{o,ac}}$ measured at v_{ac}^{0}, i.e. $v_{\mathrm{o,ac}}^{0}$, yields the true EQE of the Ge subcell. Because $i_{\mathrm{ph}}^{\mathrm{b}}$ may vary with the spectrum of the sun simulator, v_{ac}^{0} should be determined at each wavelength according to Eq. (5.3).

The output current i_{o} in the InGaAs wavelength range can be obtained from Fig. 5.1 (c) as

$$i_{\mathrm{o}} = \frac{v_{\mathrm{o,ac}}}{R_{\mathrm{DC}}} = \frac{i_{\mathrm{ph}}^{\mathrm{m}}\left[r^{\mathrm{m}} + \left(\alpha_{\mathrm{lc}}^{\mathrm{m,b}} + \alpha_{\mathrm{lk}}^{\mathrm{m,b}}\right) r^{\mathrm{b}} r_{\mathrm{sh}}^{\mathrm{b}} / \left(r^{\mathrm{b}} + r_{\mathrm{sh}}^{\mathrm{b}}\right)\right] + v_{\mathrm{ac}}}{r^{\mathrm{t}} + r^{\mathrm{m}} + \left(1 + \alpha_{\mathrm{lc}}^{\mathrm{m,b}}\right) r^{\mathrm{b}} r_{\mathrm{sh}}^{\mathrm{b}} / \left(r^{\mathrm{b}} + r_{\mathrm{sh}}^{\mathrm{b}}\right) + R_{\mathrm{AC}} + R_{\mathrm{DC}}}, \tag{5.4}$$

which shows that i_{o} consists of the contributions from the InGaAs photocurrent, the luminescence coupling current, the optical leakage current and v_{ac}. While the optical leakage current is the true Ge response, the InGaAs photocurrent and luminescence coupling current are sources of EQE measurement artifacts. Substituting $i_{\mathrm{o}} = i_{\mathrm{lk}}^{\mathrm{m,b}} = \alpha_{\mathrm{lk}}^{\mathrm{m,b}} i_{\mathrm{ph}}^{\mathrm{m}}$ into Eq. (5.4), the specific AC voltage bias v_{ac}^{0} that eliminates the measurement artifacts can be obtained as

$$v_{\mathrm{ac}}^{0} = i_{\mathrm{ph}}^{\mathrm{m}}\left[\alpha_{\mathrm{lk}}^{\mathrm{m,b}} r^{\mathrm{t}} + \left(\alpha_{\mathrm{lk}}^{\mathrm{m,b}} - 1\right) r^{\mathrm{m}} + \left(\alpha_{\mathrm{lk}}^{\mathrm{m,b}} - 1\right) \alpha_{\mathrm{lc}}^{\mathrm{m,b}} r^{\mathrm{b}} r_{\mathrm{sh}} / \left(r^{\mathrm{b}} + r_{\mathrm{sh}}\right) + \alpha_{\mathrm{lk}}^{\mathrm{m,b}} \left(R_{\mathrm{AC}} + R_{\mathrm{DC}}\right)\right], \tag{5.5}$$

where $i_{\mathrm{ph}}^{\mathrm{m}} = v_{\mathrm{o,dc}} / R_{\mathrm{DC}}$ is the photocurrent of the InGaAs subcell in the InGaAs wavelength range. Because the term of the bottom subcell usually dominates in Eq. (5.5), v_{ac}^{0} is in anti-phase with $i_{\mathrm{ph}}^{\mathrm{m}}$.

For high quality solar cells, the shunt resistance may be very large with strong luminescence coupling effect in the vicinity of the optimal DC bias voltage. Eq. (5.3) and (5.5) do not hold anymore because v_{ac}^{0} becomes a large signal. Therefore, the solar cells should be biased at a DC voltage away from the optimal bias voltage to make v_{ac}^{0} as a small signal perturbation about the DC operating points. For poor quality solar cells with low shunt resistances and weak luminescence coupling, Eq. (5.3) and (5.5) are simplified as [8]

$$v_{ac}^{0} = \frac{v_{o,ac}^{0}}{R_{DC}}\left[r^{t} + r^{m} + R_{AC} + R_{DC}\right], \tag{5.6}$$

$$v_{ac}^{0} = i_{ph}^{m}\left[\alpha_{lk}^{m,b} r^{t} + \left(\alpha_{lk}^{m,b} - 1\right) r^{m} + \alpha_{lk}^{m,b}\left(R_{AC} + R_{DC}\right)\right]. \tag{5.7}$$

In this case, v_{ac}^{0} is not affected by the shunt resistances of the Ge subcell or the luminescence coupling between the InGaAs and Ge subcells.

5.3.3 Simulation

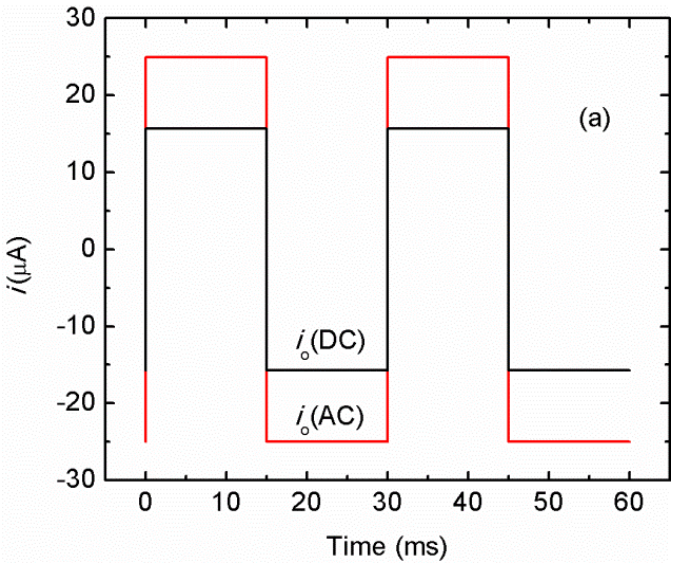

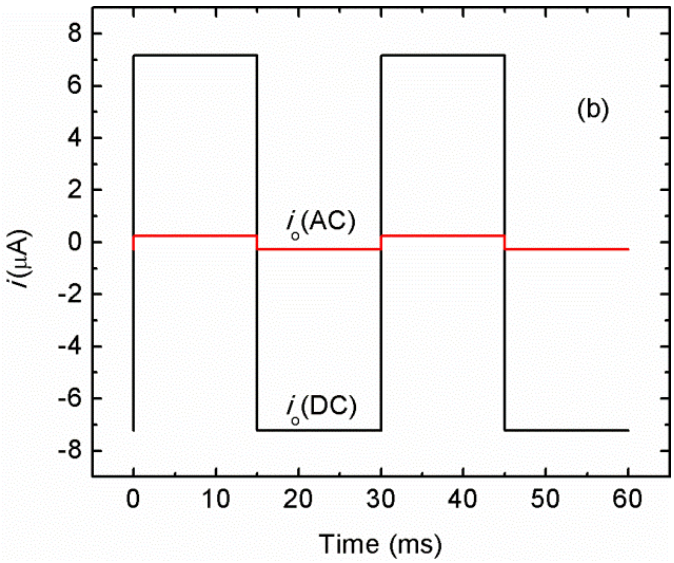

Fig. 5.4. Simulated waveforms of the output current $i_{\mathrm{o}}(\mathrm{DC})$ under the DC bias condition and $i_{\mathrm{o}}(\mathrm{AC})$ with the AC voltage bias in the EQE measurements of the Ge subcell in the Ge wavelength range (a) and the InGaAs wavelength range (b).

The EQE measurements of a Ge subcell are simulated using SPICE with the subcell parameters, bias condition and the chopped monochromatic light shown in Table 5.1. Under the DC bias condition, the small signal resistances of the InGaP, InGaAs and Ge subcells are $r^{\mathrm{t}} = 4.7\ \Omega$, $r^{\mathrm{m}} = 4.67\ \Omega$ and $r^{\mathrm{b}} = 40.2\ \Omega$, and the luminescence coupling strength between the InGaAs subcell and Ge subcell is $\alpha_{\mathrm{lc}}^{\mathrm{m,b}} = 33.2\%$. Figure 5.4 (a) and (b) show the simulation results of the output current i_{o} generated by the chopped monochromatic light in the Ge wavelength range and in the InGaAs wavelength range, respectively. Due to the shunt and luminescence coupling effects, the output current $i_{\mathrm{o}}(\mathrm{DC})$ under the DC bias condition is 62.8% of the photocurrent $i_{\mathrm{ph}}^{\mathrm{b}}$ generated in the Ge subcell in the

Ge wavelength range, and it is about 28.7% of the photocurrent $i_{\mathrm{ph}}^{\mathrm{m}}$ generated in the InGaAs subcell in the InGaAs wavelength range. In order to eliminate the EQE measurement artifacts, the necessary pulse voltage bias v_{ac} is equal to 1.18 mV peak-to-peak and is in phase with $i_{\mathrm{ph}}^{\mathrm{b}}$ in the Ge wavelength range according to Eq. (5.3), and it is equal to 0.89 mV peak-to-peak and is in anti-phase with $i_{\mathrm{ph}}^{\mathrm{m}}$ in the InGaAs wavelength range according to Eq. (5.5). As shown in Fig. 5.4, the output current $i_{\mathrm{o}}(\mathrm{AC})$ with the pulse voltage bias is equal to $i_{\mathrm{ph}}^{\mathrm{b}}$ in the Ge wavelength range and is 1% of $i_{\mathrm{ph}}^{\mathrm{m}}$ due to the leakage current in the InGaAs wavelength range. Therefore, the EQE measurement artifacts are eliminated using v_{ac}.

Table 5.1. Subcell parameters and bias conditions in the simulations of Fig. 5.4

$I_{0\mathrm{InGaP}}$ (mA)	4.16×10^{-10}	$I_{\mathrm{BS}}^{\mathrm{M}}$ (mA)	20
n_{InGaP}	2	V_{DC} (V)	0
$I_{0\mathrm{InGaAs}}$ (mA)	8×10^{-6}	$\alpha_{\mathrm{LK}}^{\mathrm{T,M}}$, $\alpha_{\mathrm{LK}}^{\mathrm{M,B}}$	1%
n_{InGaAs}	2	$R_{\mathrm{SH}}^{\mathrm{T}}$ (Ω)	10^{10}
$I_{0\mathrm{Ge}}$ (mA)	1.6×10^{-4}	$R_{\mathrm{SH}}^{\mathrm{M}}$(Ω)	10^{10}
n_{Ge}	1	$R_{\mathrm{SH}}^{\mathrm{B}}$(Ω)	$10^{5}exp[3V^{\mathrm{B}}]$
R_{L} (Ω)	1	$i_{\mathrm{ph}}^{\mathrm{b}}$	Peak-to-peak amplitude 50 μA Period 30 ms Duty cycle 50%
$I_{\mathrm{BS}}^{\mathrm{T}}$ (mA)	20	$i_{\mathrm{ph}}^{\mathrm{m}}$	

5.3.4 Measurements

5.3.4.1 Waveforms

A necessary condition to eliminate the EQE measurement artifacts is that v_{ac} is in phase with $v_{\mathrm{o,dc}}$ measured under the DC bias condition in the Ge wavelength range and is in anti-phase with $v_{\mathrm{o,dc}}$ in the InGaAs wavelength range. Figure 5.5 (a) and (b) show respectively the waveforms of the voltage $v_{\mathrm{o,ac}} = v_{\mathrm{o,dc}} + v_{\mathrm{ac}}$ and $v_{\mathrm{o,ac}} = v_{\mathrm{o,dc}} - v_{\mathrm{ac}}$ measured at a certain set of $v_{\mathrm{o,dc}}$ and the pulse voltage v_{ac}. It can be seen that $v_{\mathrm{o,dc}}$ is a trapezoidal wave due to the beam size of the sun simulator, and v_{ac} generated by the pulse generator is a square wave. The waveform of $v_{\mathrm{o,ac}}$ therefore depends on the amplitudes and phase difference of the trapezoidal wave $v_{\mathrm{o,dc}}$ and the square wave v_{ac} as shown in Fig. 5.5 (a) and (b). The rising and falling edges of $v_{\mathrm{o,ac}}$ do not generate appreciable errors in the lock-in readings as confirmed by additional measurements using a gated integrator and boxcar averager (SR250).

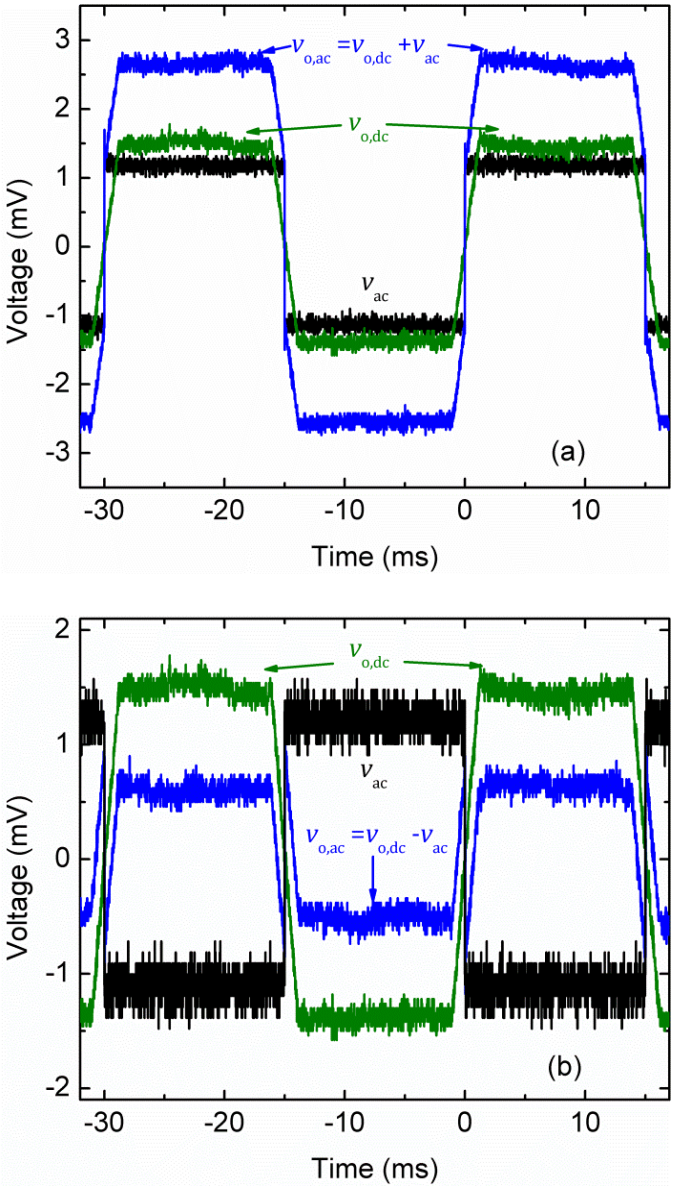

Fig. 5.5. Waveforms of the voltage $v_{o,ac} = v_{o,dc} + v_{ac}$ (a) and $v_{o,ac} = v_{o,dc} - v_{ac}$ (b) measured at a certain set of $v_{o,dc}$ measured under the DC condition and the pulse voltage bias v_{ac}.

5.3.4.2 Shunt Effect

For simplicity, the PVB method is firstly applied for triple junction solar cells with only the shunt effect. Fig. 5.6 compares the EQE measured with the conventional method and the PVB method at 980 nm in the Ge wavelength range for the Ge subcell of the triple junction solar cell S1. Using the conventional method, the measured EQE reaches the maximum of 58.5% at the optimal V_{DC} of 1.9 V, and it drops when V_{DC} increases or decreases due to the decrease of small signal diode resistance and shunt resistance of the Ge subcell respectively [3,4]. With the PVB method, the EQE is measured as about 86.5% at $1.3\ \text{V} \leq V_{\text{DC}} \leq 2.1\ \text{V}$, and it decreases as V_{DC} increases or decreases.

The variation of EQE measured using the PVB method can be explained by the variations of subcell characteristics with V_{DC}, as revealed by the small signal diode resistances r^{t} and r^{m} of the InGaP and InGaAs subcells determined using the I_{sc}-V_{oc} method. The small signal resistance of the Ge subcell is not considered because it does not affect v_{ac}^{0} according to Eq. (5.6). As shown in Fig. 5.6, for $V_{\text{DC}} > 2.1$ V, the recombination currents $I(\text{D}^{\text{T}})$ and $I(\text{D}^{\text{M}})$ of the InGaP and InGaAs subcells increase rapidly with the increase of V_{DC}, causing the fast decrease of r^{t} and r^{m}. This indicates that the Ge subcell is turned on and its small signal resistance $r^{\text{b}}r_{\text{sh}}/\left(r^{\text{b}} + r_{\text{sh}}\right)$ becomes very small. According to Eq. (5.2), i_{o}does not contain much information about the EQE in this case. For $V_{\text{DC}} < 1.3$ V, the reverse shunting current of the Ge subcell increases rapidly, causing $r^{\text{b}}r_{\text{sh}}/\left(r^{\text{b}} + r_{\text{sh}}\right)$ to be very small again. Furthermore, $I(D^{\text{T}})$ and $I(D^{\text{M}})$ decrease rapidly and r^{t} and r^{m} increase rapidly at the small current levels, as shown in Fig.

5.7. Therefore, as the modulation of the chopped monochromatic light makes $I(D^{\mathrm{T}})$ and $I(D^{\mathrm{M}})$ decrease slightly, r^{t} and r^{m} may increase slightly from the DC bias condition. As a result of these effects, the EQE is underestimated using v_{ac}^{0} determined from Eq. (5.3) for $V_{\mathrm{DC}} > 2.1$ V and $V_{\mathrm{DC}} < 1.3$ V. The best operating condition to apply the PVB method is at $1.3\ \mathrm{V} \leq V_{\mathrm{DC}} \leq 2.1\ \mathrm{V}$. In this range, the small signal resistance of the Ge subcell is at a relatively large value, and the top two subcells are strongly forward biased so that their small signal resistances do not change during the measurements. In practice, for subcells dominated by the shunt effect, v_{ac}^{0} can be determined at the optimal DC bias voltage with large light biases on the top two subcells to make them strongly forward biased.

The EQE spectra in Fig. 4.1 (a) shows that the optical leakage can be neglected in the InGaAs wavelength range, because the EQE does not decrease with decreasing wavelength in spite of the increased absorption coefficient. Therefore, Eq. (5.7) is further simplified as

$$v_{\mathrm{ac}}^{0} = -i_{\mathrm{ph}}^{\mathrm{m}} r^{\mathrm{m}} . \tag{5.9}$$

Eq. (5.4) shows that i_{o} is zero at v_{ac}^{0} in the InGaAs wavelength range when there is only the shunt effect and the optical leakage is negligible. This is confirmed by EQE measurements of the solar cell at 780 nm and $1.3\ \mathrm{V} < V_{\mathrm{DC}} < 2.1\ \mathrm{V}$.

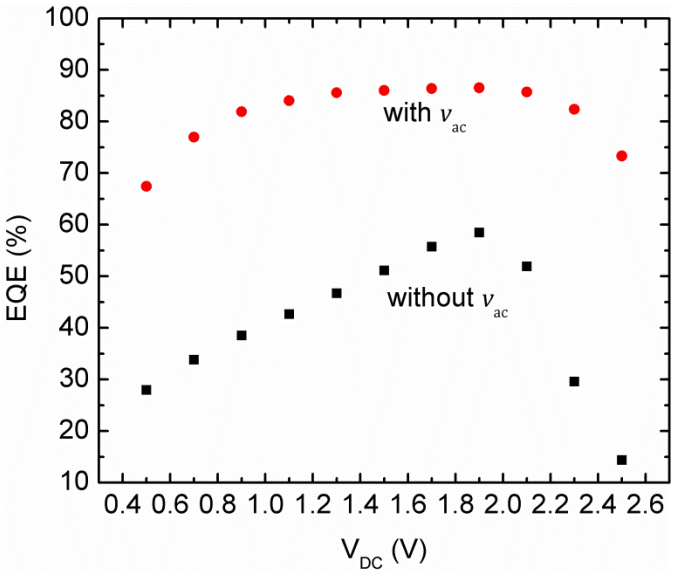

Fig. 5.6. EQE measured using the conventional method (dark dots) and the PVB method (red dots) at 980 nm in the Ge wavelength range for the Ge subcell of triple junction solar cell S1.

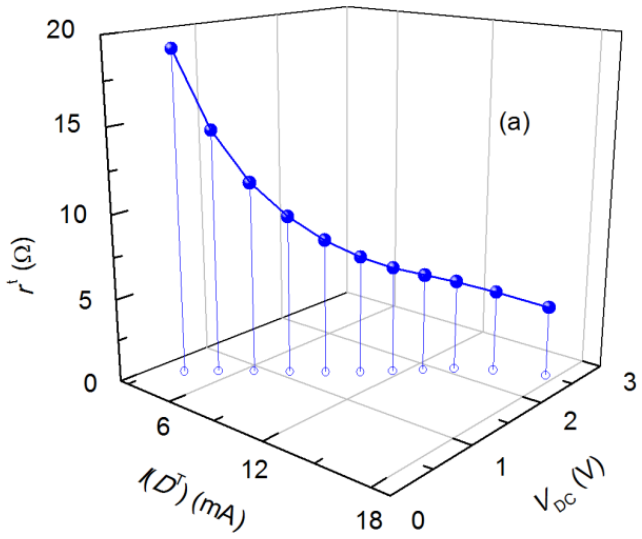

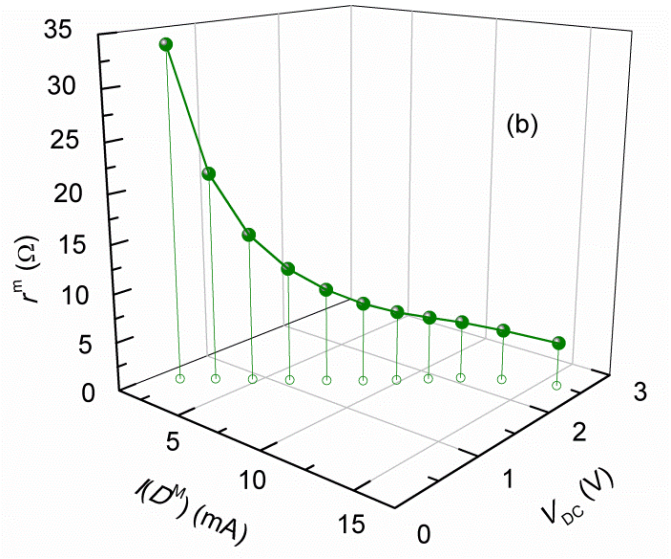

Fig. 5.7. Small signal diode resistance r^t of the InGaP subcell (a) and r^m of the InGaAs subcell (b) in the EQE measurements shown in Fig. 5.6.

5.3.4.3 Combined Effects of Shunt and Luminescence Coupling

The PVB method is also applied for triple junction solar cells with the combined effects of shunt and luminescence coupling. Fig. 5.8 shows the EQE measured with the conventional method and the PVB method at 980 nm in the Ge wavelength range and 780 nm in the InGaAs wavelength range for the Ge subcell of triple junction solar cell S2. The solar cell is biased at -0.5 V, which is smaller than the optimal bias voltage 0 V, to reduce the Ge shunt resistance and obtain v_{ac}^{0} that only generates a small signal excursion from the DC characteristics. . The EQE measured using the conventional method reaches the maximum of 64% at 980 nm and the minimum of 14% at 780 nm at the photocurrent $I_{\mathrm{BS}}^{\mathrm{M}}$ 1.8 mA corresponding to the optimal bias light intensity on the InGaAs subcell. The EQE

decreases in the Ge wavelength range at smaller and larger $I_{\mathrm{BS}}^{\mathrm{M}}$ because of the shunt effect and the luminescence coupling effect, respectively, and it changes in the opposite manner in the InGaAs wavelength range. With the PVB method, the EQE is measured as about 80.8% at 980 nm in the Ge wavelength range and 7.5% at 780 nm in the InGaAs wavelength range at 1 mA $\leq I_{\mathrm{BS}}^{\mathrm{M}} \leq$ 4.5 mA. It decreases at smaller $I_{\mathrm{BS}}^{\mathrm{M}}$ and increases at larger $I_{\mathrm{BS}}^{\mathrm{M}}$ in the Ge wavelength range, and the trend is opposite in the InGaAs wavelength range.

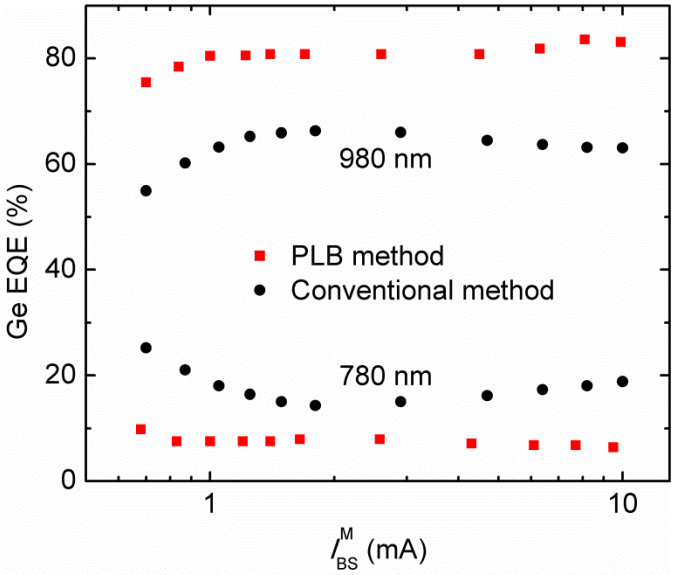

Fig. 5.8. EQE measured using the conventional method (dark dots) and the PVB method (red dots) for the Ge subcell of triple junction solar cell S2 at the DC bias voltage of -0.5 V.

The necessary pulse voltage bias v_{ac}^{0} that eliminates the measurement artifacts is obtained with the small signal resistances r^{t}, r^{m} and $r^{\mathrm{b}} r_{\mathrm{sh}} / \left(r^{\mathrm{b}} + r_{\mathrm{sh}}\right)$ in Fig. 5.9, the luminescence coupling strength $\alpha_{\mathrm{lc}}^{\mathrm{m,b}}$ in Fig. 5.10, and the optical

leakage strength of 7.5%. The slight differences of these parameters determined for the solar cell S2 from the other sections are caused by the change of optical alignment. As $I_{\mathrm{BS}}^{\mathrm{M}}$ increases, the InGaAs subcell becomes more forward biased, causing $I(D^{\mathrm{M}})$ to increase and r^{m} to decrease as shown in Fig. 5.9 (b). The strongly light biased InGaP subcell becomes slightly less forward biased, causing $I(D^{\mathrm{T}})$ to decrease and r^{t} to increase slightly as shown in Fig. 5.9 (a). Meanwhile, the Ge subcell becomes more reverse biased, and then less reverse biased as a result of the increased optical leakage current and luminescence coupling current at large $I_{\mathrm{BS}}^{\mathrm{M}}$. Therefore, $r^{\mathrm{b}}r_{\mathrm{sh}}/\left(r^{\mathrm{b}}+r_{\mathrm{sh}}\right)$ decreases and then increases as shown in Fig. 5.9 (c). Fig. 5.10 shows that $\alpha_{\mathrm{lc}}^{\mathrm{m,b}}$ increases as the InGaAs subcell becomes more forward biased, because of the increased radiative recombination efficiency in the InGaAs subcell.

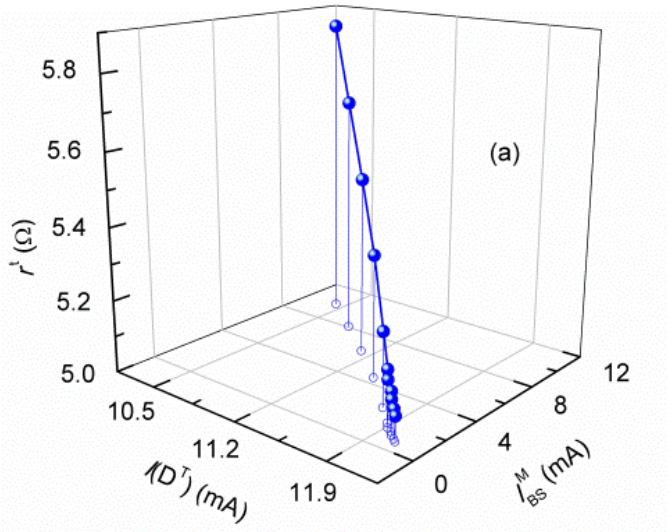

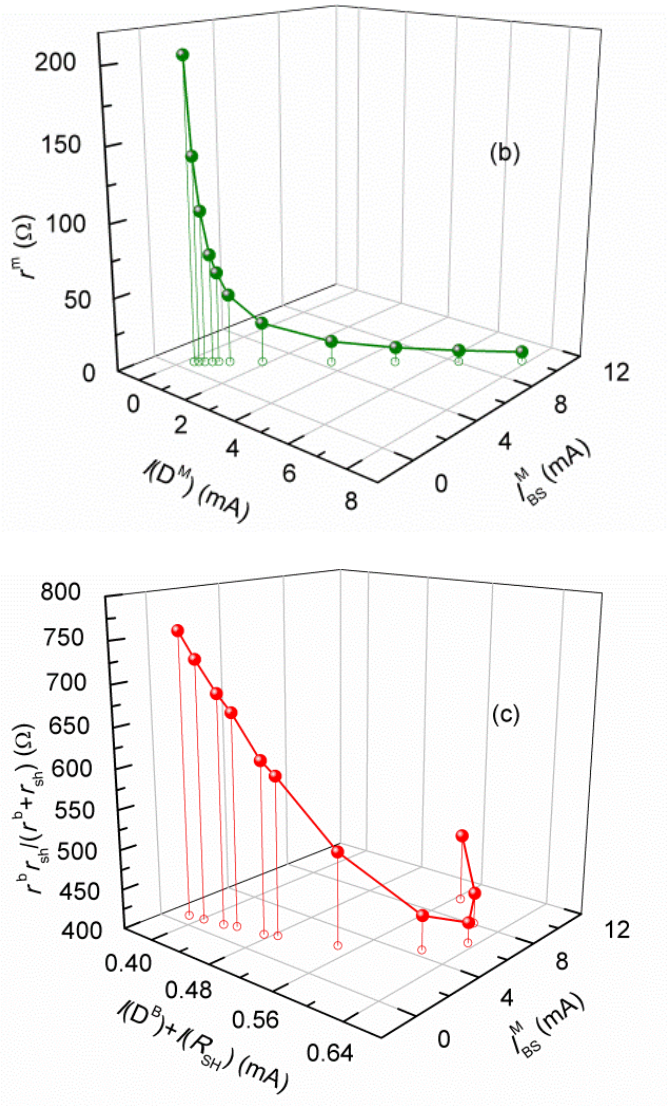

Fig. 5.9. Small signal resistances r^{t}, r^{m} and $r^{\mathrm{b}}r_{\mathrm{sh}}/\left(r^{\mathrm{b}}+r_{\mathrm{sh}}\right)$ of the three subcells in the EQE measurements shown in Fig. 5.8.

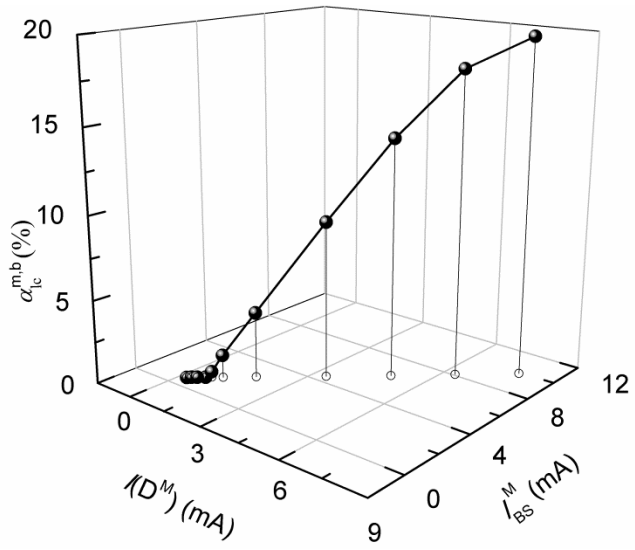

Fig. 5.10. Luminescence coupling strength $\alpha_{\mathrm{lc}}^{\mathrm{m,b}}$ between the InGaAs and Ge subcells in the EQE measurements shown in Fig. 5.8.

The variation of EQE measured using the PVB method can be attributed to the change of subcell characteristics with $I_{\mathrm{BS}}^{\mathrm{M}}$. At $I_{\mathrm{BS}}^{\mathrm{M}} < 1$ mA, $\alpha_{\mathrm{lc}}^{\mathrm{m,b}}$ is very small, r^{m} and $r^{\mathrm{b}} r_{\mathrm{sh}}/\left(r^{\mathrm{b}} + r_{\mathrm{sh}}\right)$ increase rapidly with the decrease of the respective subcell current $I(D^{\mathrm{M}})$ and $I(D^{\mathrm{B}}) + I(R_{\mathrm{SH}})$. As the modulation of the chopped monochromatic light makes $I(D^{\mathrm{M}})$ and $I(D^{\mathrm{B}}) + I(R_{\mathrm{SH}})$ decrease slightly, r^{m} and $r^{\mathrm{b}} r_{\mathrm{sh}}/\left(r^{\mathrm{b}} + r_{\mathrm{sh}}\right)$ may increase from the DC bias condition. Therefore, v_{ac}^{0} is underestimated using Eq. (5.7) and (5.9). At $I_{\mathrm{BS}}^{\mathrm{M}} > 4.5$ mA, the luminescence coupling effect becomes dominant. Because $\alpha_{\mathrm{lc}}^{\mathrm{m,b}}$ may decrease when $I(D^{\mathrm{M}})$ decreases slightly under the modulation of the monochromatic light, v_{ac}^{0} is overestimated using Eq. (5.7) and (5.9). Therefore, the best operating condition to apply the PVB method is at 1 mA $\leq I_{\mathrm{BS}}^{\mathrm{M}} \leq$ 4.5 mA, where v_{ac}^{0} is not affected by

the variations of small signal resistances and luminescence coupling strength under the modulation of the monochromatic light. In practice, v_{ac}^{0} can be determined in the vicinity of the optimal bias light intensity, while the solar cell is biased at a DC voltage where the shunt resistance of the subcell under test is not very large. In addition, in the InGaAs wavelength range, i_{o} measured using the PVB method is about 8.5% of $i_{\mathrm{ph}}^{\mathrm{m}}$ at 1 mA $\leq I_{\mathrm{BS}}^{\mathrm{M}} \leq$ 4.5 mA, which is in reasonably good agreement with the optical leakage strength 7.5% determined under the DC bias condition. This confirms that the measurement artifacts are eliminated.

5.4 Pulse Light Bias (PLB) Method

5.4.1 Principles and Models

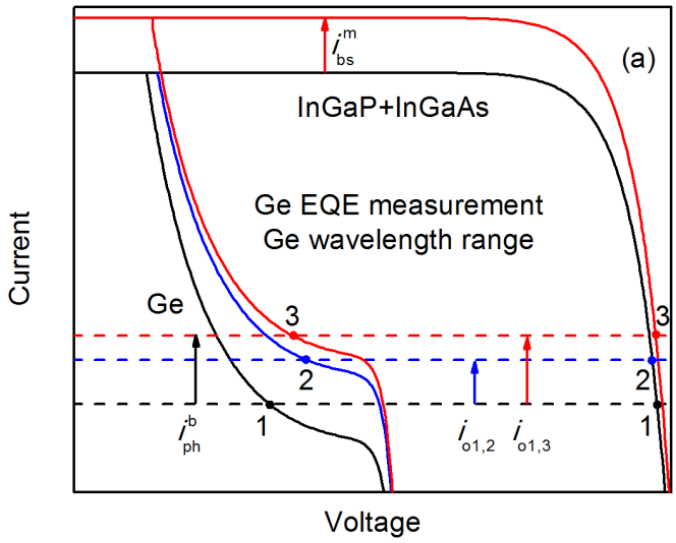

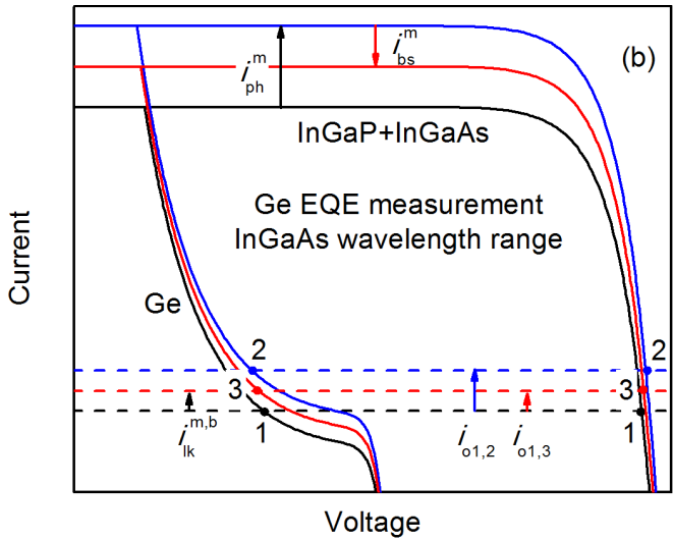

Fig. 5.11. Principle to eliminate the measurement artifacts using the pulse light bias in the Ge wavelength range (a) and in the InGaAs wavelength range (b).

Fig. 5.11 (a) and (b) show the schematic subcell I-V curves of a InGaP/InGaAs/Ge triple junction solar cell in the EQE measurements of the Ge subcell in the Ge wavelength range and in the InGaAs wavelength range, respectively. The InGaP and InGaAs subcells are light biased and therefore generate large short-circuit currents. The Ge subcell is current limiting, and it typically has a soft breakdown under reverse bias. The output currents from the MJ stack are shown by the dashed lines in Fig. 5.11. The intersections of the subcell *I-V* curves and the output current are the subcell operating points. The subcells work at points 1 under the DC bias condition and points 2 when the probing monochromatic light is on. The incremental current from point 1 to point 2 is the AC output current $i_{o1,2}$ which is measured as the apparent spectral response of the Ge subcell. The Ge cell *I-V* curve is tilted at the operating points because of

the low shunt resistance. Moreover, the luminescence coupling effect causes a negative feedback on the output current in the Ge wavelength range and an additional photocurrent in the InGaAs wavelength range [6]. As a result, $i_{o1,2}$ in the Ge wavelength range as shown in Fig. 5.11 (a) is smaller than the actual spectral response i_{ph}^{b} generated by the Ge subcell absorbing the probing monochromatic light. $i_{o1,2}$ in the InGaAs wavelength range as shown in Fig. 5.11 (b) is larger than the actual spectral response $i_{lk}^{m,b}$, i.e. the optical leakage current, generated by the Ge subcell absorbing the unabsorbed probing monochromatic light from the InGaAs subcell. These are the origins of the EQE measurement artifacts. In order to eliminate these measurement artifacts, a pulsed light bias is applied to the InGaAs subcell and generates an AC photocurrent i_{bs}^{m} to correct the discrepancy between the measured apparent spectral response i_{o} and the actual spectral response. More specifically, the pulsed light bias causes the photocurrent of the InGaAs subcell to increase or decrease by i_{bs}^{m} in the Ge wavelength range in Fig. 5.11 (a) or the InGaAs wavelength range in Fig. 5.11 (b), respectively. As a result, the subcell operating points are moved from points 2 to points 3 under the probing monochromatic light, where the measured apparent spectral response $i_{o1,3}$ in the respective wavelength range of the Ge subcell and the InGaAs subcell is equal to the photocurrent i_{ph}^{b} as shown in Fig. 5.11 (a) and the optical leakage current $i_{lk}^{m,b}$ as shown in Fig. 5.11 (b). Therefore, the measurement artifacts are eliminated.

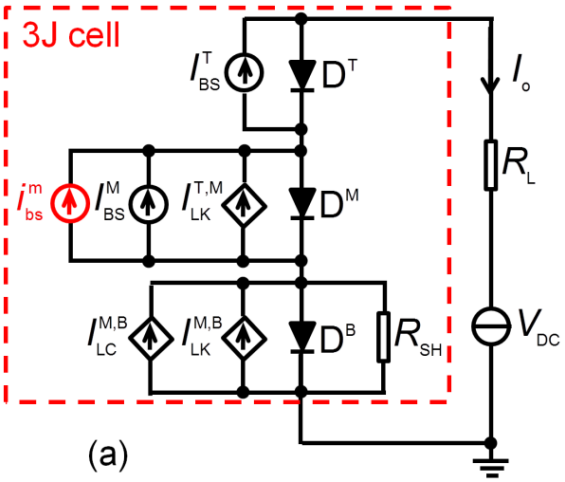
3J cell
I_{BS}^{T}
D^{T}
I_o
R_L
i_{bs}^{m}
I_{BS}^{M}
$I_{LK}^{T,M}$
D^{M}
$I_{LC}^{M,B}$
$I_{LK}^{M,B}$
D^{B}
R_{SH}
V_{DC}

(a)

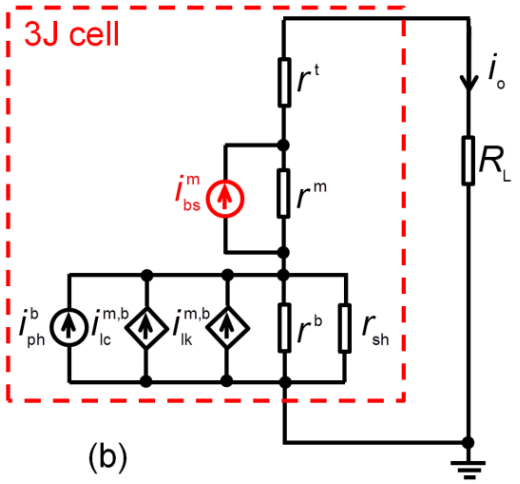
3J cell
r^{t}
i_o
R_L
i_{bs}^{m}
r^{m}
i_{ph}^{b}
$i_{lc}^{m,b}$
$i_{lk}^{m,b}$
r^{b}
r_{sh}

(b)

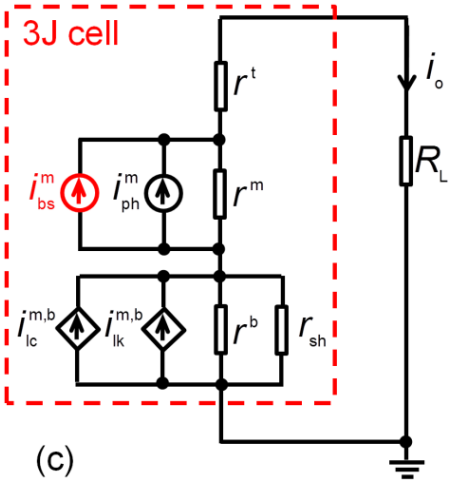
3J cell
r^{t}
i_o
R_L
i_{bs}^{m}
i_{ph}^{m}
r^{m}
$i_{lc}^{m,b}$
$i_{lk}^{m,b}$
r^{b}
r_{sh}

(c)

Fig. 5.12. Models of the triple-junction solar cells under the bias condition (a), and under the chopped monochromatic light in the Ge wavelength range (b) and in the InGaAs wavelength range (c) of the EQE measurements of Ge subcells. The symbol D: Diode. Superscripts T (t), M (m), B (b): top, middle and bottom subcells. Subscript BS (bs): bias light; LK (lk): light leakage; LC (lc): luminescence coupling and ph: AC photocurrent.

Circuit models are used to quantitatively study the coupling effects between the subcells. In this paper, DC signals are denoted as uppercase letters with uppercase subscripts and superscripts, AC signals are denoted as lowercase letters with lowercase subscripts and superscripts, and the signals consisting of both DC and AC components are in uppercase letters with lowercase subscripts and superscripts. Fig. 5.12 shows the models for the EQE measurements of the Ge subcells under the bias condition with the pulsed light bias i_{bs}^{m} on the InGaAs subcell (a), and under the probing monochromatic light scanning through the Ge wavelength range (b) and through the InGaAs wavelength range (c). As shown by the bias condition in Fig. 5.12 (a), the InGaP subcell D^{T} and InGaAs subcell D^{M} are light biased and generate the photocurrent I_{BS}^{T} and I_{BS}^{M}, respectively. Because the bias light on an upper subcell may not be completely absorbed, the unabsorbed bias light may generate additional photocurrent in the lower subcell. This optical leakage current is modeled as a current controlled current source $I_{LK}^{T,M} = \alpha_{LK}^{T,M} I_{BS}^{T}$ from the top to the middle subcell and $I_{LK}^{M,B} = \alpha_{LK}^{M,B} I_{BS}^{M}$ from the middle

to the bottom subcell. The leakage strengths $\alpha_{\mathrm{LK}}^{\mathrm{T,M}}$ and $\alpha_{\mathrm{LK}}^{\mathrm{M,B}}$ are wavelength dependent constants. Moreover, the radiative recombination in an upper subcell with a larger bandgap generates photons that can be reabsorbed in the lower subcell. This luminescence coupling effect is observed between the InGaAs subcell D^{M} and Ge subcell D^{B} for some of the solar cells used in this study, and is modeled as a current controlled current source $I_{\mathrm{LC}}^{\mathrm{M,B}} = f_{\mathrm{LC}}^{\mathrm{M,B}}\left[I\left(D^{\mathrm{M}}\right)\right]$. The InGaP and InGaAs subcells are forward biased under their respective light biases, and the effect of their shunt resistances can be neglected. The Ge subcell is either reverse biased or weakly forward biased under the DC bias voltage V_{DC} and the unintentional light bias from the leakage light and luminescence coupling. Because the Ge subcell usually has a soft breakdown under reverse bias, its shunt resistance $R_{\mathrm{SH}}^{\mathrm{B}}$ decreases with increasing reverse bias. In the small signal models of Fig. 5.12 (b) and (c), the subcells are replaced with their small signal diode resistances r^{t}, r^{m} and r^{b} and the small signal shunt resistance of the Ge subcell $r_{\mathrm{sh}}^{\mathrm{b}}$. The small signal luminescence coupling current is modeled as $i_{\mathrm{lc}}^{\mathrm{m,b}} = \alpha_{\mathrm{lc}}^{\mathrm{m,b}} i\left(r^{\mathrm{m}}\right)$ with the luminescence coupling strength $\alpha_{\mathrm{lc}}^{\mathrm{m,b}} = dI_{\mathrm{LC}}^{\mathrm{MB}} / dI\left(D^{\mathrm{M}}\right)$. The probing monochromatic light generates an AC photocurrent shown as the current source $i_{\mathrm{ph}}^{\mathrm{b}}$ on the Ge subcell in Fig. 5.12 (b) and the current source $i_{\mathrm{ph}}^{\mathrm{m}}$ on the InGaAs subcell in Fig. 5.12 (c). In order to eliminate the measurement artifacts, the pulsed light bias $i_{\mathrm{bs}}^{\mathrm{m}}$ is added to the light bias as highlighted in Fig. 5.12.

5.4.2 Necessary Pulse Light Bias

The necessary pulsed light bias can be rigorously derived from the small signal models in Fig. 5.12 (b) and (c).

In the Ge wavelength range, the output current i_o is

$$i_o = \frac{i_{bs}^m \left[r^m + \left(\alpha_{lk}^{m,b} + \alpha_{lc}^{m,b} \right) r^b r_{sh} / \left(r^b + r_{sh} \right) \right] + i_{ph}^b \, r^b r_{sh} / \left(r^b + r_{sh} \right)}{r^t + r^m + \left(1 + \alpha_{lc}^{m,b} \right) r^b r_{sh} / \left(r^b + r_{sh} \right) + R_L}. \tag{5.10}$$

When the measurement artifact is eliminated, i_o is equal to the photocurrent i_{ph}^b of the Ge subcell. Substituting this condition into Eq. (5.10), the necessary photocurrent $i_{bs}^m(\mathrm{Ge})$ to eliminate the measurement artifact is obtained as

$$i_{bs}^m(\mathrm{Ge}) = \frac{i_{ph}^b \left[r^t + r^m + \alpha_{lc}^{m,b} \, r^b r_{sh} / \left(r^b + r_{sh} \right) + R_L \right]}{r^m + \left(\alpha_{lc}^{m,b} + \alpha_{lk}^{m,b} \right) r^b r_{sh} / \left(r^b + r_{sh} \right)}, \tag{5.11}$$

which shows that $i_{bs}^m(\mathrm{Ge})$ is in phase with i_{ph}^b. In practice, $i_{bs}^m(\mathrm{Ge})$ can be obtained by varying i_{bs}^m and measuring i_o iteratively until Eq. (5.11) is satisfied. The i_o in this case, i.e. $i_o(\mathrm{Ge})$, yields the actual EQE of the Ge subcell.

In the InGaAs wavelength range, the output current i_o is

$$i_o = \frac{\left(i_{ph}^m + i_{bs}^m \right) \left[r^m + \left(\alpha_{lk}^{m,b} + \alpha_{lc}^{m,b} \right) r^b r_{sh} / \left(r^b + r_{sh} \right) \right]}{r^t + r^m + \left(1 + \alpha_{lc}^{m,b} \right) r^b r_{sh} / \left(r^b + r_{sh} \right) + R_L}. \tag{5.12}$$

When the measurement artifact is eliminated, i_o is equal to the optical leakage current $i_{lk}^{m,b}$ generated by the unabsorbed probing monochromatic light from the InGaAs subcell, i.e. $i_o(\mathrm{InGaAs}) = \alpha_{lk}^{m,b} i_{ph}^m$. Substituting this condition into Eq. (5.12), the necessary photocurrent $i_{bs}^m(\mathrm{InGaAs})$ to eliminate the measurement artifact is obtained as

$$i_{\mathrm{bs}}^{\mathrm{m}}(\mathrm{InGaAs}) = i_{\mathrm{ph}}^{\mathrm{m}} \frac{\alpha_{\mathrm{lk}}^{\mathrm{m,b}} r^{\mathrm{t}} + \left(\alpha_{\mathrm{lk}}^{\mathrm{m,b}} - 1\right) r^{\mathrm{m}} + \left(\alpha_{\mathrm{lk}}^{\mathrm{m,b}} - 1\right) \alpha_{\mathrm{lc}}^{\mathrm{m,b}} r^{\mathrm{b}} r_{\mathrm{sh}} / \left(r^{\mathrm{b}} + r_{\mathrm{sh}}\right) + \alpha_{\mathrm{lk}}^{\mathrm{m,b}} R_{\mathrm{L}}}{r^{\mathrm{m}} + \left(\alpha_{\mathrm{lc}}^{\mathrm{m,b}} + \alpha_{\mathrm{lk}}^{\mathrm{m,b}}\right) r^{\mathrm{b}} r_{\mathrm{sh}} / \left(r^{\mathrm{b}} + r_{\mathrm{sh}}\right)}, \qquad (5.13)$$

which shows that $i_{\mathrm{bs}}^{\mathrm{m}}(\mathrm{InGaAs})$ can be obtained directly if the photocurrent $i_{\mathrm{ph}}^{\mathrm{m}}$ of the InGaAs subcell can be accurately measured under the DC bias condition. In addition, $i_{\mathrm{bs}}^{\mathrm{m}}(\mathrm{InGaAs})$ is in anti-phase with $i_{\mathrm{ph}}^{\mathrm{m}}$ because the term associated with the bottom subcell usually dominates in the numerator of Eq. (5.13).

For Ge subcells with weak luminescence coupling from the InGaAs subcell due to low material quality or under weak bias light intensity, Eq. (5.11) and (5.13) are simplified to

$$i_{\mathrm{bs}}^{\mathrm{m}}(\mathrm{Ge}) = i_{\mathrm{ph}}^{\mathrm{b}} \frac{r^{\mathrm{t}} + r^{\mathrm{m}} + R_{\mathrm{L}}}{r^{\mathrm{m}} + \alpha_{\mathrm{lk}}^{\mathrm{m,b}} r^{\mathrm{b}} r_{\mathrm{sh}} / \left(r^{\mathrm{b}} + r_{\mathrm{sh}}\right)}, \qquad (5.14)$$

$$i_{\mathrm{bs}}^{\mathrm{m}}(\mathrm{InGaAs}) = i_{\mathrm{ph}}^{\mathrm{m}} \frac{\alpha_{\mathrm{lk}}^{\mathrm{m,b}} r^{\mathrm{t}} + \left(\alpha_{\mathrm{lk}}^{\mathrm{m,b}} - 1\right) r^{\mathrm{m}} + \alpha_{\mathrm{lk}}^{\mathrm{m,b}} R_{\mathrm{L}}}{r^{\mathrm{m}} + \alpha_{\mathrm{lk}}^{\mathrm{m,b}} r^{\mathrm{b}} r_{\mathrm{sh}} / \left(r^{\mathrm{b}} + r_{\mathrm{sh}}\right)}, \qquad (5.15)$$

where the luminescence coupling strength is neglected. For high quality Ge subcells with large small signal resistance and strong luminescence coupling from the InGaAs subcells at the operating points, Eq. (5.11) and (5.13) are simplified to

$$i_{\mathrm{bs}}^{\mathrm{m}}(\mathrm{Ge}) = i_{\mathrm{ph}}^{\mathrm{b}} \frac{\alpha_{\mathrm{lc}}^{\mathrm{m,b}}}{\alpha_{\mathrm{lc}}^{\mathrm{m,b}} + \alpha_{\mathrm{lk}}^{\mathrm{m,b}}}, \qquad (5.16)$$

$$i_{\mathrm{bs}}^{\mathrm{m}}(\mathrm{InGaAs}) = i_{\mathrm{ph}}^{\mathrm{m}} \frac{\left(\alpha_{\mathrm{lk}}^{\mathrm{m,b}} - 1\right) \alpha_{\mathrm{lc}}^{\mathrm{m,b}}}{\alpha_{\mathrm{lc}}^{\mathrm{m,b}} + \alpha_{\mathrm{lk}}^{\mathrm{m,b}}}. \qquad (5.17)$$

where the small signal resistances of the three subcells are neglected or canceled out.

It is important to note that the small signal resistances, the luminescence coupling strength and optical leakage strength in the above equations can be measured under the DC bias condition using the characterization methods developed in [4], [6] and [7].

5.4.3 Simulation

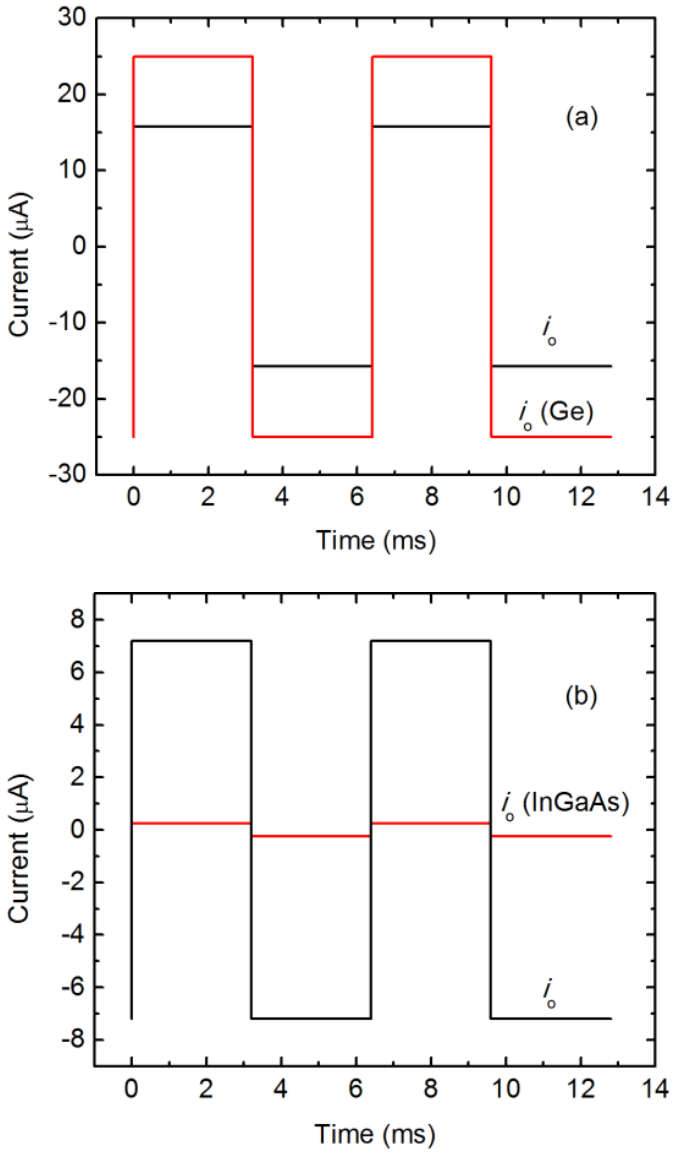

Fig. 5.13. Simulated waveforms of the apparent spectral response i_o under the DC bias condition and the actual spectral response $i_o(\text{Ge})$ in the Ge wavelength range (a) and $i_o(\text{InGaAs})$ in the InGaAs wavelength range (b) with the pulsed light bias in the EQE measurements of the Ge subcell.

The concepts proposed above are proven using SPICE simulations with the assumed subcell parameters, bias condition and the probing monochromatic light shown in Table 5.1. Fig. 5.13 (a) and (b) show the simulation results of the apparent spectral response i_o in the Ge wavelength range and in the InGaAs wavelength range, respectively. Because of the shunt and luminescence coupling effects, i_o under the DC bias condition is 62.8% of the photocurrent i_{ph}^{b} generated by the probing monochromatic light in the Ge wavelength range, and it is about 28.8% of the photocurrent i_{ph}^{m} generated by the probing monochromatic light in the InGaAs wavelength range. According to Eq. (5.11) and (5.13), the necessary photocurrent $i_{bs}^{m}(\text{Ge})$ to eliminate the EQE measurement artifacts in the Ge wavelength range is 64.4 μA peak-to-peak and is in phase with i_{ph}^{b}, and the necessary photocurrent $i_{bs}^{m}(\text{InGaAs})$ in the InGaAs wavelength range is 48.3 μA peak-to-peak and is in anti-phase with i_{ph}^{m}. Therefore, with the pulsed light bias, the actual spectra response $i_o(\text{Ge})$ in the Ge wavelength range is equal to i_{ph}^{b}, and $i_o(\text{InGaAs})$ in the InGaAs wavelength range is equal to 1% of i_{ph}^{m} due to the

optical leakage. These modeling results have confirmed that the EQE measurement artifacts are eliminated.

5.4.4 Measurement

The PLB method is applied to the characterization of commercial triple-junction solar cells. The pulsed light bias generated by a 780 nm laser diode operates at 156.2 Hz and is synchronized to the probing monochromatic light. This frequency is low enough for the subcell photocurrent responses to follow, because the pulse width is much larger than the minority carrier lifetime [6], [7]. A neutral density filter is used to reduce the light intensity from the laser diode and make the photocurrent i_{bs}^{m} comparable to the photocurrent generated by the probing monochromatic light. i_{bs}^{m} is measured when an additional light bias is applied to the Ge subcell to make the InGaAs subcell current limiting.

5.4.4.1 Shunt Effect

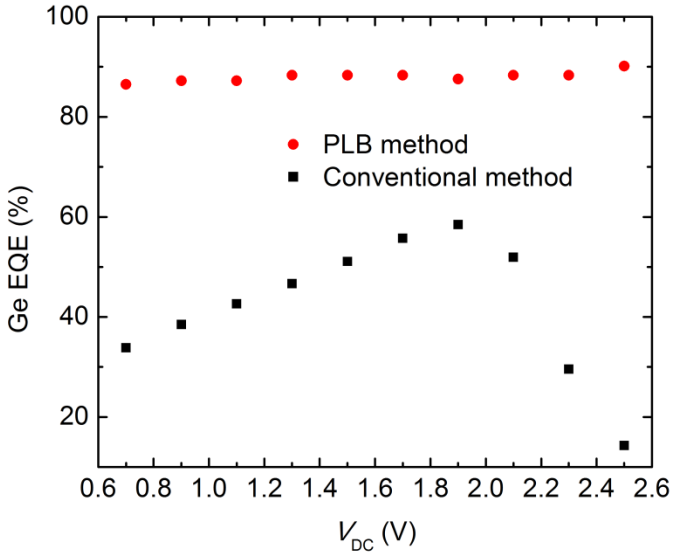

Fig. 5.14. EQE measured using the conventional method (dark dots) and the PLB method (red dots) for the Ge subcell of triple junction solar cell S1.

Fig. 5.14 shows the EQE measurement results of the Ge subcell in the triple-junction solar cell S1 with strong shunt effect and negligible luminescence coupling effect. Using the conventional method, the measured apparent EQE reaches a peak of 59% at 980 nm in the Ge wavelength range at the optimal V_{DC} of 1.9 V, and drops at larger and smaller V_{DC} because of the decreased small signal diode resistance and shunt resistance of the Ge subcell, respectively. Using the PLB method, the actual EQE is measured as 88% in the Ge wavelength range according to Eq. (5.14), and it is close to zero at 780 nm in the InGaAs wavelength range according to Eq. (5.15) as the optical leakage effect is not observed in this device.

5.4.4.2 Luminescence Coupling Effect

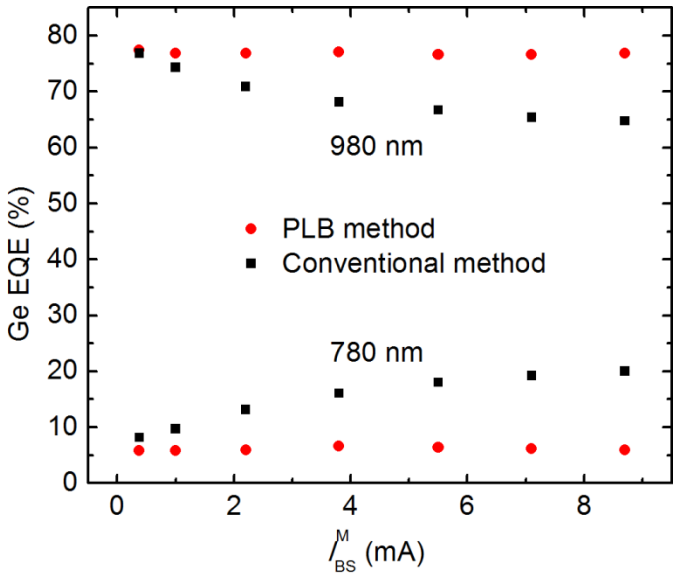

Fig. 5.15. EQE measured using the conventional method (dark dots) and the PLB method (red dots) for the Ge subcell of triple junction solar cell S2 at the optimal bias voltage 0 V.

Fig. 5.15 shows the EQE measurement results of the Ge subcell in the triple-junction solar cell S2 with characteristics of comparable shunt and luminescence coupling, which is measured at the optimal V_{DC} where the shunt effect of these solar cells is minimized and only the luminescence coupling effect affects the spectral responses. Using the conventional method, the measured apparent EQE decreases at 980 nm in the Ge wavelength range and increases at 780 nm in the InGaAs wavelength range with the increase of I_{BS}^{M}, because of the increased luminescence coupling effect when the InGaAs subcell becomes more forward biased. Using the PLB method, the actual EQE is measured as about 77% in the Ge wavelength range according to Eq. (5.16), and is about 6.1% in the InGaAs wavelength range according to Eq. (5.17). The $i_{o}\left(\mathrm{InGaAs}\right)$ measured using the PLB method in the InGaAs wavelength range is 6.7% of i_{ph}^{m}, which is in good agreement with the optical leakage strength of 6.5% determined under the DC bias condition. This finding confirms that the measurement artifact is eliminated.

5.4.4.3 Combined Effects of Shunt and Luminescence Coupling

Fig. 5.16 shows the EQE of the same device used for Fig. 5.15 measured at a V_{DC} different from the optimal bias voltage, where the shunt and

luminescence coupling effects are comparable. Using the conventional method, the measured apparent EQE reaches the maximum of 64% at 980 nm in the Ge wavelength range and the minimum of 14% at 780 nm in the InGaAs wavelength range, where the photocurrent I_{BS}^{M} is equal to 1.8 mA at the optimal DC bias light intensity on the InGaAs subcell. The measured apparent EQE decreases in the Ge wavelength range and increases in the InGaAs wavelength range at smaller I_{BS}^{M} because of the increased shunt effect, and at larger I_{BS}^{M} because of the increased luminescence coupling effect. Using the PLB method, the EQE is measured as 78% in the Ge wavelength range and 8.0% in the InGaAs wavelength range.

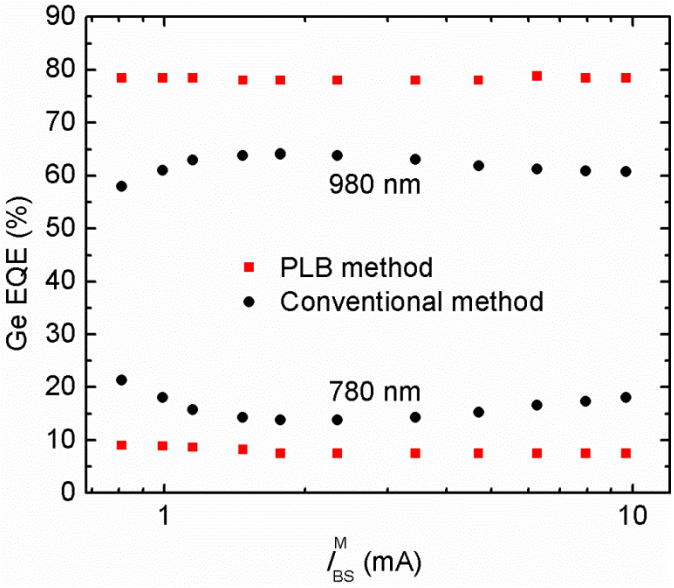

Fig. 5.16. EQE measured using the conventional method (dark dots) and the PLB method (red dots) for the Ge subcell of triple junction solar cell S2 at the bias voltage -0.5 V.

The necessary photocurrent $i_{\mathrm{bs}}^{\mathrm{m0}}$ generated by the bias light on the InGaAs subcell is determined with the small signal resistances r^{t}, r^{m} and $r^{\mathrm{b}}r_{\mathrm{sh}}/\left(r^{\mathrm{b}}+r_{\mathrm{sh}}\right)$ in section 4.6.3, the luminescence coupling strength $\alpha_{\mathrm{lc}}^{\mathrm{m,b}}$ the same in section 4.6.2, and the optical leakage strength 8.5%. The slight differences of these parameters determined for the solar cell S2 from the other sections are caused by the change of optical alignment. i_{o} measured with the PLB method is about 9% of $i_{\mathrm{ph}}^{\mathrm{m}}$ in the InGaAs wavelength range, which is in good agreement with the leakage strength 8.5%. This shows that the measurement artifact is eliminated, because the measured output current is equal to the leakage current in the InGaAs wavelength range.

The actual EQE of the MJ cells does not depend on the DC bias voltage or the bias light intensity, because the current collection in the subcells in principle is not a function of the depletion region width. The variation of EQE with the DC bias condition measured using the conventional method is caused by the coupling effects between the subcells, while the EQE determined using the PLB method independent of the DC bias condition is a strong evidence of the removal of the measurement artifacts.

This paper only uses one pulsed light bias on the InGaAs subcell for simplicity. In principle, pulsed light biases can be used on any of the subcells to control the subcell operating points. If there is neither optical leakage nor the load resistor R_{L}, pulsed light biases can be applied to both the InGaP and InGaAs subcells, and the necessary photocurrent to eliminate the measurement artifacts

becomes $i_{bs}^{m}(\text{Ge}) = i_{ph}^{b}$ in the Ge wavelength range and $i_{bs}^{m}(\text{InGaAs}) = -i_{ph}^{m}$ in the InGaAs wavelength range. In this case, the subcell parameters are not needed to determine the necessary pulsed light bias.

In addition, it is worth mentioning that lasers are used for the light biases because the subcell responses need to be precisely controlled and measured. If the bias light on a subcell is also absorbed by the adjacent subcells, the characterization methods developed for subcell parameters in Eq. (5.10)-(5.17) may not be applicable anymore, and it becomes more complicated to determine the necessary pulsed light bias. For MJ solar cells with more subcells and more spectral interferences, proper characterization methods need to be developed to address these issues.

References

[1] G. Siefer, C. Baur, and A. W. Bett, "External quantum efficiency measurements of germanium bottom subcells: measurement artifacts and correction procedures," in *Proc. 35th IEEE PVSC*, Hawaii, pp. 704–707, Jun. 2010.

[2] J. J. Li, S. H. Lim, C. R. Allen, D. Ding, and Y. H. Zhang, "Combined effects of shunt and luminescence coupling on external quantum efficiency of multijunction solar cells," *IEEE J. Photovoltaics*, vol. 1, no. 2, pp. 225–230, Oct. 2011.

[3] J. J. Li, C. R. Allen, S. H. Lim, and Y. H. Zhang, "A novel method to eliminate the measurement artifacts of external quantum efficiency of multi-junction solar cells caused by the shunt effect," in *Proc. SPIE*, 8256, 825616, 2012.

[4] J. J. Li, C. R. Allen, S. H. Lim, and Y. H. Zhang, "Elimination of measurement artifacts in external quantum efficiency of multijunction solar cells using a pulse voltage bias," *Prog. Photovolt: Res. Appl.*, in review

[5] J. J. Li and Y. H. Zhang, "Elimination of measurement artifacts in external quantum efficiency of multijunction solar cells using a pulse light bias," *IEEE J. Photovoltaics*, in review.

[6] R. R. King, D. C. Law, K. M. Edmondson, C. M. Fetzer, G. S. Kinsey, H. Yoon, R. A. Sherif, and N. H. Karam, "40% efficient metamorphic GaInP/GaInAs/Ge multijunction solar cells," *Appl. Phys. Lett.*, vol. 90, no. 18, pp. 183516, 2007.

[7] R. R. King, C. M. Fetzer, P. C. Colter, K. M. Edmondson, J. H. Ermer, H. L. Cotal, H. Yoon, A. P. Stavrides, G. Kinsey, D. D. Krut, and N. H. Karam, "High-efficiency space and terrestrial multijunction solar cells through bandgap control in cell structures," in *Proc. 29th IEEE PVSC*, pp. 776–781,2002.

VI CONCLUSIONS

This dissertation addresses three issues hindering the improvement of the efficiencies of multi-junction (MJ) solar cells, including the development of lattice-matched materials for high efficiency MJ solar cells, the contact grid design of concentrator solar cells and the accurate measurement of external quantum efficiency (EQE) of MJ solar cells.

Firstly, a series of CdSe/CdTe superlattices are grown on GaSb substrates by molecular beam epitaxy for a subcell of the MJ solar cells, and their material properties are studied. The high structural qualities of the superlattices are shown in high-resolution X-ray diffraction patterns, high-resolution transmission electron microscopy images and the selected area electron diffraction pattern. The ground state optical transition energies of the superlattices measured using photoluminescence (PL) are smaller than the bandgap of either CdSe or CdTe, and hence establish the existence of a strong type-II band alignment between CdSe and CdTe. The type-II valence band offset between unstrained CdSe and CdTe is determined as 0.63 ± 0.06 eV by fitting the PL peak positions to the ground state optical transition energies calculated using the Kronig-Penney model. Furthermore, the PL peak position blue shifts with an increase of excess carrier concentrations. This blue shift is attributed primarily to the band bending effect of the type-II superlattices by comparing the measured blue shift with the increase in the ground state transition energy obtained from self-consistent solutions of the Schrödinger and Poisson equations.

Secondly, the front contact grid layout of concentrator solar cells is studied using the distributed series resistance model. By considering the distributed nature of the emitter layer sheet resistance, the contact resistance, and the metal finger resistance, this model shows that the local voltage and current densities vary along the path of lateral current flow. This effect is especially important under high concentrations and at large finger spacing, as the high local voltage may cause the photocurrent generated at the junction to recombine locally. In this situation, the junction current recombination loss also plays a significant role in the design of the contact grid layout, in addition to the shadowing loss and series resistance loss considered in the conventional lumped resistance model. At the optimal finger spacing, the lumped series resistance model is a good approximation in spite of its assumption of uniform voltage and current density along the path of lateral current flow.

Lastly, EQE measurement artifacts caused by the shunt and luminescence coupling effects are studied. Models are built for the measurements of triple junction solar cells, and the subcell parameters in the models are characterized. Good agreements are found between modeling and EQE measurement results for only the shunt effect, only the luminescence coupling effect and the combined effects of shunt and luminescence coupling. The results show that the EQE measurement artifacts can be minimized using proper DC voltage and light biases.

In order to eliminate the EQE measurement artifacts, a pulse voltage bias method and a pulse light bias method are developed. The pulse voltage bias or the

pulse light bias, which is synchronized to the chopped monochromatic light and superimposed on the DC voltage and light biases, is used to control the subcell operating points and counterbalance the effects of shunt and luminescence coupling. The necessary pulse voltage bias and the necessary photocurrent generated by the pulse light bias are derived and the measurement procedures are developed. The methods are demonstrated to effectively eliminate the measurement artifacts caused by only the shunt effect, only the luminescence coupling effect and the combined effects of shunt and luminescence coupling.